Early Thermalization and Hydrodynamic Expansion in Nuclear Collisions at RHIC

(Dissertation)

Peter Franz Kolb

Universität Regensburg
Januar 2002

Meinen lieben Eltern gewidmet.

Early thermalization and hydrodynamic expansion in nuclear collisions at RHIC

Dissertation

zur Erlangung des
Doktorgrades der Naturwissenschaften
(Dr. rer. nat.)
der Naturwissenschaftlichen Fakultät II - Physik
der Universität Regensburg

vorgelegt von

Peter Franz Kolb
aus Waldsassen

Januar 2002

Die Arbeit wurde angeleitet von: Prof. Dr. Ulrich Heinz.

Das Promotionsgesuch wurde eingereicht am: 31. Januar 2002.

Die wissenschaftliche Aussprache fand am 26. März 2002 statt.

Prüfungsausschuss:

Prof. Dr. Christian Back	(Vorsitzender)
Prof. Dr. Ulrich Heinz	(1. Gutachter)
Prof. Dr. Joachim Keller	(2. Gutachter)
Prof. Dr. Vladimir Braun	(weiterer Prüfer)

ZUSAMMENFASSUNG

Kollisionen schwerer Atomkerne mit ultrarelativistischen Energien eröffnen die Möglichkeit ihre elementaren Bausteine, die Quarks und Gluonen, in ausgedehnten Systemen unter extremen Bedingungen (Temperaturen von einigen hundert MeV $\sim 10^{12}$ K) zu studieren. Dies ist von besonderem Interesse, als Quanten Chromodynamik, die fundamentale Theorie zur Beschreibung der Starken Wechselwirkung, einen Phasenübergang von Kernmaterie bei Temperaturen in dieser Größenordnung vorhersagt. Demnach sind bei Temperaturen höher als die kritsche Übergangstemperatur die Quarks und Gluonen aus ihren einschließenden Nukleonenhüllen befreit und die mikroskopischen Freiheitsgrade des Systems durch das statistische Verhalten dieser elementaren Bausteine bestimmt, nicht mehr durch die Statistik der uns umgebenden hadronischen Materie. Ein wichtiges Ziel der Schwerionenexperimente ist es, ein ausreichend großes System aus freien Quarks und Gluonen zu erzeugen und den Übergang zu hadronischer Materie eindeutig zu identifizieren und im Detail zu untersuchen.

Voraussetzung für die Definition thermodynamischer Variablen und die Diskussion thermodynamischer Konzepte ist eine hinreichende Ausdehnung des Systems und (lokale) Thermalisierung seiner Konstituenten. In dieser Arbeit nehmen wir an, dass diese Voraussetzungen erfüllt sind und bestimmen die zeitliche Entwicklung des Systems anhand der hydrodynamischen Bewegungsgleichungen. Eine große Anzahl von Observablen wird mit experimentellen Daten von Gold-Gold Kollisionen mit Schwerpunktsenergien von $\sqrt{s} = 130$ GeV pro Nukleon verglichen. Die Übereinstimmung von Theorie und Experiment, welche unter der Annahme von verzögerter Thermalisierung oder schwächerem Rückstreuen der Konstituenten verloren geht, ist ein klarer Hinweis, dass bei diesen Experimenten in der Tat ein System in lokalem thermodynamischen Gleichgewicht erzeugt wird. Weitere Observablen deuten darauf hin, dass das System während seiner kontinuierlichen Expansion und Kühlung einen Phasenübergang erster Ordnung durchläuft.

Im ersten Kapitel dieser Dissertation wird die Zielsetzung dieser Arbeit in

weiteren Details motiviert. Ferner werden dort die Vorzüge und Nachteile einer makroskopischen Studie eines solch komplexen Systems diskutiert.

Das zweite Kapitel beschäftigt sich mit der Zeitentwicklung des Feuerballs welcher in der Kollision produziert wird, mit besonderem Hinblick auf Phänomene die aus der Asymmetrie in nicht-zentralen Stößen hervorgerufen werden. Dazu beschreiben wir zunächst die Geometrie der Kollision und diskutieren Energie- und Entropiedeposition im Reaktionsvolumen. Anschließend werden die hydrodynamischen Bewegungsgleichungen und die Zustandsgleichung unserer Rechnungen beschrieben. Nachdem wir uns mit dem Ausfrieren der meßbaren Teilchen aus dem Feuerball befaßt haben, können wir mit Hilfe von Teilchenspektren identifizierter Teilchen von zentralen Kollisionen die Parameter unserer Rechnungen bestimmen. Die Initialisierung des Systems bei endlichem Stoßparameter folgt dann aus der Geometrie der stoßenden Kerne und liefert uns neue Observable ohne Einführung weiterer Parameter. Als Parameter zur Beschreibung zentraler Stöße bei 130 GeV finden wir bei einer Äquilibrierungszeit von $\tau_{\rm equ} = 0.6$ fm/c das Maximum der Energiedichte zu $e_{\rm equ} = 24.6$ GeV/fm^3 mit einer maximalen Baryonenzahldichte von $n_{\rm equ} = 0.3$ fm^{-3} (resultierend in einer Temperatur von $T_{\rm equ} = 340$ MeV im Zentrum der Kollision, weit über der kritischen Temperatur unserer Zustandsgleichung). Teilchen werden aus dem Feuerball ausgefroren, wenn die lokale Temperatur auf $T_{\rm dec} = 130$ MeV abfällt. Am Schluss des Kapitels diskutieren wir die Zeitentwicklung des Systems und beobachten wie Anisotropien im Ortsraum in einem kurzen Zeitraum zu Anisotropien im Impulsraum führen, und dabei die Ortsraumanisotropie gänzlich reduzieren. Anisotropien im Impulsraum sind daher Observablen die früh, in den heißesten Stadien der Kollision aufgebaut werden.

Quantitative Vorhersagen der Hydrodynamik werden in den nächsten Kapiteln mit experimentellen Daten verglichen. Zunächst, in Kapitel 3, nützen wir den Einfluss der variierenden Systemgröße und Energiegehalt welcher sich bei nichtverschwindendem Stoßparameter ergibt. Stöße verschiedener Zentralität liefern daher unterschiedliche transversale Impulsspektren, gegeben durch verschiedene Multiplizitäten, mittlere Teilchenimpulse und Flussgeschwindigkeiten. Die hydrodynamischen Resultate sind in ausgezeichnetem Einklang mit den experimentellen Daten. Nur in Kollisionen mit großem Stoßparameter ($b > 9$ fm) und für hohe Teilchenimpulse gehen die hydrodynamischen Voraussetzungen (u.a. Systemgröße $\gg$ mittlere freie Weglänge) verloren und die Daten werden nicht mehr korrekt reproduziert.

Im vierten Kapitel untersuchen wir Observable, welche tatsächlich von der Impulsraumanisotropie des Endzustands stammen. Wegen größerer Druckgradienten in Richtung des Stoßparameters ist der kollektive Fluss in dieser Richtung größer, und somit zeigt auch die Verteilung der emittierten Teilchen eine azimuthale Modulation, welche durch eine Fourier-Dekomposition quantitativ untersucht werden kann. Durch die effiziente Transformation der anisotropen Druckgradienten in Impulsanisotropien unter einer hydrodynamischen Entwicklung sind die hydrodynamischen Vorhersagen für 'elliptischen Fluss' (den zweiten Koeffizienten der Fourierentwicklung) relativ hoch. Die Daten erreichen diese hohen Werte solange der Stoßparameter und die transversalen Impulse der untersuchten Teilchen nicht zu groß ist. Wir diskutieren die Wichtigkeit von rascher Thermalisierung, sowie den Einfluss des Phasenübergangs, welcher sich vor allem bei schweren Teilchen zeigt und auf die Existenz eines Übergangs mit relativ großer latenter Wärme hinweist.

Die Wechselwirkung zwischen Ortsraum und Impulsraum ist damit auf makroskopischer Ebene verstanden – die Entwicklung des Systems folgt den hydrodynamischen Gesetzen. Im fünften Kapitel behandeln wir jedoch die unerwarteten experimentellen Resultate zur Geometrie des Ausfriervorgangs, welche sich bisher aller theoretischen Beschreibung entziehen. Wir untersuchen die Ursachen und Gründe der Diskrepanz und spekulieren über Mechanismen, welche die Geometrie des Ausfrierens beeinflussen, ohne die hydrodynamisch korrekten Impulsobservablen nachteilig zu verändern. Zum Abschluss untersuchen wir diese Ortsraumobservablen für nicht-zentrale Stöße. Hier finden wir teilweise wieder quantitativen Einklang mit den gemessenen Daten.

Die meisten analytischen Rechnungen und Herleitungen sowie technische Details sind in einem Anhang zusammengefasst.

CONTENTS

1 Introduction **1**

1.1 QCD and the Quark-Gluon Plasma 2

1.2 Macro- versus microscopic modeling 4

1.3 Predictions, confirmations and the structure of this thesis 6

1.4 Remarks on the notation 8

2 Evolution of the fireball **10**

2.1 Geometry of the collision 11

2.2 Hydrodynamic expansion 20

2.3 Freeze-out 26

2.4 Quantitative initialization 30

2.5 Time evolution of flow characteristics 33

2.6 The influence of the phase transition 36

3 Global transverse observables **40**

3.1 Transverse momentum spectra 41

3.2 Particle multiplicity 44

3.3 Mean transverse momentum 45

3.4 Mean transverse flow velocity 46

3.5 Transverse Energy 47

4 Anisotropic particle emission 50

4.1 Elliptic flow from hydrodynamics 52

4.2 Indications for *early* thermalization 64

4.3 Elliptic flow and the phase transition 66

4.4 A blast wave model for anisotropic particle emission 67

5 HBT radii from hydrodynamics 70

5.1 The source function 71

5.2 Correlation lengths 75

5.3 HBT radii from central collisions 76

5.4 Failure of HBT predictions 80

5.5 Azimuthally sensitive HBT 86

6 Summary and conclusions 97

Appendix 101

A Coordinates and transformations 101

A.1 Coordinate space 101

A.2 Momentum space 105

B Integrals for correlation lengths 108

C Free streaming 112

C.1 Formalism 112

C.2 Illustration with a box profile 115

D Glossary 118

Bibliography 120

Acknowledgements 133

1

INTRODUCTION

In an effort to understand its place in the universe, civilization has developed philosophical models to describe matter on its smallest and its largest scales as well as the origin of the universe itself. With the technical revolution over the past centuries, the philosophical and theoretical constructs could be verified and checked on their consistency and predictive power as quantitative sciences developed. Precision experiments became the ultimate tools to decide on the validity and usefulness of descriptive models. Today we have 'standard models' for the interaction of fundamental particles and cosmology, which developed from highly successful interactions between theoretical and experimental physicists.

The standard model for the interaction between quarks and gluons which build up nuclear matter, Quantum Chromodynamics, predicts that nuclear matter undergoes a phase transition when heated to temperatures higher than a certain critical temperature $T_{\text{crit}} \sim 2 \cdot 10^{12}$ K. In every day life, quarks and gluons are tightly bound in the confined space of the cores of the atoms that surround us. At higher temperatures, so theory tells us, a plasma stage of quarks and gluons can form, in which they can travel freely over large distances without major interactions. Cosmology suggests that shortly after the Big Bang the temperature of the universe was high enough for this state to exist, before upon further expansion the universe cooled and quarks and gluons became confined into nuclear matter. By colliding large nuclei with relativistic velocities one hopes to heat nuclear matter above the transition temperature, and thus get a glimpse at this extraordinary state of matter and the state of the universe further back in time than any telescope will ever allow us to see.

Starting with the now legendary conference on "Statistical mechanics of quarks and hadrons" in Bielefeld 1980 [141] the field has since seen intense combined theoretical and experimental efforts to unequivocally identify this elusive state of nuclear matter. The search culminated in the summary of evidences from the heavy ion program at the SPS[1] at CERN almost 20 years later [60, 140]. Later in the year 2000 a new chapter was opened by the first collisions at the Relativistic Heavy Ion Collider (RHIC) at Brookhaven National Laboratory. With center of mass energies an order of magnitude higher than at the previous fixed target experiments at the SPS, chances are greater that the liberated quarks and gluons reach a state of local thermal equilibrium due to intense rescattering. Furthermore higher initial energy densities and temperatures of the system should lead to a larger lifetime of the deconfined state and lead to clearer signals of its existence. In fact, the first published results from the year 2000 run at RHIC are in quantitative agreement with rapid thermalization of the deconfined matter and a subsequent hydrodynamic expansion of nuclear matter undergoing a phase transition. Furthermore the experimental observables can so far *only* be explained under the assumption of early pressure in the system. The arguments and analysis leading to these conclusions are the main subject of this thesis.

1.1 QCD AND THE QUARK-GLUON PLASMA

On the most fundamental scale, nuclear matter is built up by quarks of spin 1/2 which interact by exchanging gluons – the spin 1 gauge Bosons of the theory, just as the electromagnetic forces between charged particles are mediated by photons, as described by Quantum Electrodynamics (QED). In contrast to electrodynamics where there is only one charge (which can be positive or negative) the quarks come in three different, so called ‘color’ charges (therefore ‘Quantum Chromodynamics’, or QCD). The interaction however is insensitive to rotations in SU(3) color space. This rotation is non-commutative, or non-Abelian, and this leads to a self-interaction of the mediators of the force – the gluons are colored objects themselves. This is why nuclear forces are so strong compared to the other fundamental interactions and what makes the theory intrinsically more complicated than QED, where photons do not carry charge and do not directly couple to themselves.

In principle everything about the strong interaction is known as it can be derived from the fundamental Lagrangian of QCD which was discovered almost 50 years ago [134]. However the mathematical techniques are not yet far enough developed to extract all of the desired information. One of the most intriguing features of QCD is that the coupling constant of the interaction decreases with

---

[1] The abbreviations used for experiments, colliders and laboratories are summarized in the Glossary.

increasing momentum transfer, a phenomenon termed 'asymptotic freedom' [53, 94]. Therefore even approximative schemes like the very successful perturbation theory and diagrammatical techniques which are of tremendous use in QED can only be applied in the extreme case of very large momentum transfer. Low energy phenomena however render perturbation theory invalid, as the coupling constant and therefore the expansion coefficient is not a small number anymore. This denies access to such interesting phenomena as color confinement, the clustering of color charged particles to form color neutral objects, and other non-perturbative phenomena.

Therefore, in order to study the features of strongly interacting matter, one has to rely on effective theories, or one extracts information from the QCD Lagrangian by numerical calculation of the desired observables on a four-dimensional space-time lattice. Again, due to the strong coupling at short distances, these calculations are tremendously time consuming, in particular as one has to reach the continuum limit, i.e. taking the grid-size of the calculations to distances small enough that the physical results are not influenced by the artificial discretization of the space time fabric by use of a numerical mesh.

Lattice calculations that study the thermodynamics of strongly interacting matter have indicated an abrupt jump in the scaling of the energy density with the fourth power of temperature [46, 95], and the most recent calculations (for a summary see e.g. [72]) locate the transition temperature of this discontinuity at around 155 - 175 MeV, depending on the assumptions and approximation schemes that are used in these calculations. The simplest explanation for the change of the scaling factor is in terms of a liberation of degrees of freedom at the transition temperature. The hadronic degrees of freedom which rule the thermodynamic properties of nuclear matter below T_{crit} give way to a larger number of degrees of freedom when the quarks and gluons break loose from their confining 'bags'. As the colored quarks and gluons are now freely roaming and as they are the constituents that determine the thermodynamic properties of this system, this state is called a 'Quark-Gluon Plasma' (QGP). By colliding large nuclei with ultra-relativistic energies one hopes to produce matter in the laboratory with temperatures and energy densities exceeding the critical values predicted by lattice QCD. This would allow the confirmation of the predictions of QCD and create a medium where perturbative methods find application to further study this elusive state of matter and its underlying theory.

Apart from a deconfining transition occurring at large temperatures, one also expects that the hadronic bags can be broken open at large particle densities or upon compression of nuclear matter. In fact, on the high density side of the phase diagram, a whole new set of effects of pairing phenomena sets in, and further phase transitions of QCD are expected. These conditions might be reached in the center of neutron stars, but to date there are no ways for an experimental investigation of these phenomena in sight. For an extensive review on high density QCD we refer to [100] and references therein.

1.2 MACRO- VERSUS MICROSCOPIC MODELING

One of the main objectives of the ultra-relativistic heavy ion program is to produce and study a thermodynamically equilibrated system of deconfined quarks and gluons at high temperature. Naturally, a system in thermodynamic equilibrium is characterized by macroscopic observables such as its temperature, its pressure, energy density, chemical potentials, etc. with no need for the detailed knowledge of the microscopic dynamics of the system's constituents.

If the system is in local thermal equilibrium, variations in the pressure fields (pressure gradients) will lead to a dynamical evolution of the macroscopic fields. The latter is described by the equations of hydrodynamics, which simply enforce locally the conservation of energy and momentum (plus other conserved currents in the system under investigation, like charge, baryon-number, strangeness, etc). After some initial configuration is given, the hydrodynamical laws fully determine the evolution of the system. Due to the simplicity of this macroscopic approach it has a long tradition in its application to hadronic and heavy ion collisions [81] and it has been developed to a high degree of sophistication, even attempting to incorporate entropy generation in the preequilibrium stage thus modeling the reaction dynamics even before equilibration (see the review [122] and references therein). However only in the new energy domain recently opened by the first run at RHIC we seem to have reached high enough particle densities that the rescattering of the secondary particles created sufficient thermodynamic equilibrium to allow for the macroscopic treatment, even in non-central collisions as we will see.

The ideal hydrodynamic description cannot describe the path from the initial partonic collisions to local thermal equilibration by frequent rescattering of the primary and secondary particles. Parton cascades have to be employed to understand the preequilibrium stage of the collision, but due to conceptual problems as well as numerical expenses advances in this direction are slow [22]. In our analysis we ignore the preequilibrium stage but find that the system is seemingly driven into local thermodynamic equilibrium at equilibration times $\tau_{\mathrm{equ}} \sim 0.6$ fm/c, from which on the hydrodynamic approach is applicable. The systems generated in the collisions are of finite spatial extent. By using as large nuclei as nature and the experimental setup allows, one tries to make the system as large as possible, to allow for larger and longer-lived fireballs. For hydrodynamic concepts to be valid in a finite system, the microscopic scattering lengths must be much smaller than the size of the system. Even though the QCD coupling decreases with temperature as discussed above, the mean free path at temperatures accessible at RHIC and the Large Hadron Collider LHC are much smaller than the radii of large nuclei [111]. Still, at some radial distance from the center of the colliding nuclei the energy and particle density are too low as to provide for sufficiently short rescattering lengths, and the effective hydrodynamic treatment gradually loses its foundations of validity. In principle this can be circumvented by switching to a microscopical description for the late and dilute hadronic stages of the collision, as pioneered by Bass et al. for azimuthally symmetric collisions [20, 21] and recently generalized to non-central collisions by Derek Teaney and collaborators [124, 125, 126]. We will instead use the simpler Cooper-Frye prescription [39] to end the hydrodynamic evolution as discussed in much detail in Section 2.3.

Even though microscopical scattering processes are not accessible within the macroscopic treatment of the system, a lot of microscopic information about the constituents of the system can be extracted from thermodynamics. After all, one of the major pillars of atomic theory resulted from thermodynamic studies of gaseous systems at the beginning of the 20th century. Other thermodynamic investigations, for example on the specific heat of gases, led to more information about their microscopic constituents such as the discovery of rotational or vibrational degrees of freedom of the atoms. And ultimately, a macroscopic description is the most natural way to test for equilibration and the applicability of thermodynamic concepts.

However, the scattering dynamics and the path to equilibration are completely ignored in the macroscopic approach, even though those questions are certainly of fundamental interest. Parton cascades set out to study the full collision dynamics [49, 138]. So far however little is known about the in-medium behavior of partons under such extreme conditions. To reproduce the large flow signals [91] as observed at RHIC energies, cascade calculations either have to assume much larger cross sections for the fundamental interactions or parton multiplicities orders of magnitudes larger than traditional partonic calculations like HIJING [128]. The strong transverse dynamics, which (under realistic conditions) so far is only reproduced by calculations with an initial hydrodynamic stage, strongly points to some microscopical effects that we are not yet aware of. Recently, progress was reported through the phenomenological introduction of string-melting processes [86], or multi-pomeron exchanges in string cascades [135]. Another complication in partonic approaches lies in the formation of the finally observable colorless hadrons. The non-perturbative transition from colored partons to final state observables has to be introduced ad hoc and can so far not be described in the partonic cascades.

Macroscopic approaches circumvent the introduction of additional parameters and speculative 'new' physics in the dynamical stage. However they rely on crucial assumptions on the equilibration stage and freeze-out process, which we will discuss thoroughly in Chapter 2.

1.3 PREDICTIONS, CONFIRMATIONS AND THE STRUCTURE OF THIS THESIS

Whenever experiments enter a new domain in energy, predictions for the upcoming observations deviate widely. This was particularly true in heavy ion physics, where the first run of RHIC in the year 2000 reached center of mass energies an order of magnitude larger than the previous fixed target experiments at the SPS or AGS. This tremendous energy gain promised to lead to new phenomena, never before to be studied on earth. Correspondingly the predictions of various theories and scenarios had a large spread, and a special session [19] on RHIC predictions was called in at the last International Conference on Ultra-Relativistic Nucleus-Nucleus Collisions in 1999 [142] before RHIC was to start producing collisions in this new domain and data would become available to be tested against theory and model calculations. In spite of the large spread of detailed predictions, there was broad agreement that the larger collision energies would lead to higher energy densities in the initial stages and higher particle multiplicities in the final stages of the collision.

For our analysis, the final particle multiplicity in central collisions is one of the most important observables that constrain our choice of input parameters. For predictions of flow observables into the new energy domain, we thus had to extrapolate [74, 75] initial conditions adjusted to SPS multiplicities [76] by using the uncertain predictions of final state multiplicities resulting from other theoretical models [19]. To circumvent intrinsic uncertainties in the model predictions from this poorly controlled parameter, we presented our predictions as a function of the observed multiplicity density [74, 75]. The first analysis of non-central collisions at RHIC [2] excellently confirmed the hydrodynamic predictions of anisotropies in particle flow given in [75]. On the other hand, the anisotropies observed in experiments could not be described by any of the traditional microscopic models. Shortly before the publication of experimental flow anisotropies, the first RHIC publication by the PHOBOS collaboration confirmed the expected higher multiplicities and energy densities in this new domain [14] and fixed this crucial free parameter in the hydrodynamic model (thereby also eliminating the majority of the models presented in [19]). As experimental statistics for the flow analysis was improving and hydrodynamics turned out to apply *quantitatively*, it was necessary to also free our initial conditions as much from theoretically uncertain estimates as possible. Furthermore, experimental cuts such as momentum and rapidity acceptance had to be taken into account as they cause effects of up to 10 % in the studied observables [79]. In this way compelling agreement with further observables was found [77] and the predictions could be extended to study mass effects, earlier decoupling, and more [68]. Again, these more delicate hydrodynamic features were confirmed later in an experimental analysis by the STAR collaboration [9], after the data was analyzed in more detail to allow for the discrimination of particle species and refined centrality bins. Meanwhile the PHENIX collaboration reported the centrality dependence of particle multiplicities [3], freeing us of ambiguities in the initialization process which we had investigated in [78]. In a last step PHENIX presented single particle spectra for central collisions in a wide region of transverse momentum [127, 35], thus offering us the ultimate tool to precisely initialize our parameters. In addition this detailed information on particle production has also acquired higher statistics and smaller systematical errors than the previous multiplicity measurements. (Similar data from the STAR collaboration have not been finally released, but so far seem to be fully consistent with the PHENIX data and the hydrodynamic model.)

In this work, we do not repeat the historical succession of events, but rather give a detailed account of our converged understanding of the system's geometry and initial setup together with the input parameters required to describe the particle spectra from *central* RHIC collisions (see Chapter 2). With the parameters fixed in central collisions, the generalization to non-central collision results solely from geometrical effects and does not introduce further parameters – observables resulting from non-central collisions are thus clean predictions of the theory. Such predictions are of even more interest when we concentrate on observables which vanish in central collisions due to symmetry but arise from anisotropies in the initial configuration of non-central collisions. After obtaining a qualitative understanding of the system's evolution, we study quantitatively final state observables in the subsequent chapters. First, in Chapter 3, we investigate the centrality dependence of global transverse observables, i.e. the multiplicity, the mean transverse momentum, the mean transverse energy, the mean radial flow velocity and the particle spectra from collisions with non-zero impact parameter. In Chapter 4 we then focus on anisotropies in the particle emission patterns, and various dependencies of the *'elliptic flow'* in comparison with experimental results. To further elucidate this anisotropic particle emission, we also present more simple-minded but intuitive model calculations motivated by a so called *'blast wave* *model'*. By the end of Chapter 4 we will have shown that flow observables and the momentum space structure of the expansion are in excellent agreement with a hydrodynamic expansion scenario with short equilibration times.

In Chapter 5 we turn to the geometrical space-time aspects of the fireball's freeze-out configuration. Experimentally this geometry can be extracted with the measurement of HBT parameters for which the new experiments delivered stunning results far away from earlier predictions of all model calculations [6, 70]. The larger initial energies - so the simplest argument runs - should lead to largely increased system lifetimes and therefore also to larger emission durations, especially if the equation of state features a phase transition [66, 103]. No such signal was found, and the HBT parameters that characterize the space-time structure of the particle emitting source do not show large effects going from AGS to RHIC energies. The detailed hydrodynamic model is not able to explain the data either; therefore we will carefully study the origin of these discrepancies between theory and observation and offer a discussion of possible ways out of this dilemma. Important is that the momentum-space evolution is well described by the hydrodynamic description which requires that the system thermalizes rapidly. That the final space-time geometry of the source is not perfectly described by ideal hydrodynamics is to be expected due to the breakdown of the applicability of the hydrodynamic concepts in the late, dilute stages. Curiously, the long hadronic rescattering stages of hybrid models do not improve on the deviations, but lead to even larger discrepancies.

The technical details of the calculations are spared for the Appendix in order not to interrupt the flow of arguments with technical formalities. A short Glossary summarizes repeatedly occurring abbreviations and symbols.

1.4 REMARKS ON THE NOTATION

In the following we use natural units, strictly setting $c = k_{\rm B} = \hbar = 1$ as conventional and convenient in nuclear and high-energy physics. Furthermore we caution that y has a double meaning: In one case it serves as the second coordinate to describe a point in the transverse plane (x, y) - (a precise definition of our coordinate system is given in Section 2.1 and Appendix A). In the other case it characterizes the longitudinal rapidity $y = \mathrm{Artanh}\,(p_z/E)$ of a particle with p_z being the momentum component along the z-axis and E its total energy. Generally it is obvious which of the two meanings the specified y stands for. Sometimes however a situation arises where two different y's in one formula take on the two different meanings. Rather than trying to alter well established conventions we stick to the tradition in the field and avoid possible confusion from such occurrences by explaining the various meanings carefully when the need arises.

More confusing might be the notation for *pseudorapidity* and *space-time rapidity*, two very different quantities that have managed to acquire the same symbol. The pseudorapidity is a kinematic (momentum-space) variable of a particle. A particle with longitudinal momentum p_z and total momentum p has pseudorapidity $\eta = \frac{1}{2} \ln \frac{p+p_z}{p-p_z} = \text{Artanh}\,(p/p_z)$. The space-rapidity is a purely geometrical construct in coordinate space, resulting from a straightforward coordinate transformation to a set of coordinates that is especially useful in dealing with large longitudinal velocities as they appear in high energy collisions. It is defined (see Appendix A) as $\eta = \frac{1}{2} \ln \frac{t+z}{t-z} = \text{Artanh}\,(z/t)$. Again the context will determine in which meaning the symbol η is used.

Frequently we also deal with *four-vectors* and *four-coordinates*, where x gets a double meaning with $x \equiv x^\mu = (t, x, y, z)$, thus being used to denote either a full set of four space-time coordinates or simply the x-coordinate of a space-time point. Again, its usage will be clear from the context wherever this notation appears. The same convention is taken for the four momentum of particles, $p = p^\mu = (E, p_x, p_y, p_z)$. Three-vectors in coordinate space are written in bold face, e.g. $\mathbf{r} = (x, y, z)$, whereas vectors in only two dimensions are indicated by an arrow, e.g. $\vec{r}_\perp = (x, y)$. For clarity, momentum vectors in the transverse plane and their magnitudes often carry a lower case 'T' or $\perp$ sign.

2

EVOLUTION OF THE FIREBALL

Imagine two large nuclei being brought to collision with velocities close to the speed of light. To be more specific, think of two gold nuclei (mass number $A = 197$, radius $R_0 \approx 6.4$ fm) with a center of mass energy per nucleon pair of $\sqrt{s_{\mathrm{NN}}} = 130$ GeV. Under these conditions, each nucleus appears contracted by a gamma-factor $\gamma \approx 70$ and has a velocity of about 0.9999 times light-speed in the center of mass frame. Collisions of this kind were induced in the first year run of the Relativistic Heavy Ion Collider (RHIC) at Brookhaven National Laboratory (BNL).[1] Debris from those collisions was collected in 4 detectors around the ring holding the ion beams. Those detectors can only observe final state observables, far away (in terms of nuclear scales) from the collision zone and long after the collision dynamics has ceased. The challenge now is to find observables imprinted in the recorded final state which contain information on the initial conditions of the reaction and the subsequent collision dynamics to gather information about nuclear matter under the extreme conditions produced upon impact. Requiring consistency with an as large variety of observables as possible allows to accept or reject different model scenarios that are used for the description of the evolution of the system. This is the only way we have to study the dynamics of the system and learn about the properties of matter under the extreme conditions that were created. Later, we will exploit a large selection of data taken with the STAR, PHENIX and PHOBOS detectors that give support to the hydrodynamic expansion model of a relativistic heavy-ion collision which is presented in this chapter.

---

[1] From now on, we will refer to these conditions as 'RHIC 1'. In the year 2001, RHIC was running at full beam energy, with $\sqrt{s_{\mathrm{NN}}} = 200$ GeV. Collisions at these energies will be referred to with the label 'RHIC 2'.

2.1 GEOMETRY OF THE COLLISION

We first define the coordinate system of the collision. The center of momentum of the two nuclei sets the origin in momentum space, the collision point sets the origin along the beam direction in coordinate space. Initially the nuclei travel parallel to the z-axis with opposite momenta. The plane orthogonal to the z-axis, spanned by the x and y axes is called the *transverse plane*. If the collision is not central but the center of the nuclei are displaced by a finite impact parameter $\mathbf{b}$, the x-axis is set to point in the direction of $\mathbf{b}$. The z-axis and $\mathbf{b}$ span the *reaction plane*, Fig. 2.1.

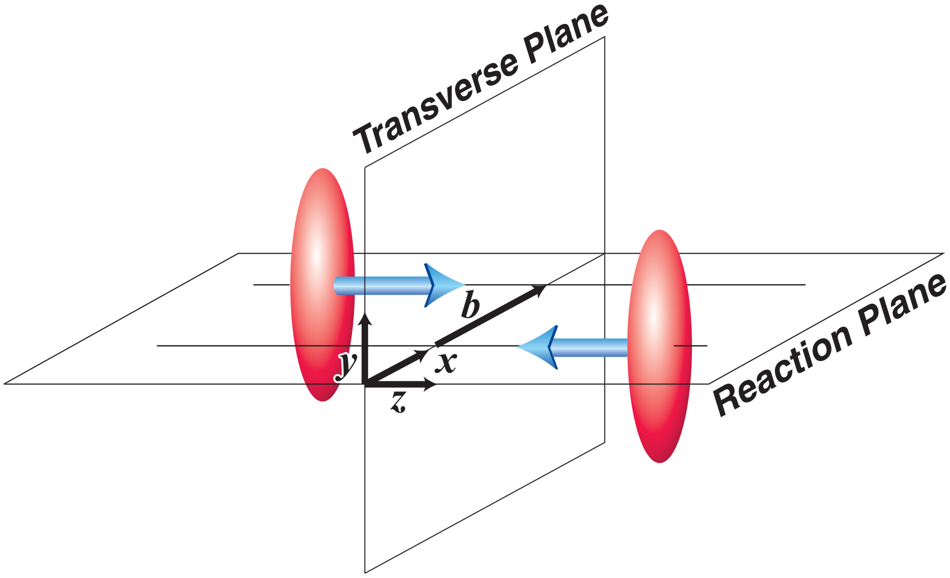

Figure 2.1: Definition of the transverse plane and the reaction plane, the coordinate system and impact parameter $\mathbf{b}$. The nuclei before the collision are indicated by ellipsoids (as a result of Lorentz contraction, not to scale), and their direction of motion by the bold arrows.

Such collisions with finite impact parameters are of special interest: Energy deposition in the reaction region is most efficient in central collisions, and by going to finite impact parameters one produces less entropy/energy in the collision. By systematically studying the centrality dependence of observables, one can thus in principle measure excitation functions of observables without varying the beam energy of the collider. However one carefully has to disentangle the geometric effects from those induced by the varying energy content and energy densities in the system. Excitation functions are especially interesting in the field, as they might show the most drastic signals when the energy density reaches the predicted transition region of the nuclear equation of state where the underlying degrees of freedom change.

Furthermore, changing the centrality changes the size of the system. This in turn is ideal to probe medium effects of observables. Colored particles which travel through a background field of a strongly interacting medium would experience a characteristic ‘energy loss’, which is the larger the bigger the strongly interacting medium is.

The most exciting physics can be expected from the broken azimuthal symmetry in non-central collision. The overlap of the two nuclei can lead to observables which are highly sensitive to their emission angle φ relative to the reaction plane. For example, this may be reflected in different energy loss of hard partons depending on their direction of emission. In this study, we will mainly address the anisotropic dynamical, collective effects arising from this initial spatial anisotropy.

To profit from these points it is essential to have a good understanding of the initial geometry of the system.

2.1.1 GLAUBER MODEL FOR THE COLLISION

Before the reaction, the density distribution of the two nuclei with mass number A is described by a Woods-Saxon parametrization

$$\rho_A(r) = \frac{\rho_0}{e^{(r-R_A)/\xi} + 1}\,, \tag{2.1}$$

with $R_A = (1.12\,A^{1/3} - 0.86\,A^{-1/3})$ fm. In the following we focus on Au+Au collisions with A=197 and use $\xi = 0.54$ fm for the surface diffuseness [29]. The normalization factor ρ_0 is set to give $\int d^3r \rho_A(r) = A$. With these parameters we have $\rho_0 = 0.17$ fm^{-3}.

The relevant quantity for the following considerations is the *nuclear thickness function*, which integrates the nuclear density function over the longitudinal coordinate z:

$$T_A(x,\,y) = \int_{-\infty}^{\infty} dz\,\rho_A(x,\,y,\,z)\,. \tag{2.2}$$

The opacity of the nucleus is obtained simply by multiplying the thickness function with the total inelastic cross section σ_0 of a nucleon nucleon collision. At $\sqrt{s_{\rm NN}} = 130$ GeV we use $\sigma_0 = 40$ mb [52].

WOUNDED NUCLEONS

Wounded nucleons are nucleons that interact at least once in the collision.[2] Their number is of special interest, as they are thought to be responsible for the bulk of soft particle production and energy deposition in nuclear collisions: at SPS energies it was observed that the number of final state particles scales linearly with the number of wounded nucleons [11]. Deviations from such a scaling as they are now observed at RHIC energies give hints for the onset of new scattering mechanisms [3, 24, 18].

Statistical considerations allow to express the density of wounded nucleons in the transverse plane in terms of the nuclear thickness function of one nucleus, multiplied with a combinatorial factor involving the nuclear thickness function of its collision partner. This factor ensures that the participating nucleon does not penetrate the finite opposing nuclear matter without interaction [25]. For symmetric and central collisions this reads

$$n_{\mathrm{WN}}(r) = 2\,T_A(r)\left(1-\left(1-\frac{\sigma_0 T_A(r)}{A}\right)^A\right)\,, \tag{2.3}$$

where $r = \sqrt{x^2+y^2}$ is the radial distance from the origin. This functional dependence is displayed by the solid line in Fig. 2.2 for the Au+Au collisions of our studies (due to the energy dependence of the nucleon cross section σ_0, it depends slightly on the beam energy of the collision).

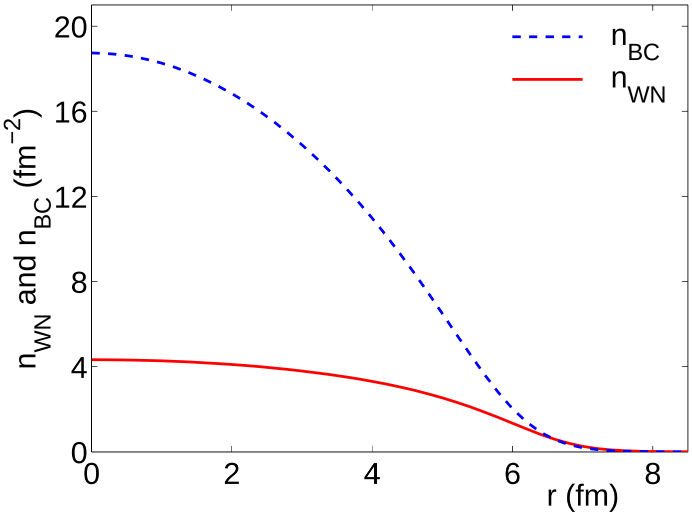

Figure 2.2: Density of wounded nucleons (n_{WN}) and binary collisions (n_{BC}) in the transverse plane as function of the radial distance from the origin, with parameters corresponding to central Au+Au collisions at $\sqrt{s_{\mathrm{NN}}} = 130$ GeV.

---

[2] Synonymously used is ‘Participants’ or ‘Participant Nucleons’.

More generally, non-central collisions of spherical nuclei with different mass numbers A and B separated by the impact parameter b produce a density of wounded nucleons according to

$$\begin{aligned} n_{\mathrm{WN}}(x,y;\,b) \;=\;& T_A(x+b/2,y)\left(1-\left(1-\frac{\sigma_0 T_B(x-b/2,y)}{B}\right)^B\right) \\ &+T_B(x-b/2,y)\left(1-\left(1-\frac{\sigma_0 T_A(x+b/2,y)}{A}\right)^A\right)\,. \end{aligned} \tag{2.4}$$

where the thickness function of each nucleus is simply shifted by $\pm b/2$ to the left or to the right along the x-axis to meet the thickness function of the other nucleus shifted in the other direction. Integrating the above expression over the transverse plane yields the total number of wounded nucleons (or number of participants) as function of the impact parameter, $N_{\mathrm{WN}}(b) = \int dx\,dy\; n_{\mathrm{WN}}(x,y;\,b)$. For central RHIC 1 collisions it predicts $\approx$ 378 wounded nucleons. In reality fluctuations occur: collisions at a certain impact parameter sometimes produce more and sometimes less wounded nucleons as a result from the microscopical structure of the nuclei and scattering events [73]. In this sense the numbers evaluated in this Glauber formulation [51, 132] can be seen as average numbers of wounded nucleons at fixed impact parameter. The centrality dependence, which also reflects the centrality dependence of the system's effective size, is displayed in Figure 2.3.

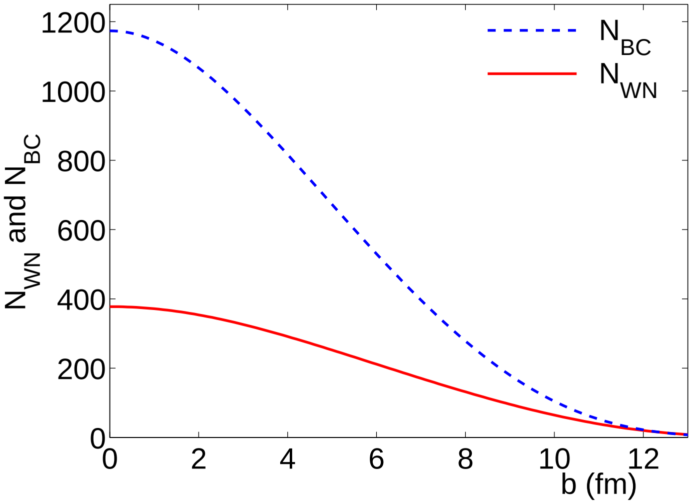

Figure 2.3: Centrality dependence of the total number of wounded nucleons (N_{WN}) and binary collisions (N_{BC}) with parameters corresponding to Au+Au collisions at $\sqrt{s_{\mathrm{NN}}} = 130$ GeV.

BINARY COLLISIONS

The density of binary collisions becomes of interest in the high energy limit. After suffering their first collisions, the partons travel on through the nuclear medium and are eligible for further (hard) collisions with other partons. This leads to the notion that one has to count the binary collisions, and the density of their occurrence in the transverse plane is expressed simply by the product of the thickness function of one nucleus with the encountered opacity of the other nucleus, leading to the squared thickness function

$$n_{\mathrm{BC}}(r) = \sigma_0 \, T_A^2(r) \,, \tag{2.5}$$

in symmetric and central collisions. This distribution of binary collisions is much more strongly peaked toward the center of the collision than the density of wounded nucleons (dashed line in Fig. 2.2).

Again the formula generalizes to non-central $A+B$ collisions simply by taking an offset of $\pm b/2$ along the x direction of the two nuclei to become

$$n_{\mathrm{BC}}(x, y;\, b) = \sigma_0 \, T_A(x + b/2, y) \, T_B(x - b/2, y) \,. \tag{2.6}$$

The total number of binary collisions, $N_{\mathrm{BC}}(b) = \int dx\, dy\, n_{\mathrm{BC}}(x, y;\, b)$, also shows a larger sensitivity on the impact parameter than does the total number of wounded nucleons (dashed line in Fig. 2.3).

With increasing impact parameter the density of wounded nucleons and binary collision of the system in the center of the fireball, at $(x,\, y) = (0,\, 0)$ decreases as well, see Fig. 2.4. This is the fact which we exploit when regarding centrality

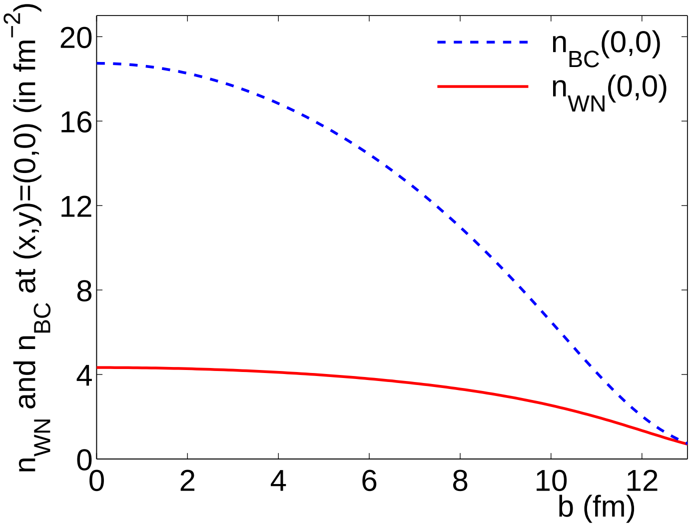

Figure 2.4: Centrality dependence of the density of wounded nucleons (n_{WN}) and the density of binary collisions (n_{BC}) in the center of a collision for parameters corresponding to Au+Au collisions at $\sqrt{s_{\mathrm{NN}}} = 130$ GeV.

dependencies as excitation functions. Again, the effect as predicted by Eqs. (2.4) and (2.6) is more drastic for the binary collision case.

For the subsequent expansion of the fireball matter we assume a hydrodynamic expansion as described in Section 2.2. As already discussed in the introduction such an approach can only be valid for a large enough system with large enough densities so that the mean free paths of the particles are much smaller than the system size. Even if these prerequisites are fulfilled in the most central collisions (for which we will present arguments in the following), it is expected that they will be violated in very peripheral collisions, see Figs. 2.3 and 2.4. At some impact parameter, the hydrodynamic limit will gradually break down and non-flow effects take over in more peripheral collisions.

ANISOTROPIES IN THE INITIAL CONDITIONS

For collisions with finite impact parameters the density fields of wounded nucleons and binary collisions feature pronounced anisotropies in the transverse plane. As an example, Fig. 2.5 shows contours of constant densities of binary collisions, Eq. (2.6), for a Au+Au collision with impact parameter $b = 7$ fm. The dashed circles indicate the Woods-Saxon circumferences of the Au nuclei separated by 7 fm (the centers of the nuclei are marked by smaller crossed circles).

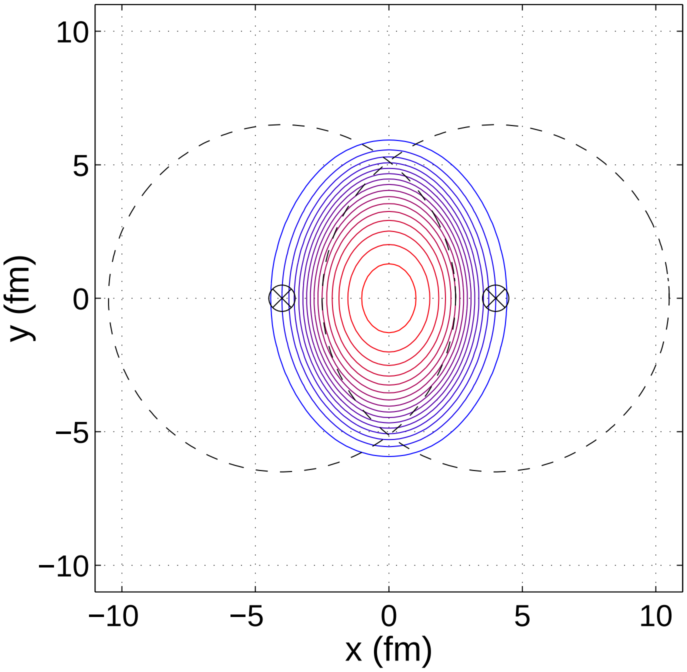

Figure 2.5: Contours of constant densities of binary collisions for Au+Au collisions with $b = 7$ fm at $\sqrt{s_{\mathrm{NN}}} = 130$ GeV. The contours are given for 5, 15, 25, ... percent of the maximum value (which here is 12.8 fm^{-2}).
The dashed circles indicate the Woods-Saxon circumferences of the colliding nuclei.

The strong asymmetry in the azimuthal angle $\varphi_s = \arctan(y/x)$ of the initial distribution is apparent. Quantitatively the initial spatial anisotropy can be characterized by

$$\epsilon_x = \frac{\langle\langle y^2 - x^2 \rangle\rangle}{\langle\langle y^2 + x^2 \rangle\rangle}\,, \tag{2.7}$$

where the averages are taken over the relevant density function under investigation. As function of impact parameter, the spatial anisotropy rises quickly up to a maximum of $\sim 40\%$ before it drops to 0 again in the most peripheral collisions, Fig. 2.6. The distribution of binary collisions is more sharply peaked in the transverse plane and shows larger anisotropies in semi-central collisions up to $b \sim 11$ fm. In Section 2.5 we will discuss how this initial asymmetry is carried over to the final state observables.

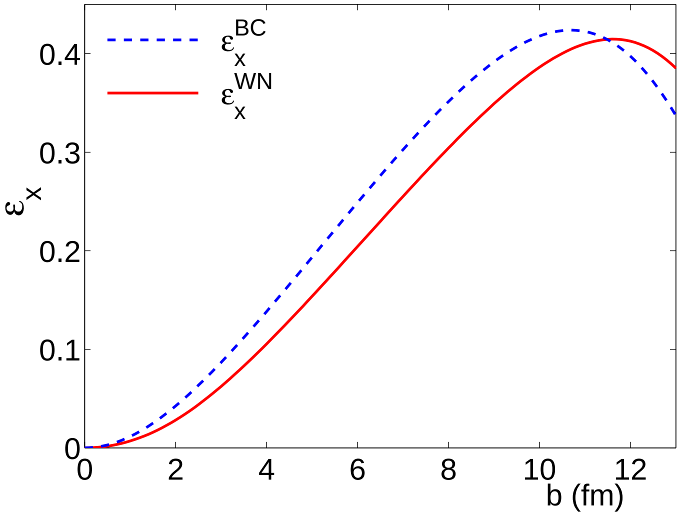

Figure 2.6: Spatial anisotropy of the initial overlap region in the binary collision (ϵ_x^{BC}) and wounded nucleon (ϵ_x^{WN}) distribution for Au+Au collisions at $\sqrt{s_{\mathrm{NN}}} = 130$ GeV.

2.1.2 ENERGY VERSUS ENTROPY DEPOSITION

In the following, we assume that the initial state of the matter in the transverse plane is governed entirely by the physics of “soft” and “hard” processes represented in terms of the densities of wounded nucleons and binary collisions, respectively. Shadowing effects by the spectators, i.e. the nucleons that do not suffer any interaction in the collision, do not play a role at RHIC energies, as the spectators leave the transverse plane at $z = 0$ in a timescale of less than 1 fm/c. We will come back to discuss the interesting physics resulting from spectator matter at lower energies in Chapter 4.

Whether the energy or entropy deposited in the collision region scales with the (density) of wounded nucleons or binary collisions is not clear from first principles. Data from the SPS [11] suggest that the final state particle multiplicity is proportional to the number of wounded nucleons. As the hydrodynamic evolution largely conserves entropy [82] (apart from some entropy generation in shock waves – discontinuities in the thermodynamic fields which can arise under the influence of a strong phase transition), traditional hydrodynamic approaches initialize the evolution by setting the initial entropy density proportional to the density of wounded nucleons [92]. At RHIC 1 energies (and most recently at full beam energy [24, 18]) it was found that the particle production per participating nucleon is no longer a constant, but rather a function increasing with centrality [3], which is attributed to a significant contribution from hard processes, scaling with the number of binary collisions. The PHENIX collaboration parameterizes the centrality dependence of the produced charged hadron yield as $dN_{ch}/d\eta = AN_{\mathrm{WN}} + BN_{\mathrm{BC}}$ with $A = 0.88 \pm 0.28$ and $B = 0.34 \mp 0.12$ [3], whereas others [73] find a combination $B/A = 0.198$ more suitable.[3]

To get a clear view of the significance of the initialization process, we investigated four different cases, assuming the initial energy density to be proportional to the density of wounded nucleons or binary collisions (labeled 'e_{WN}' and 'e_{BC}' in the following) or, alternatively, to have the initial entropy density being proportional to the density of wounded nucleons or binary collisions (labeled 's_{WN}' and 's_{BC}' respectively) [78]. Assuming thermalization at the time when the hydrodynamic evolution begins, the entropy density can then in turn be related to the energy density via thermodynamic identities (see Section 2.2.2). For the different initializations, the resulting energy densities as a function of the radial distance from the origin are displayed in Fig. 2.7 for central collisions. In each case, the energy density is normalized in such a way that at the end of the hydrodynamic evolution the same particle multiplicity is obtained in central collisions, $dN_{\mathrm{ch}}/dy = 670$. This value was motivated by the first measurement in this new energy domain [14] (the details on the evaluation of particle multiplicities follow in Sections 2.3 and 2.4). It is important to note that the entropy-initializations lead to more pronounced maxima in the energy-density distributions than their energy-initialization counterparts, which is a result of the connection $e \sim s^{4/3}$ [28] in the high energy density (quark-gluon plasma) phase of hadronic matter, Section 2.2.2. In addition we have learned from Figs. 2.3 and 2.4, that the binary collision distributions react more sensitively to variations of the impact parameter. Taken together, we can expect that the total energy and entropy deposition in the transverse plane is quite sensitive to the initialization. This is directly re-

---

[3] The extraction of the contribution of hard collisions relies strongly on data extracted from the most peripheral collisions. There, the determination of the number of wounded nucleons carries along strong model dependencies. At the time the fractional contribution of strong processes therefore has a large uncertainty.

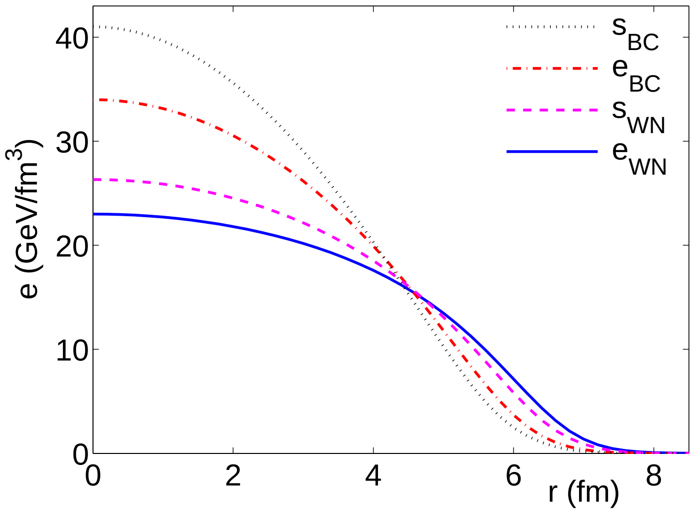

Figure 2.7: Radial dependence of the initial energy density for the different assumptions of choosing either the energy (e) or the entropy density (s) proportional to the density of wounded nucleons (subscript WN) or binary collisions (subscript BC). The curves are normalized to yield the same particle multiplicity $dN_{\rm ch}/dy = 670$.

flected in the centrality dependence of the final particle multiplicity per wounded nucleon; it is displayed in Fig. 2.8 together with experimental data from the PHENIX [3] and the PHOBOS collaboration [14, 15]. The two extreme cases of $e_{\rm WN}$ and $s_{\rm BC}$ show quantitatively completely different behaviors. $e_{\rm WN}$ leads to increasing particle production per participating nucleon pair, as the system gets smaller. In contrast, the data show that the particle production per participant pair increases for more central collisions, which requires a significant contribution from the binary collision distribution. In the following we therefore attribute 75% of the total generated entropy to the wounded nucleons and 25% to the binary collisions, using $s(x,y) = 0.75\, s_{\rm WN}(x,y) + 0.25\, s_{\rm BC}(x,y)$ where $s_{\rm XX} \propto n_{\rm XX}$ are indi-

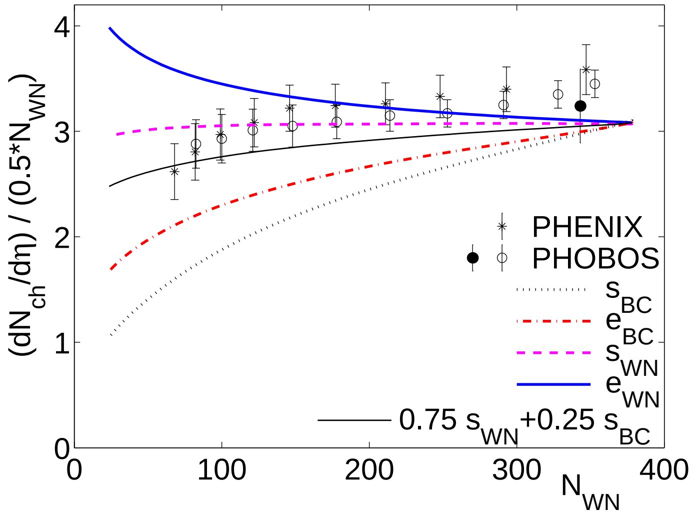

Figure 2.8: Particle production per participating nucleon pair as function of centrality (given in terms of wounded nucleons) for the different model initializations as in Fig. (2.7), together with data from PHENIX [3] and PHOBOS [14, 15].

vidually normalized to the same maximum value $s_{\mathrm{equ}}(0,0)$ at equilibration which is an input parameter directly related to the final particle multiplicity (Section 2.4). With this ratio, the centrality dependence of the particle multiplicity follows the experimental trend (see Figs. 2.8 and 3.4). We return to the hydrodynamic centrality dependence of particle multiplicities in the context of other centrality dependent observables in Chapter 3. As a side remark we point out a surprising agreement of the results from the e_{WN} initialization and the centrality dependence resulting from a perturbative QCD calculation in terms of a saturation model, which limits the gluonic multiplicity and density geometrically [48, 78].

2.2 HYDRODYNAMIC EXPANSION

While the nuclei are penetrating each other during the first fractions of a fm/c, they liberate the quarks and gluons described by their nuclear structure functions and produce secondaries, leading to large particle- and entropy densities with distributions that were discussed in the previous section. The tightly packed partons then rescatter with each other and, if the rescattering is intense enough, local thermal equilibrium is established before the particles disperse. The system can then be characterized in terms of macroscopic fields, its pressure, temperature, flow velocity, etc. and the subsequent evolution is governed by the laws of hydrodynamics. Whereas it is by no means evident that equilibrium concepts might be applicable in those violent collisions, this approach to the description of nuclear collisions is of unique beauty as the laws of hydrodynamics are simply a manifestation of the fundamental laws of energy and momentum conservation. The application of hydrodynamic concepts to nuclear collisions has thus a long tradition [81], and sophisticated methods and algorithms for the solution of the hydrodynamic equations of motion have been developed. Ultimately it appears that at RHIC collision energy and the sizes of the collision system have reached the prerequisites for the applicability of thermodynamic concepts already at very early times after the collision. The respective arguments are presented in the forthcoming chapters. In this section we discuss the hydrodynamic equations of motion, and the time evolution of the fireball until freeze-out.

2.2.1 EQUATIONS OF MOTION

The dynamics of a system in local thermal equilibrium can be described by the local conservation laws of energy and momentum, together with conservation laws for conserved currents like charge, baryon number, strangeness, etc. In its simplest form, neglecting non-ideal and dissipative effects, the relativistic energy-momentum tensor of a fluid is given by

$$T^{\mu\nu}(x) = \left(e(x) + P(x)\right) u^{\mu}(x) u^{\nu}(x) - g^{\mu\nu} P(x)\,, \tag{2.8}$$

where $e(x)$ and $P(x)$ is the energy-density and pressure at space-time point $x = x^{\mu} = (t, x, y, z)$. The fluid moves with the four velocity $u^{\mu}(x) = \gamma\,(1,\, \mathbf{v}(x))$ where γ is the Lorentz-factor $\gamma = (1 - \mathbf{v}^2)^{-1/2}$. The tensor $g^{\mu\nu}$ describes the space-time geometry in a standard Minkowski metric given by $g^{\mu\nu} = \mathrm{diag}(1,\, -1,\, -1,\, -1)$. For a fluid at rest, or in the comoving frame of a certain fluid cell with non-zero velocity, the energy momentum tensor reduces to $T^{\mu\nu} = \mathrm{diag}\,(e,\, P,\, P,\, P)$. The general equation (2.8) can be retrieved from this trivial expression by Lorentz-boosting it to a frame with velocity $u^{\mu}(x)$. Non-ideal features of the fluid such as bulk or shear viscosity and heat conductivity could be included by introducing additional terms in the energy momentum tensor [40]. However they lead to a large number of additional parameters and therefore blur the simplicity of the hydrodynamic scheme and its interpretation. We will return to this point and discuss the effects of such non-ideal generalizations in Section 5.4.2.

The conservation of energy and momentum is achieved by requiring that the four-divergence of the energy momentum tensor vanishes, leading to four coupled equations (Greek indices run from 0 to 3 and indices appearing twice are to be summed over):

$$\partial_{\mu} T^{\mu\nu}(x) = 0\,, \qquad (\nu = 0,\, \dots\,, 3)\,. \tag{2.9}$$

Furthermore we consider the conservation of (net) baryon number

$$\partial_{\mu}\, j^{\mu}(x) = 0\,, \tag{2.10}$$

where $j^{\mu}(x) = n(x)\, u^{\mu}(x)$ is the baryon current and $n(x)$ is the net baryon number density. As we have no net strangeness in the initial stage of the collision, there are no strangeness currents to be determined in our analysis.

Altogether we are left with 5 equations of motion, Eqs. (2.9) and (2.10), which ultimately determine the idealized time evolution of the system, expressed by the 6 fields – energy density, baryon density, pressure, and the three independent velocity fields of the four velocity. The system of equations is closed by thermodynamic relations between the thermodynamic fields. Once a proper thermodynamic potential for the medium is given, energy density, baryon density and pressure are related by the so-called equation of state from which also the entropy, temperature and chemical potentials can be derived.

2.2.2 EQUATION OF STATE

From the microscopic point of view, the energy momentum tensor of a system built up by particles of different species i, which are distributed in phase-space according to $f_i(x,\,p)$ is given by kinetic theory as

$$T^{\mu\nu}(x) = \sum_{i,\,\mathrm{species}} \frac{g_i}{(2\pi)^3} \int \frac{d^3p}{E_i}\, p^\mu p^\nu f_i(x,\,p)\,, \tag{2.11}$$

with $E_i = \sqrt{m_i^2 + \mathbf{p}^2}$ and m_i being the mass of particles of species i and g_i is their spin-isospin degeneracy. If the system is in thermodynamic equilibrium, the particles are distributed in the local rest-frame according to their statistical properties ('$+/-$' for Fermions/Bosons), by

$$f_i(x,\,p) = \frac{1}{e^{\beta(x)[E_i(p)-\mu_i(x)]} \pm 1} \tag{2.12}$$

with a common (local) temperature $T(x) = 1/\beta(x)$ but possibly different chemical potentials (or sets of chemical potentials) $\mu_i(x)$.

By comparison with the diagonal components of the hydrodynamic energy-momentum tensor in the local rest-frame of a fluid cell, we see that the local pressure in such a system is given by

$$P = \sum_{i,\,\mathrm{species}} \frac{g_i}{(2\pi)^3} \int \frac{d^3p}{E_i} \frac{\mathbf{p}^2}{3}\, f_i(x\,,p)\,. \tag{2.13}$$

Knowing the pressure as a function of the temperature and the chemical potentials, we can evaluate the densities of the conserved currents by taking the derivatives with respect to the corresponding chemical potential. For example for the baryon density we have $n_B = -\partial\Omega/\partial\mu_B = \partial P/\partial\mu_B$, and the entropy density is given as the temperature derivative of the pressure $s = -\partial\Omega/\partial T = \partial P/\partial T$. Having those thermodynamic fields evaluated we can access the energy density e with help of the thermodynamic identity

$$Ts = e + P - \sum_i \mu_i\, n_i\,, \tag{2.14}$$

where the sum runs over all conserved charges.

An equation of state obtained in this manner assumes point-like non-interacting particles and thus does not contain effects that might arise from the intrinsic volume of the hadrons themselves. An attempt to correct for those effects is the proper volume correction which leads to an increased total volume

$V = V_{\text{avail}} + e/(4B)$, where e is the energy-density in the uncorrected volume and B is the so called *bag-constant*, which can also be seen as the potential confining the partons into the hadrons. Its value is usually taken to be around $B^{1/4} \approx 230$ MeV. Thermodynamically, this proper volume correction leads to small inconsistencies, as it does not give the correct relative particle abundances contributing to the total pressure $n_i = \partial P/\partial\mu_i$. In practice, this is known to lead to only small corrections, which do not largely influence the resulting equation of state and the subsequent hydrodynamic evolution of matter [83, 102, 124].

It was already argued in the introduction that a change of the underlying degrees of freedom is to be expected, when we bring the system under extreme conditions of heat and/or pressure. Then the individual hadrons are so tightly packed that their confining shells begin to overlap and might break open to liberate the formerly confined quarks and gluons. This intuitive picture gets strong support from lattice QCD, where the proportionality constant between energy density and the fourth power of temperature shows a sharp jump when strongly interacting matter is heated above a certain critical transition temperature [46, 95]. If we are in fact dealing with a gas of liberated quarks and gluons at the high temperature end of the phase diagram, then the equation of state is simply given as the one for an ultrarelativistic gas of massless quarks and gluons, readily evaluated as described in Eq. (2.13). Eventually one ends up with the simple relation between pressure and energy density typical for any gas of massless, point-like particles [28]

$$P = e/3\,. \tag{2.15}$$

We only have to subtract the pressure that the QCD vacuum outside of the fireball exerts on the partons inside the fireball to end up with $P_{\text{QGP}} = e/3 - B$. The transition between the hadronic and plasma stage then occurs at the line of equal pressure $P_{\text{had}} = P_{\text{QGP}}$. The critical temperature of this equation of state is $T_{\text{crit}} = 164$ MeV. (This was achieved by choosing $B^{1/4} = 230$ MeV such that T_{crit} reproduces the lattice data.) Furthermore, the thermodynamic relations then determine the critical energy density, which we find with our choice of B to be $e_{\text{crit}} = 0.45$ GeV/fm^3 and a the latent heat of $\Delta e = 1.15$ GeV/fm^3. The dependence of the pressure on energy- and baryon density is displayed in Fig. 2.9. The strong first order phase transition is a prominent feature of all equations of state constructed in such a way. We will discuss its influence on the evolution of the system and certain observables in other sections. To do so, we will also perform calculations with the very hard equation of state of the ideal gas without a phase transition, $p = e/3$ (EOS I) and the soft equation of state of purely hadronic matter $p \approx 0.15\,e$ (EOS H) extended to arbitrarily large energy densities.

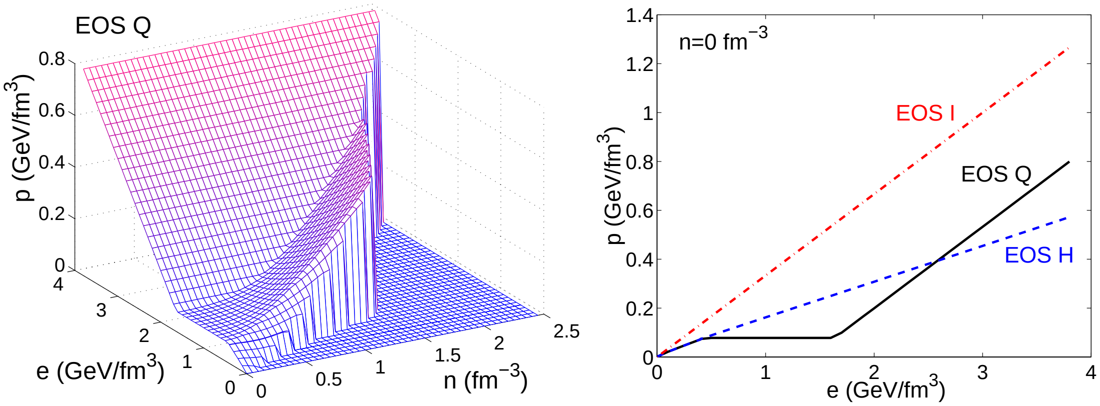

Figure 2.9: Equation of state with a strong first order phase transition as described in the text. The left figure shows the dependence of pressure on energy- and baryon density. The right figure shows the relation between pressure and energy density for this equation of state at vanishing baryon density together with the equation of state for an ideal gas (EOS I) and a hadronic resonance gas (EOS H).

2.2.3 LONGITUDINAL BJORKEN FLOW

Before the collision, the two interacting nuclei have large longitudinal velocities. This motion is partially carried over to the fireball matter created in the collision. Then, just like in the expanding universe, matter can only have reached a distance z from its origin within a time t, if it has been traveling with velocity z/t. For the radial expansion of the universe this kind of velocity field is called 'Hubble expansion', for the longitudinal expansion of an ultrarelativistic heavy-ion collision, $v_z = z/t$, it is named 'Bjorken flow' field [27]. Other studies have shown that the hydrodynamic equations preserve this flow field in time [119]. In collisions, however, this flow field can only hold in a finite window around $z = 0$, as due to causality matter is confined to regions where z/t is less or equal the speed of the initial nuclei, which is still a little smaller than the speed of light. For experimental observables, a perfect Bjorken flow field translates into observables which do not show any dependence on the rapidity $y = \text{Artanh}\,(p_z/E)$ (*boost invariance*). For RHIC 1 experiments there are indications that boost invariance holds well for a window reaching over almost four units of rapidity [16, 93, 79]. Fully four dimensional calculations indicate that the concepts of boost invariance and early thermalization hold in a pseudorapidity range of about 2 units [65].

In contrast to the strong longitudinal dynamics already present before impact, initially there is essentially no motion transverse to the beam direction. Transverse dynamical observables are thus a direct product of the fireball evolution, whereas dynamically generated observables along beam direction are difficult to disentangle from the initial motion of the nuclei (but they also exhibit interesting physics, see [63] for an extensive review). Furthermore in experiments with equal nuclei at collider facilities such as RHIC, the main detectors are centered around the transverse plane at midrapidity. In this work, we want to make use of the wealth of transverse observables collected in the first year of RHIC. We therefore implement the boost-invariant longitudinal velocity field directly into the equations of motion Eq. (2.9) and (2.10) to reduce the numerical costs of the calculations. The reduction of the 5 equations of motion to 4 non-trivial ones is most easily done by a coordinate transformation from Minkowski coordinates to rapidity coordinates via

$$x^\mu = (t, x, y, z) \longrightarrow \bar{x}^m = (\tau, x, y, \eta)$$

$$\begin{array}{rclrcl} t & = & \tau\cosh\eta & \qquad \tau & = & \sqrt{t^2 - z^2} \\ z & = & \tau\sinh\eta\,, & \qquad \eta & = & \mathrm{Artanh}\,(z/t)\,. \end{array} \tag{2.16}$$

Here η is named the (longitudinal) space-time rapidity and τ the (longitudinal) proper time. After implementing the longitudinal flow field $v_z = z/t$, we finally arrive at the equations of motion in this chosen coordinate system[4]

$$T^{\tau\tau}{}_{,\tau} + \left(\bar{v}_x T^{\tau\tau}\right)_{,x} + \left(\bar{v}_y T^{\tau\tau}\right)_{,y} = -\frac{1}{\tau}\left(T^{\tau\tau} + P\right) - \left(P\bar{v}_x\right)_{,x} - \left(P\bar{v}_y\right)_{,y}\,, \tag{2.17}$$

$$T^{\tau x}{}_{,\tau} + \left(\bar{v}_x T^{\tau x}\right)_{,x} + \left(\bar{v}_y T^{\tau x}\right)_{,y} = -P_{,x} - \frac{1}{\tau} T^{\tau x}\,, \tag{2.18}$$

$$T^{\tau y}{}_{,\tau} + \left(\bar{v}_x T^{\tau y}\right)_{,x} + \left(\bar{v}_y T^{\tau y}\right)_{,y} = -P_{,y} - \frac{1}{\tau} T^{\tau y}\,, \tag{2.19}$$

$$\frac{1}{\tau^2} P_{,\eta} = 0\,, \tag{2.20}$$

$$j^\tau{}_{,\tau} + (\bar{v}_x j^\tau)_{,x} + (\bar{v}_y j^\tau)_{,y} = -\frac{1}{\tau} j^\tau\,, \tag{2.21}$$

where the lower case comma and coordinate are an abbreviation for the partial derivative with respect to this coordinate, e.g. $f_{,\tau} \equiv \partial f/\partial\tau$. Furthermore we have introduced the abbreviation $\bar{v}_i = v_i \cosh\eta$.

This is still a full system of 5 equations, but now the 4th equation decouples trivially. The longitudinal Bjorken flow field directly leads to a pressure field

---

[4] The detailed intermediate steps of the derivation are given in Appendix A.

that is independent of space-time rapidity η. Furthermore no derivatives on η appear in the other equations, implying that the assumed initial boost-invariance (η–dependence) is preserved in time. Thus we have effectively reduced the dimensionality of the full problem.

Note the appearance of the factors of $-1/\tau$ on the right-hand sides of the equations. These loss terms result from the longitudinal flow field. If the system's evolution starts early, the longitudinal loss from a small slice dz around $z = 0$ will be large as the longitudinal transport with $v_z = z/t$ will be larger.

The ideal hydrodynamic equations of motion also conserve entropy [82]:

$$\partial_\mu \, s^\mu = 0 \, . \tag{2.22}$$

Here s^μ is the entropy current $s^\mu(x) = s(x) \, u^\mu(x)$ where $s(x)$ is the entropy density. As exercised in Appendix A.1.2 for the conservation of baryon number (Equation A.15), implementing boost-invariance in such a continuity equation turns it to $\partial_\tau(\tau s^0(x)) + \partial_x(\tau s^1(x)) + \partial_y(\tau s^2(x)) = 0$. Integrating this equation over the transverse plane (and assuming that the entropy field vanishes at large distances) we find that $\partial_\tau \int dxdy \, \gamma \tau s = 0$ and therefore the entropy per unit rapidity $\tau_0 \, dS/dz = dS/dy$ is a conserved quantity. In turn the entropy is proportional to the final particle yield, $dS/dy \propto dN/dy$.

2.3 FREEZE-OUT

As discussed in the introduction, the applicability of hydrodynamic concepts is limited (and therefore it is of extreme interest that hydrodynamic laws in fact do apply!). Prerequisites for hydrodynamics are a sufficiently large system with large particle densities together with short rescattering lengths. Furthermore, the system has to be in local thermal equilibrium. If we happen to have created such a system by colliding two heavy ions, liberating their gluons and creating enough secondary particles, so that thermodynamic aspects do apply, the subsequent dynamical expansion and the strong radial velocities that build up during the system's evolution will at some point clearly render the approximations of high density and short rescattering lengths invalid. More precisely, there is a gradual transition from the dense interior center of the fireball towards the lower densities at larger distances from the center. With passing time and continuous dilution, the hydrodynamic approximation gets worse and worse in a larger and larger fraction of the fireball volume, until finally the system is so dilute and the densities $\rho_j(x)$ of species j get so small that the average time between individual scattering events with particles of species i (with cross section σ_{ij} and relative velocity

v_{ij}), which is given as $\Delta\tau_{\rm scatt} = 1/\sum_j \langle\sigma_{ij} v_{ij}\rangle \rho_j(x)$, becomes of the order of the expansion time-scale of the collision $\partial_\mu u^\mu(x)$. Then the particles stop interacting and travel off freely to the detectors, to hopefully leave traces and signatures in the detectors that allow for the particles' detection and identification. From this discussion, one sees that different particle species decouple from the system at different times due to largely varying cross-sections [107, 108, 67]. The difference in the cross-sections for the most abundant mesons and hadrons is however not too large, only the heavy strange particles show larger deviations from the common freeze-out trend. The particle density in the denominator for the expression of the scattering timescale is a steep function of temperature. Therefore the freeze-out prescription is almost identical to freezing out the particles from fluid cells which have reached a certain *freeze-out temperature* $T_{\rm dec}$ [107]. For baryon-poor matter at $n \approx 0$, this again is essentially identical to employing freeze-out of fluid cells that have reached a certain limiting energy density $e_{\rm dec}$. The latter is our choice of method, as it is of higher numerical accuracy.

With the initial conditions given, the equations of motion and the equation of state tells us how the system builds up flow, dilutes and cools down. By solving the equations of motion we therefore also get the proper time evolution of the hypersurface (the time evolution of a surface in three-dimensional coordinate space) of constant freeze-out energy density, which we denote by Σ. At freeze-out we assume that every infinitesimal part of this hypersurface behaves as a simple black body source of particles. Its thermal spectra for the individual hadrons i are given by the equilibrium distributions as in Eq. (2.12), $f_i(E,x) = 1/(2\pi)^3 \left\{\exp[\beta(x)(E-\mu_i(x))] \pm 1\right\}^{-1}$, corresponding to the temperature $T(x) = 1/\beta(x)$ and chemical potential $\mu_i(x)$ at the space-time point of the source-cell. ($f_i(E,x)$ just describes the thermal energy distribution in the local rest-frame.) The collective velocity of the fluid on the hypersurface which results from longitudinal and transverse flow is taken into account by using the invariant expression $E = E(x) = p^\mu u_\mu(x)$. The transverse flow component leads to a transverse boost or a *blue-shift* of the transverse momentum spectra [84]. The total spectrum for particles of species i (with degeneracy g_i) is then achieved by integrating over all infinitesimal source contributions σ^μ on the surface Σ. This then leads to the so called Cooper-Frye prescription [39]

$$E\frac{dN}{d^3p} = \frac{dN}{dy p_{\rm T} dp_{\rm T} d\varphi_p} = g_i \int_\Sigma f(u_\mu p^\mu, x) p_\mu d^3\sigma^\mu\,, \tag{2.23}$$

giving the multiplicity of particles with the specified kinematic properties. In the boost-invariant system the freeze-out hypersurface is independent of η and the hypersurface is therefore parameterized by only two coordinates, i.e. by the freeze-out time τ_f as a function of the transverse coordinates (x, y). Within such a parametrization, which we determine by the numerical solution of the hydrodynamic equations of motions, the particle spectra are given as[5]

$$\begin{aligned}\frac{dN}{dy dp_x dp_y} &= \frac{2g_i}{(2\pi)^3} \int dx dy \, \tau_f(x,y) \sum_{n=1}^{\infty} (\mp 1)^{n+1} e^{\frac{n}{T}[\gamma(v_x p_x + v_y p_y)+\mu_i]} \times \\ &\times \left[m_{\mathrm{T}} \mathrm{K}_1\left(n\beta_\perp\right) - p_x \frac{\partial \tau_f(x,y)}{\partial x} \mathrm{K}_0\left(n\beta_\perp\right) - p_y \frac{\partial \tau_f(x,y)}{\partial y} \mathrm{K}_0\left(n\beta_\perp\right) \right] .\end{aligned} \tag{2.24}$$

with $\beta_\perp = \gamma \, m_{\mathrm{T}}/T$.

The validity of this approach has been widely discussed in the literature, and improvements of various kinds have been proposed. The main criticism arises from the point that some fluid cells in this formalism (in particular the ones with space-like normalvector) would also radiate particles backwards into the fluid. Therefore some authors introduce sharp $\Theta-$functions eliminating those particles from the spectra, which however cuts back on energy conservation. A self-consistent formalism has been suggested recently [34], but due to numerical expenses it has not yet been applied to quantitative calculations. In Section 5.1 we will have a differential look at the time sequencing of particle emission and see that most hadrons leave the fireball in the latest stages of the collisions, when large flow velocities have built up. Therefore the contribution of particles traveling back into the fireball is rather small, and we stick with the traditional formalism, Eq. (2.23).

At RHIC (but also at the SPS [118, 31]) there is clear evidence that chemical freeze-out happens at larger temperatures than thermal freeze-out [32], meaning that the relative particle abundances are set at a larger temperature than the flow properties, in particular the slopes of the spectra which are fixed at thermal freeze-out. Evidence is developing that the chemical freeze-out is happening close to the transition to hadronic matter, i.e. hadrons are born into chemical equilibrium [32] and stay there! Therefore we use the Cooper-Frye prescription to evaluate the relative particle abundances at hadronization, i.e. at $T_{\mathrm{crit}} =$ 164 MeV. In principle one could then keep those particle ratios fixed during the further evolution of the system by ascribing a space-time dependent chemical potential μ_h to each individual hadron species [124]. This however is not expected to lead to a largely different relation between the energy density, baryon density and pressure in the hadronic stage, and subsequently to no large influence of the system's evolution. In our approach, chemical equilibrium is implicitly assumed to hold all the way to the thermal decoupling temperature T_{dec}, and to reproduce the relative abundances of heavy hadrons correctly, we will have to rescale their

---

[5] The generalization of the derivation given in [104, 58] is shown at length in Appendix A.

spectra evaluated at freeze-out temperature $T_{\rm dec}$. Again, this does not largely influence the *flow* phenomena which are investigated in this study.

Particle emission in this scenario also includes the generation of heavier, short lived resonances, which decay into lighter hadrons that are superimposed on the thermal particle spectra resulting directly from the freeze-out hypersurface [117]. The contributions of all known resonances [52] and their kinematic decays are taken into account and added to the thermal spectra. We will remark on the importance of these resonance decay contributions in a later section.

Freeze-out can be modeled in more detail by evolving the hadronic rescattering stage not within a hydrodynamic picture, but rather by switching to a cascade calculation (RQMD or UrQMD), which treat the hadronic physics microscopically [125, 126, 20, 21, 116]. Unfortunately such a microscopic approach for the freeze-out description leads to a large increase in numerical costs. This makes quantitative comparisons to a broad variety of observables rather time intensive. On the other hand, there are also large payoffs. In addition to the proper modeling of the gradual transition from a hydrodynamic ensemble to free-streaming particles, chemical freeze-out happens naturally in the cascade afterburners As discussed earlier, chemical freeze-out could be implemented in the hydrodynamic equation of state by adding chemical potentials for the various particle species under investigation. It is important and assuring to note that the flow patterns of the hybrid models do not largely deviate from purely hydrodynamic flow patterns [126]. We mainly focus on momentum observables of the most abundant hadronic species produced in the collisions – pions, kaons and protons. Later we will focus on observables (e.g. elliptic flow, see Chapter 4) which are generated early in the collision. As the cause of the signal ceases at a rather early time in the collision, it is largely independent on the freeze-out condition and the applied freeze-out mechanism. There, we will also see in which parameter space the full hydrodynamic assumptions seem to hold, and it will be interesting to find out where the picture begins to break down and freeze-out in fact has to be modeled more realistically. In Chapter 5 we will discuss the geometry in coordinate space of the freeze-out in more detail. There, we will present experimental data, which pose serious difficulties to the rapid freeze-out from a decoupling hypersurface as well as to the gradual microscopic freeze-out out of a hadronic cascade.

2.4 Quantitative initialization

The entire evolution of the system from energy/entropy deposition in the pre-equilibrium stages through the hydrodynamic evolution to final particle freeze-out is now fully determined by the prescription discussed above. We finally have to fix the parameters of the initialization and freeze-out in order to reproduce physical observables, while keeping as much predictive power as possible. We therefore fix our parameters by tuning them in such a way that particle spectra from the *most central* collisions are well reproduced. To do so, we focus on the absolute pion yield per unit of rapidity, which gives a measure for the product of the initially stored entropy/energy density in the transverse plane times the equilibration time as the entropy per unit of rapidity is a conserved quantity in a hydrodynamic evolution with longitudinal boost invariance, Eq. (2.22). Then

$$\frac{dN}{dy} \propto \frac{dS}{dy} = \tau_{\mathrm{equ}} \int dx\, dy\, s(x,y;\tau_{\mathrm{equ}})\,, \tag{2.25}$$

helps us to fix the maximum of the entropy density distribution at equilibration $s_{\mathrm{equ}} = s(0,0;\tau_{\mathrm{equ}})$ – (in the equation above, the y on the left-hand side stands for rapidity, on the right hand side it is one of the 2 transverse coordinates over which is integrated, see the remarks on the notation in Section 1.4). As was discussed in the previous section, the relative particle abundances are fixed at the hadronization temperature $T = T_{\mathrm{crit}}$. We adjust the net baryon density at equilibration time $n_{\mathrm{equ}} = n(0,0;\tau_{\mathrm{equ}})$ to reproduce the experimental ratio of antiprotons to protons at hadronization, $\bar{p}/p = 0.65 \pm 0.08$ [7]. The slopes and shapes of the single particle spectra of identified pions and antiprotons help us to determine equilibration time and decoupling temperature. As a variation of one of our four parameters has influence on more than one observable at the time, one has to carefully tune the parameters to obtain the best fit to the data. Fig. 2.10 shows the transverse momentum spectra of positive pions and antiprotons from the PHENIX and the STAR collaborations, together with the spectra obtained from the hydrodynamic simulation initialized at equilibration time $\tau_{\mathrm{equ}} = 0.6$ fm/c with initial parameters $s_{\mathrm{equ}} = 95$ fm^{-3} and $n_{\mathrm{equ}} = 0.3$ fm^{-3}. Within our equation of state this corresponds to a maximum energy density $e_{\mathrm{equ}} = 24.6$ GeV/fm^3 and a central temperature of $T_{\mathrm{equ}} = 340$ MeV. With this initialization we arrive at a particle yield per participating nucleon pair $(dN_{\mathrm{ch}}/d\eta)/(0.5 \cdot N_{\mathrm{WN}}) = 3.1$ in central collisions.

Recent results from the first run of RHIC at full beam energies showed an increase in pion multiplicity at midrapidity of 15-20 % relative to RHIC 1 [17, 24]. When giving predictions for observables at full beam energy we therefore use a maximum initial entropy density of $s_{\mathrm{equ}} = 110$ fm^{-3}. In order to see what effects

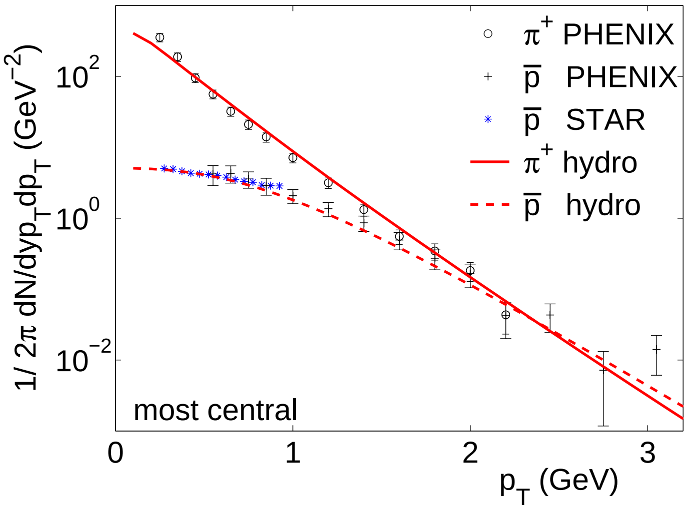

Figure 2.10: Transverse momentum spectra of pions and antiprotons from most central collisions (up to 5% of the total cross section) from PHENIX [127, 35] and STAR [10] in comparison with hydrodynamic results.

arise by changing the maximum entropy/energy density only, we omit changing the initial baryon density, freeze-out temperature and equilibration time, and leave those parameters the same as for RHIC 1 simulations. Calculations with this parameter set will be referred to as 'RHIC 2'.

Later we will also give predictions for systems expected to be created at LHC. At those much higher center of mass energies of $\sqrt{s_{\mathrm{NN}}} = 5.5$ TeV, we expect systems with higher initial temperature and therefore shorter formation and equilibration times of the particles [71], in fact such that $T_{\mathrm{equ}}\tau_{\mathrm{equ}} \sim$ const (which we omitted in the extrapolation from RHIC 1 to RHIC 2, as due to $s \sim T^3$ the effect is small for the modest change in s_{equ}). For the LHC, we assume an initial temperature of 1 TeV as suggested in [47]. At higher energy, less net baryon density is deposited in the transverse plane, an effect known as nuclear transparency. For the sake of simplicity, we leave n_{equ} constant at energies above RHIC 1. For the dynamics of the evolution this does not play a role as the equation of state in the plasma stage which rules the expansion at these energies is independent of n. We do not attempt to present predictions of particle ratios where n would be influential.

For calculations at SPS energies we fitted hydrodynamic spectra to experimental spectra of charged hadrons and net protons from central collisions [74, 75]. We found that $s_{\mathrm{equ}} = 43$ fm^{-3} and $n_{\mathrm{equ}} = 1.1$ fm^{-3} at $\tau_{\mathrm{equ}} = 0.8$ fm/c gives the best description to the SPS data, together with a freeze-out temperature of 120 MeV. Those results are displayed in Figure 2.11. The figure also shows the results from RHIC which we discussed previously. It is apparent at first glance that the particle spectra at the higher energies are flatter, which is a consequence of higher initial energy densities at RHIC and stronger transverse flow due to

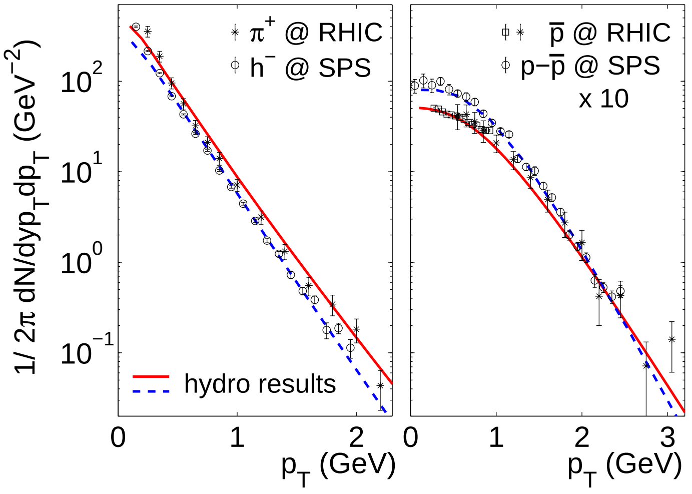

Figure 2.11: Energy dependence of particle spectra in central collisions. Left: π^+ at RHIC ($\sqrt{s_{\rm NN}} = 130$ GeV) [127, 35] and negatively charged hadrons at SPS ($\sqrt{s_{\rm NN}} = 17$ GeV) [13]. Right: antiproton spectra at RHIC [127, 35, 10] and net-protons at SPS [13]. Hydrodynamic spectra are displayed as solid (RHIC) and dashed (SPS) lines.

larger pressure gradients (the average transverse velocity at freeze-out, Section 3.4, increases by $\sim$ 15% from SPS to RHIC). To compare the energy density and energy content in the two systems, we evaluate the average energy density $\langle e\rangle(\tau{=}1~{\rm fm}/c) = \int_{e>e_{\rm dec}} dxdy\, e(x,y;\,\tau{=}1~{\rm fm}/c)/\int_{e>e_{\rm dec}} dxdy$ in the fireball at the fixed proper time $\tau = 1$ fm/c. This is often taken as a reference point also in the discussion of experimental data, as the initial energy density can be roughly estimated from the transverse energy per unit rapidity $dE_{\rm T}/dy$ in the final state. Bjorken estimated [27] for a boost invariant source of transverse radius R but without transverse expansion, that the initial energy density at some 'formation time' τ_0 is given by

$$\langle e\rangle = \frac{dE_{\rm T}}{dy}\frac{1}{\tau_0 \pi R^2}\,. \tag{2.26}$$

The initial conditions for our SPS initialization lead to $\langle e\rangle(\tau = 1{\rm fm}/c) = 3.6$ GeV/fm^3, whereas our calculations for RHIC energies give 5.4 GeV/fm^3, a 50 % gain in energy density. Using the Bjorken estimate, the PHENIX collaboration obtained from their measurements of the transverse energy an average energy density of 4.7 ± 0.2 at $\tau = 1{\rm fm}/c$ [4, 35]. The discrepancy originates from the transverse energy that is observed in the experiment and hydrodynamic calculations, which we will discuss in Section 3.5. For the moment, we note that the experimental derivation with the bottom-top estimate (from final state transverse energy back to initial energy density) is in rough consistency with the hydrodynamic approach, which takes the top to bottom approach (from thermalization to spectra). In any case, it appears that the experiments produce systems with energy densities that penetrate far into the critical region predicted by lattice QCD calculations (Chapter 1).

The resulting parameters for the 4 different energy domains are summarized in Table 2.1. In addition, we give parameters which allow reasonable fits to the RHIC 1 particle spectra when using the purely hadronic equation of state EOS H.

	τ_{equ} (fm/c)	s_{equ} (fm^{-3})	n_{equ} (fm^{-3})	e_{equ} (GeV/fm^3)	T_{equ} (MeV)	T_{dec} (MeV)
SPS	0.8	43.0	1.1	9.0	257	120
RHIC 1	0.6	95.0	0.3	24.6	340	130
RHIC 2	0.6	110	0.3	29.8	360	130
LHC	0.21	500	0.3	222	1000	130
RHIC H	0.6	95.0	0.3	22.8	272	140

Table 2.1: Maximum values of the initial entropy- and baryon density (s_{equ} and n_{equ}) at equilibration time τ_{equ}, for the simulations at different beam energies from SPS to LHC together with the applied freeze-out temperature T_{dec}. The initial energy density and temperature are related to the entropy and baryon density via the equation of state. The last line gives parameters suitable for a description of the RHIC 1 particle spectra with a purely hadronic equation of state underlying the hydrodynamic evolution.

2.5 TIME EVOLUTION OF FLOW CHARACTERISTICS

The equations of motion, together with the equation of state of the flowing matter fully determine the further time evolution of the initial thermodynamic fields. The continuously present pressure gradients lead to a continuous generation of collective flow in the transverse plane. As we have already discussed, this is of particular interest, as the initial stage of the collision is essentially free of transverse motion. Thus the observed transverse flow is a pure product of the expansion dynamics. In contrast, for observables along the beam direction it is difficult to disentangle collective effects which are a result of the expansion from the longitudinal motion imprinted by the initial conditions.

In Section 2.1, we discussed the azimuthal asymmetry in the transverse plane arising from non-central collisions. These initial configurations offer stronger pressure gradients along their short axis (in direction of the x-axis) than along their long axis (in direction of y). The driving forces along the short direction therefore are stronger, and transport of matter is more efficient along the short than along the long axis. Eventually, the developing asymmetry in the generated flow field leads to a reduction of the asymmetry of the density fields, until they finally disappear and no further anisotropic flow is generated [120, 121].

To render this discussion more quantitative and to investigate the time-scales of these processes, we study the time-evolution of the spatial anisotropy ϵ_x, as defined in Eq. (2.7) [75]. Anisotropies in the flow pattern manifest themselves as a momentum anisotropy, expressed through the energy-momentum tensor as

$$\epsilon_p = \frac{\langle\langle T^{xx} - T^{yy} \rangle\rangle}{\langle\langle T^{xx} + T^{yy} \rangle\rangle}\,, \tag{2.27}$$

where $\langle\langle \ldots \rangle\rangle$ denotes the average over the full transverse plane at fixed proper time τ. Furthermore we investigate the average transverse flow velocity in the system

$$\langle\langle v_\perp \rangle\rangle = \frac{\langle\langle \gamma \sqrt{v_x^2 + v_y^2} \rangle\rangle}{\langle\langle \gamma \rangle\rangle}\,. \tag{2.28}$$

Figure 2.12 displays the time evolution of these quantities for collisions at SPS, RHIC and LHC energies, for a fixed impact parameter of $b = 7$ fm. Additionally the evolution for a system with the ideal gas equation is given. This represents the limiting case of infinite collision energy, as in this case the system's evolution is entirely determined by the hard quark-gluon plasma phase where $\partial p/\partial e = 1/3$. The evolution of the latter system is essentially insensitive on the initialization energy density and the equilibration time. The top panel of Fig. 2.12 shows how the spatial anisotropy develops from the initial almond elongated in y-direction ($\epsilon_x > 0$), to rounder shapes (smaller ϵ_x).[6] When ϵ_x reaches zero, the flow has built up so strongly that the preferred motion in x direction is continued and the fireball becomes oval shaped again, this time with a preference in x direction (ϵ_x turns *negative*). It is clear that this process occurs the faster the harder the equation of state is, which means here the higher the energy density in the system is.

Parallel to the evolution of *spatial* anisotropies, the second panel shows the evolution of the *momentum* anisotropy. The larger the spatial eccentricity is, the larger are the driving forces to build up momentum asymmetries. In the plasma stage with the hard QGP equation of state, the largest forces are at work and reduce the spatial asymmetry the fastest. Note that for RHIC energies, almost all momentum anisotropy is built up during the first 3 fm/c. This is a combined result of the reduction of spatial anisotropy, and the disappearance of transverse forces (vanishing pressure gradients) in the mixed phase. The triangles, squares and circles show where the center of the system enters the mixed and the hadronic phase and finally where the entire system has cooled below the freeze-out

---

[6] At the same impact parameter b, the initial spatial deformation $\epsilon_x(\tau_{\mathrm{equ}})$ is smaller at the SPS than at the higher energies due to the more anisotropic binary collision contribution at higher energies (Fig. 2.6) which is absent at the SPS.

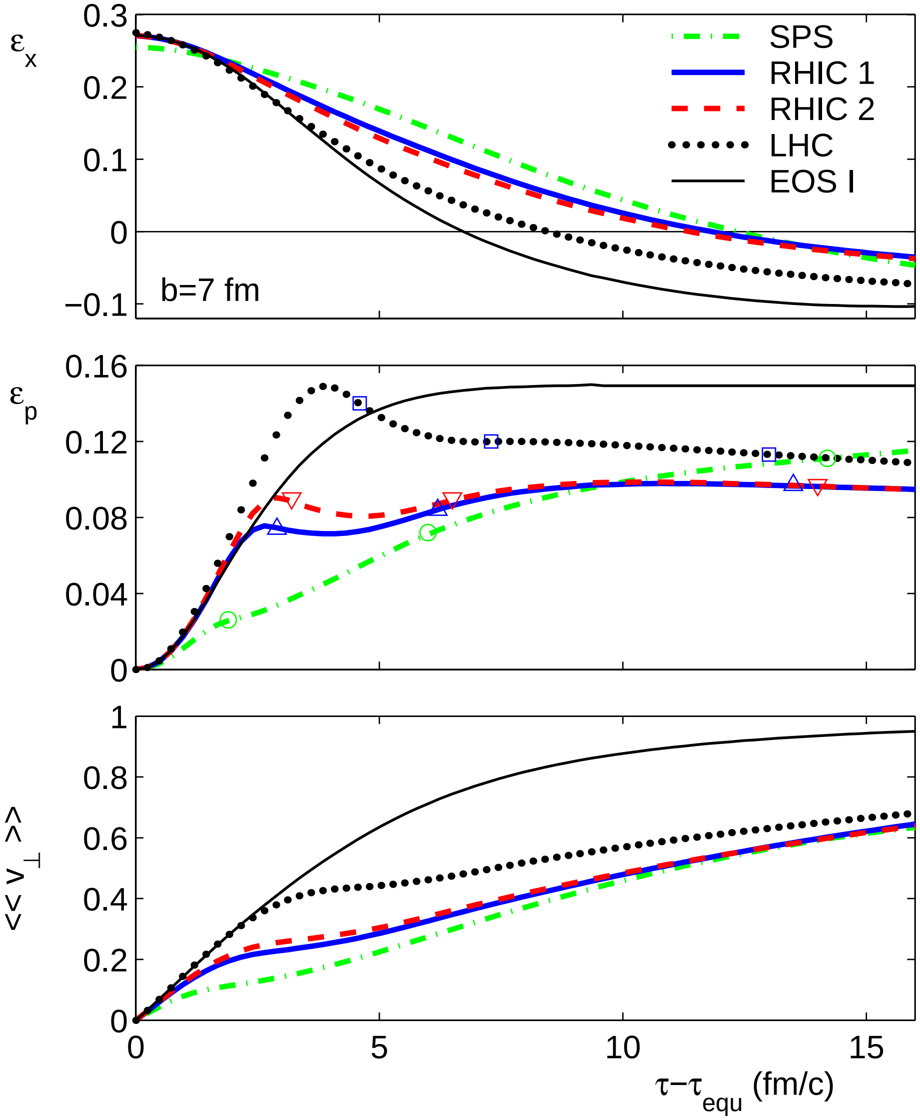

Figure 2.12: Time evolution of spatial anisotropy (top), momentum anisotropy (middle), and radial flow (bottom), for systems with entropy densities leading to particle multiplicities observed at the SPS, in RHIC year 1, RHIC year 2, predictions for the LHC and the ideal gas limit. The calculations were done for Au+Au (Pb+Pb) collisions at impact parameter $b = 7$ fm.

temperature. Even though microscopic calculations fall short in the quantitative predictions for elliptic flow, it is important to note that the timescale of the generation of asymmetries is very much the same in parton cascade calculations [137]. Another interesting effect is that at LHC energies anisotropy develops *faster* than in the extreme case given by EOS I. This is due to the mixed phase enclosing the QGP core in the realistic collision, which inhibits the development of flow more efficiently in y direction than in x direction. Therefore, for some time, the ideal gas case can give smaller flow anisotropies. The flow anisotropies can show a maximum as a function of time, even though the spatial anisotropy is still positive. This results from the inert mixed phase, where the flow pattern is 'frozen' but the system continues its expansion in a self-similar fashion [26]. This in turn leads to an effective reduction of the *anisotropies* in the system.

From the lowest figure one sees that radial flow does not show any saturation effects and keeps increasing monotonically with time, to be bounded only by the speed of light. There are pressure gradients in the system throughout the time evolution, therefore radial flow keeps growing, summing up information over the full history of the time evolution. This starkly distinguishes flow anisotropies from radial flow, as anisotropic flow gathers up information mainly from the earliest and hottest stages of the collision.

2.6 THE INFLUENCE OF THE PHASE TRANSITION

To understand the expansion of the fireball in even more detail we consider contour plots of the energy density in the transverse plane. Fig. 2.13 shows four snapshots of the transverse plane at 2, 4, 6 and 8 fm/c after thermalization, for the RHIC 1 initialization with impact parameter $b = 7$ fm. In addition to the contour plots marking 5, 15, ..., 95 % of the maximum energy density, the plots contain contours for the freeze-out energy density $e_{\rm dec} = 0.08$ GeV/fm^3 (dash-dotted), the critical energy density $e_{\rm crit} = 0.45$ GeV/fm^3 for the transition from hadron gas to mixed phase (dashed) and the energy density of the pure quark-gluon plasma $e_{\rm QGP} = 1.6$ GeV/fm^3 (solid), where applicable.

After 2 fm/c the system consists of three distinct parts. In the interior we still have the stiff quark-gluon plasma stage, surrounded by an inert mixed phase, where pressure gradients vanish and therefore the matter does not experience accelerating forces. This in turn is confined by a shell of hadronic matter. This configuration leads to interesting solutions of the hydrodynamic equations [123] which we have already discussed in the previous section. The strong pressure gradients in the interior lead to large forces on the fluid cells and large matter

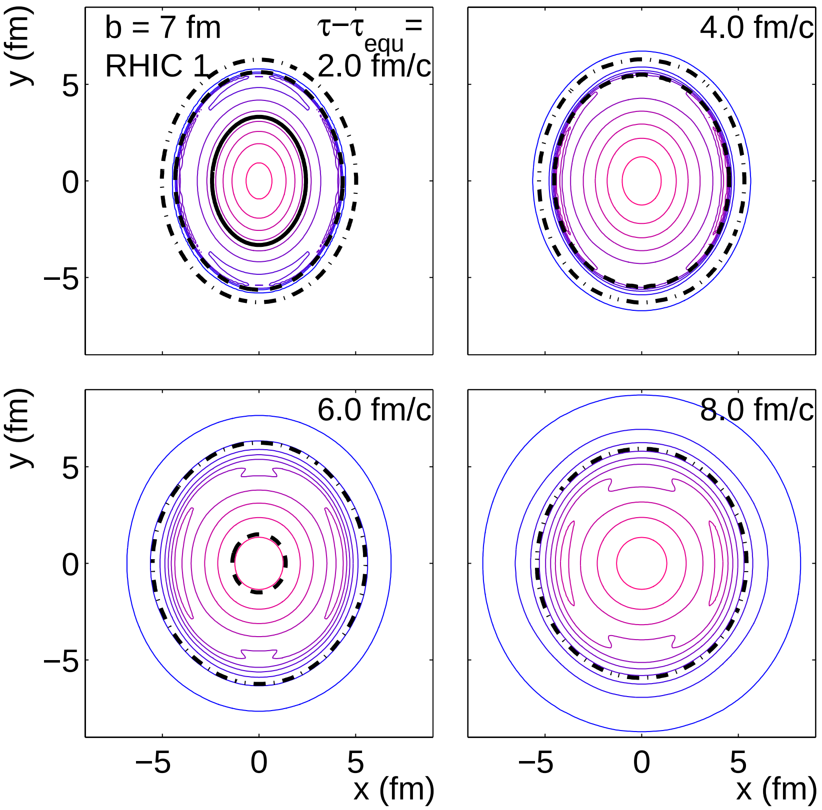

Figure 2.13: Contour plots of the energy density in the transverse plane for RHIC 1 collisions with $b = 7$ fm. Shown are the contours of 5, 15, ...,95 % the maximum energy density at the corresponding time-step, which are subsequently 2.56, 0.99, 0.48 and 0.25 GeV/fm^3. The thick lines indicate the boundary between plasma, mixed and hadronic phase where applicable.

transport, which is stronger in x- than in y-direction due to the initial geometry. However when this motion hits the soft mixed phase, it cannot be absorbed quickly enough into the mixed phase and streams up- and downwards instead of entering the ring of mixed phase [75]. This leads to the horn-shaped contours already seen in the first snapshot. When the system dilutes further (both longitudinally and transversely) the horn-shaped contours enter the hadronic stage and pick up more transverse Hubble like radial velocity. This can eventually lead to a breaking of the horn-shaped contours and result in two separate islands of higher energy densities (plot 3 of the series). Teaney and Shuryak [123] argued that this eventually can turn into a 'nut-shell' like freeze-out hypersurface, however as the figures suggest it is a very weak effect.

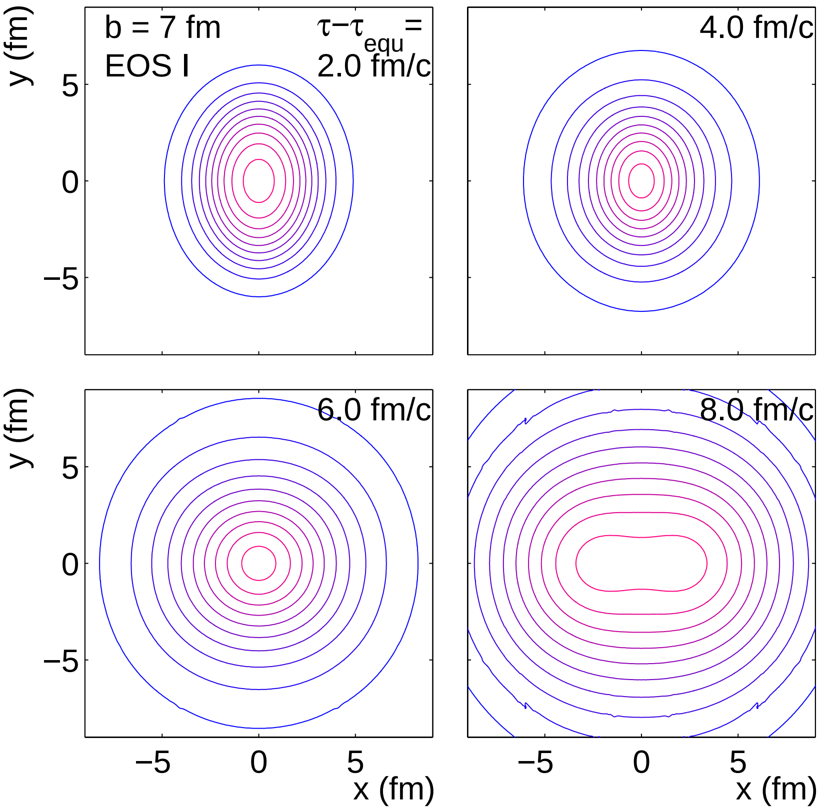

Figure 2.14: Contour plots of the energy density in the transverse plane for a system without a phase transition (EOS I). Shown are the contours of 5, 15, ...,95 % the maximum energy density at the corresponding time-step, which are subsequently 20.1, 5.60, 1.28 and 0.26 GeV/fm^3.

Also note how the distinctive initial elongation along the y-axis gets washed out by time. As we have discussed before, the system becomes rounder as time goes by and eventually can even turn over to negative values of ϵ_x.

The formation of these distinctive flow patterns is entirely due to the phase transition in the equation of state. In the case of an ideal gas equation of state, the contours of constant density evolve much more smoothly, as shown in Fig. 2.14. In this case the switch from out-of-plane to in-plane elongation is even clearer to see. Due to the hard equation of state the dynamics develops on shorter timescales than the dynamics of a system containing a soft part in the equation of state. Furthermore we have seen how a mixed phase inhibits the generation of flow and flow anisotropies. The confining property of a mixed phase shell around a QGP core leads to longer system lifetimes and smaller anisotropies in the resulting observables. Here we have only qualitatively assessed the influence of the phase transition. We will return to investigate the issue on a more quantitative level in the next chapters.

We conclude that anisotropies in particle flow, which will finally manifest themselves in anisotropic particle emission, have the unique property of being a hadronic probe which carries information on the earliest time of the collisions where the partons were deconfined. Elliptic flow thus is an early fireball signature which can be measured at the $^0/_{00}$ level even with a general purpose detector. However it only gives large signals in strongly deformed systems; unfortunately the larger the impact parameter, the more likely is the breakdown of the assumption of local equilibration.

This problem could be circumvented by colliding *deformed* nuclei, e.g. ^{238}U, side-on-side where a strong spatial deformation exists even in central collisions [85, 112, 75]. The deformed oval in such a process is much larger than in non-central collision of spherical nuclei, as the long and short axis of the nuclei are $R_l = 8$ fm and $R_s = 6.2$ fm respectively [29]. In comparison, a collision of two Au nuclei with impact parameter 7 fm has (Gaussian) radii of about 4.5 and 3.5 in the long and short direction. Furthermore the central U collisions have larger initial energy densities than the non-central Au collisions where the overlap functions are much smaller. Therefore we do not only have a much larger system, but also one that probes into higher energy densities and has larger initial particle number densities. This is all in favor of a better applicability of hydrodynamic laws. Furthermore, the system lives longer and the laws we want to probe are at work for a longer time. Given the rich flow physics underlying such U+U reactions they should not go mentioned and an experimental realization should be further discussed. We will comment on the aspects of triggering on collisions in side-on-side configurations in Section 4.1.2.

3

Global transverse observables

All the parameters of the calculation are now fixed by fitting to the single particle spectra of central collisions as presented in the previous chapter. Only the parameter determining the relative influence of the soft and hard contributions in the initial state makes use of the centrality dependence of the observed total multiplicity. The centrality dependence of all other observables from non-central collisions however are parameter free predictions of the theory.

In this chapter we discuss global hadronic observables in the transverse plane, i.e. observables related to the azimuthally integrated transverse momentum spectrum

$$\frac{dN}{p_{\mathrm{T}} dp_{\mathrm{T}}\, dy}\,(p_{\mathrm{T}},\, y;\, b) = \int_0^{2\pi} d\varphi_p\, \frac{dN}{p_{\mathrm{T}} dp_{\mathrm{T}}\, d\varphi_p\, dy}\,(p_{\mathrm{T}},\, y,\, \varphi_p;\, b)\,. \tag{3.1}$$

All sensitivity to the emission angle φ_p relative to the reaction plane is here integrated out. The remaining dependencies on impact parameter stem only from the decreasing system size and the reduced energy that is stored in the system when observing more peripheral collisions. In particular we will study the transverse momentum spectra of identified particles from collisions with various centralities, as well as the particle multiplicities, the mean transverse momentum and the average radial velocity as functions of centrality. Observables which exploit the azimuthal anisotropy in the transverse plane are the subject of the following chapter. Throughout this work we investigate results taken at midrapidity, i.e. at $y = 0$.

Experimentally the recorded events can be classified with respect to their collision centralities. The different collaborations use different techniques for this centrality binning, but finally a consensus seems to be emerging.[1] In most of the

---

[1] A special workshop devoted exclusively to this very issue was held at Brookhaven National Laboratory on July 19, 2001: 'RHIC Topical Workshop: Estimating N_{part} and N_{coll}'.

data to be analyzed in the following, the STAR collaboration classified the centrality of the collisions solely through cuts in the total multiplicity distribution of the total set of data used in the corresponding analysis [2, 115, 9, 10], as the most central events should lead to the largest entropy deposition in the reaction-zone, and therefore they should result in the largest particle yield. In this sense, the 6% of the events giving the largest particle yield are then attributed to result from the 6% most central collisions [2], etc. The PHENIX collaboration on the other hand uses a correlation between the observed signal in a zero-degree calorimeter (measuring the energy going down the beam direction, which is larger in peripheral collisions) and a signal from the beam-beam counter (measuring fast moving particles in forward/backward direction) which is the larger the more central a collision is [3, 127, 35]. Through these counteracting observables fluctuations in the individual collisions can be respected, an effect which the old STAR classification cannot capture. In a recent publication, STAR also uses such correlation effects for the determination of the most central collisions [8].

To get an estimate for the number of nucleons that participated on average in a collision within one of the different centrality classes, a Glauber-model calculation similar to the one presented in Section 2.1 needs to be employed. Unfortunately this introduces parameter dependencies (parametrization of density, nucleon-nucleon cross-section, optical model approximation, ...) which can only be avoided by adopting a generally accepted common set of parameters (which is so far not yet the case). The experimental observables can then be expressed as function of the average number of participants (wounded nucleons) in the collision. The PHENIX results which we discuss in this chapter are divided into 5 centrality bins with $\sigma =$ 0-5, 5-15, 15-30, 30-60 and 60-92 % of the total nucleus nucleus cross-section $\sigma_{\rm tot} = 7.2$ mb [127, 35]. The average number of wounded nucleons PHENIX estimates for these centralities is 347 ± 10, 271 ± 9, 178 ± 7, 76 ± 7 and 14 ± 3.5 respectively [35, 3] (the given error reflects the systematic uncertainties).

3.1 Transverse momentum spectra

For a first qualitative comparison we study the centrality dependence of identified particle spectra as presented by the PHENIX collaboration [127, 35]. Fig. 3.1 shows the normalized particle spectra of identified negative pions; as one goes from central to peripheral collisions, each following spectrum is scaled down by a factor of 1/10 for clearer visibility. Pion spectra from the most central bin were used to fix the parameters (Fig. 2.10) but we see that excellent agreement persists also for non-central collisions. Even in the most peripheral bin larger deviations

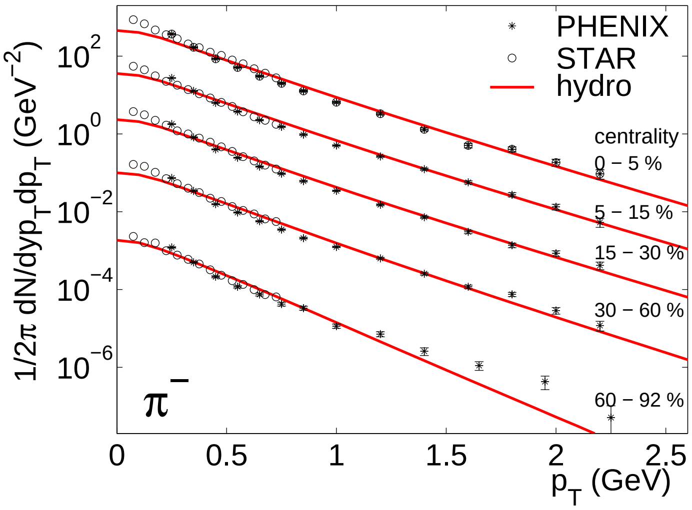

Figure 3.1: Transverse momentum spectra of negative pions from the hydrodynamic simulation compared to data from PHENIX [127, 35] in 5 different centrality regions and STAR [36] in slightly different bins (see text).

only start to occur for p_T higher than 1.5 GeV (later we will investigate these deviations and their origins in more detail, Sec. 4.1.4). In the figure, we also included the most recent pion spectra from the STAR collaboration [36], which is sensitive in a window of lower transverse momentum than the PHENIX detector. The STAR data shown in the plot correspond to the centrality bins with 0-5, 10-20, 20-30, 40-50 and 70-80% of the total cross-section [36].

The transverse momentum spectra of antiprotons are displayed in Fig. 3.2. Again we have included the latest results by STAR [10]. Even though these data are taken again in slightly different centrality bins with a different binning strategy (the figure includes results from the 0-6, 6-11, 18-26 and 45-58 % centrality bins from STAR [10]) the agreement of the 2 experiments in the four more central

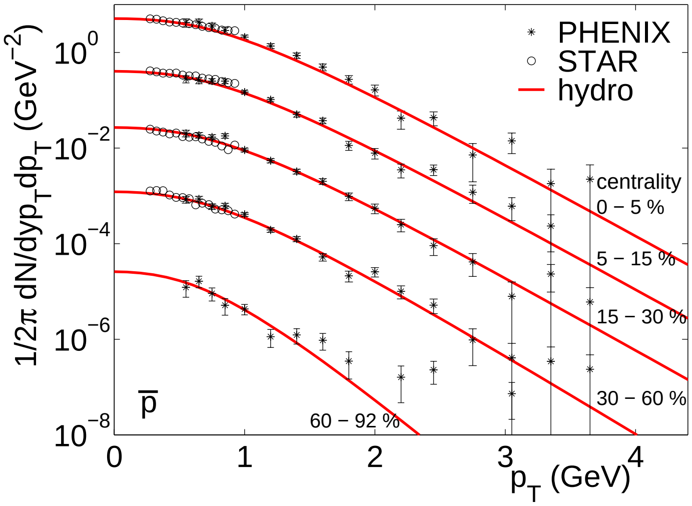

Figure 3.2: Transverse momentum spectra of antiprotons from the hydrodynamic simulation compared to data from PHENIX [127, 35] and STAR [10] (see text) in 5 different centrality regions [127, 35].

bins is excellent. After scaling the hydrodynamic antiproton spectra in order to take the higher chemical freeze-out temperature into account (see Section 2.4), the spectral shapes of the hydrodynamic results are in excellent agreement with the experimental data over almost the full range of centralities and momenta up to 3 GeV. Significant deviations occur only in the most peripheral bin with $\sigma > 60\% \, \sigma_{\mathrm{tot}}$.

Finally, we can compare hydrodynamic spectra for charged kaons with experimental results. Fig. 3.3 shows the transverse momentum spectra of positive kaons [35]. Again, we find excellent agreement with the hydrodynamic predictions. It must be stressed that the kaons were not included in any procedure for fitting the initial conditions. So here already the results for the most central bin were a prediction, which is fully confirmed by experiment.

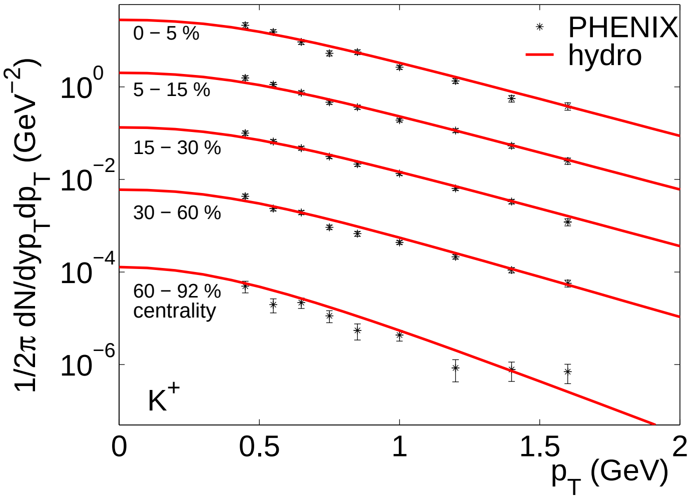

Figure 3.3: Transverse momentum spectra of positive kaons from the hydrodynamic simulation compared to data from PHENIX in 5 different centrality regions [35].

Preliminary results for the single particle spectra of positive pions, negative kaons and protons have also been measured [35]. The resulting agreement is equivalent to the results presented here and is therefore not displayed in separate figures. The agreement between the hydrodynamic spectra and the experimental data is investigated on an even more quantitative level in the following sections when we regard the multiplicities, transverse momenta, etc. in the different centrality bins.

3.2 PARTICLE MULTIPLICITY

As discussed earlier, the final particle multiplicity is strongly correlated with the number of wounded nucleons of the collisions. Here we check the centrality dependence of the number of emitted particles per unit rapidity, which is readily obtained from the double differential spectra $dN/p_T dp_T dy$ by integrating over the transverse momentum:

$$\frac{dN}{dy} = \int_{\min}^{\max} dp_T p_T \frac{dN}{p_T dp_T dy} \,. \tag{3.2}$$

Having multiplicities of identified particles available we can avoid the coordinate transformation to pseudo-rapidity (which had been necessary at an earlier stage of the data analysis [68, 77]) and can carefully employ the same geometric and centrality cuts on our simulations that have been employed in the experimental data. In particular, this frees us from artificial extrapolations outside of the experimentally accessible p_T-window, which can introduce large systematic uncertainties [35, 10]. Fig. 3.4 shows the fiducial multiplicities measured in the different centrality bins normalized to the number of wounded nucleon pairs. The pions include all pions with momenta $0.2 \leq p_T \leq 2.3$ GeV, for kaons the acceptance is $0.4 \leq p_T \leq 1.7$ GeV and the antiprotons reach from $0.5 \leq p_T \leq 3.8$ GeV. The plot includes hydrodynamic results under different assumptions on the binary collision contribution in the initialization. The thick lines correspond to a 25% contribution from binary collisions to the initial entropy density (see Section 2.4), the thin dashed lines assume a contribution of 15% and the dashed dotted

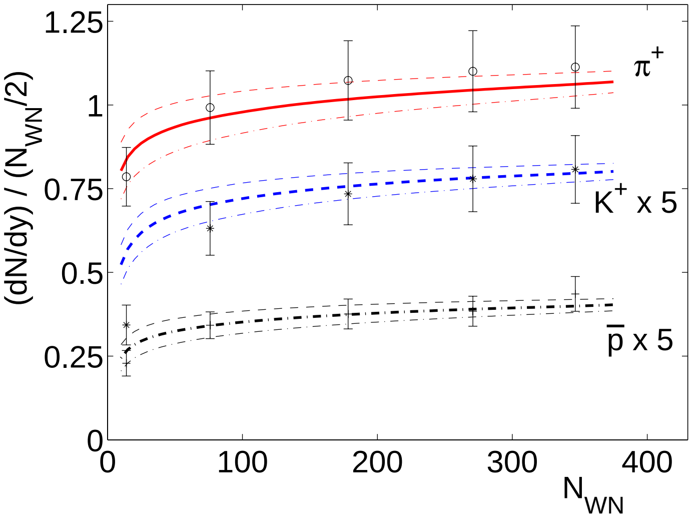

Figure 3.4: Particle yield of individual particle species per participating nucleon pair in the corresponding p_T-windows accessible by the PHENIX detector [35] (see text) and hydrodynamic calculations with identical cuts as functions of the number of participating nucleons. Different contributions of binary collision processes are indicated by the thin lines (see text).

lines a 35% contribution. Without a hard scattering contribution results in a direct proportionality of particle production per unit rapidity to the number of wounded nucleons and would thus lead to a constant $(dN/dy)\,/\,(N_{\rm WN}/2)$, which was seen at SPS energies [88]. The RHIC 1 data indicate that there is a significant contribution from hard processes, and first results at full RHIC energy continue in this trend [24, 18].

3.3 MEAN TRANSVERSE MOMENTUM

The dependence of the spectral slopes, or the mean transverse momentum of the particles, on their rest mass clearly exposes the collective expansion flow of the fireball matter. If all particles in the fluid share a common expansion velocity, the heaviest particles will carry away the largest moment (non-relativistically $p_{\rm flow} = m\, v_{\rm flow}$); using this, the average transverse flow velocity can be traced down [84, 109]. As the system size and energy content in the system decreases going from central to peripheral collisions, we expect smaller mean transverse momenta. For quantitative comparisons with the experiment we average the transverse momenta only within the experimental accessible $p_{\rm T}$ range, i.e.

$$\langle p_{\rm T}\rangle_{\rm trunc} = \frac{\int_{\rm min}^{\rm max} dp_{\rm T}\; p_{\rm T}^2\; (dN/p_{\rm T}dp_{\rm T}dy)}{\int_{\rm min}^{\rm max} dp_{\rm T}\; p_{\rm T}\; (dN/p_{\rm T}dp_{\rm T}dy)} \tag{3.3}$$

where the integration limits are the same as the ones described in the previous subsection.

Fig. 3.5 shows that the centrality dependence of the mean transverse momentum is somewhat stronger in the hydrodynamic model than in the real data. This is a reflection of the experimental particle spectra being *flatter* in the most peripheral collisions than the hydrodynamic spectra. This was already found to be true at SPS energies [76]. Most likely it originates from hard scattering effects in the most peripheral collisions which dominate already the low-$p_{\rm T}$ region of the produced particles. Recently it was argued [90, 105] that the particle spectra could be intrinsically broadened by a saturation of the gluon density in the transverse plane, building up a ‘color glass condensate’. At the moment however it seems that such a scenario is not able to account for the large azimuthal sensitivity of the transverse observables which we study in the next chapter.

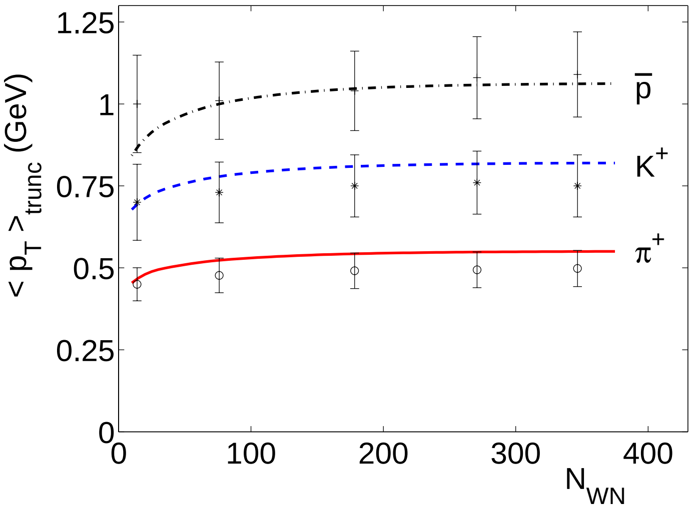

Figure 3.5: Mean transverse momentum within the p_{T}-windows accessible by the PHENIX detector [35] compared to hydrodynamic calculations with the same cuts as function of participating nucleons (see text for details).

3.4 Mean transverse flow velocity

From the experimental point of view, it is common practice (see e.g. [23]) to extract the freeze-out temperature T_{dec} and the average flow velocity by fitting the transverse mass spectra of various particle species to a hydrodynamically motivated model parametrization [84, 109], given as

$$\frac{dN}{p_{\mathrm{T}} dp_{\mathrm{T}}} \propto \int_0^R r dr\, m_{\mathrm{T}}\, \mathrm{I}_0 \left(\frac{p_{\mathrm{T}} \sinh \rho(r)}{T_{\mathrm{dec}}} \right) \mathrm{K}_1 \left(\frac{m_{\mathrm{T}} \cosh \rho(r)}{T_{\mathrm{dec}}} \right) . \tag{3.4}$$

Here $\rho(r) = \mathrm{Artanh}\, v_\perp(r)$, and one usually assumes a linearly increasing radial flow profile $v_\perp(r) = v_{\max}\, r/R$. This fitting routine was applied [35] individually for the different bins of the PHENIX data, but simultaneously for charged pions, kaons, protons and antiprotons. With increasing impact parameters (decreasing system size), the decoupling temperature was found to increase, from 121 ± 4 in the most central bin to $161 \pm (19, 12)$. This could be expected, as the system size is getting smaller and the mean free path of the constituents becomes of the order of the system size already at higher temperatures. For our hydrodynamic calculations we did not employ a centrality dependent freeze-out temperature, in order to avoid a proliferation of model parameters. We will come back to indications for a centrality dependence of the decoupling temperature in Section 4.1.1.

The average transverse velocity from the fit [35] to the particle spectra is displayed in Fig. 3.6, together with the mean transverse flow velocity on the freeze-out hypersurface of our full hydrodynamic calculation. It has to be stressed that the mean transverse momentum of the PHENIX data is a *fit parameter* to

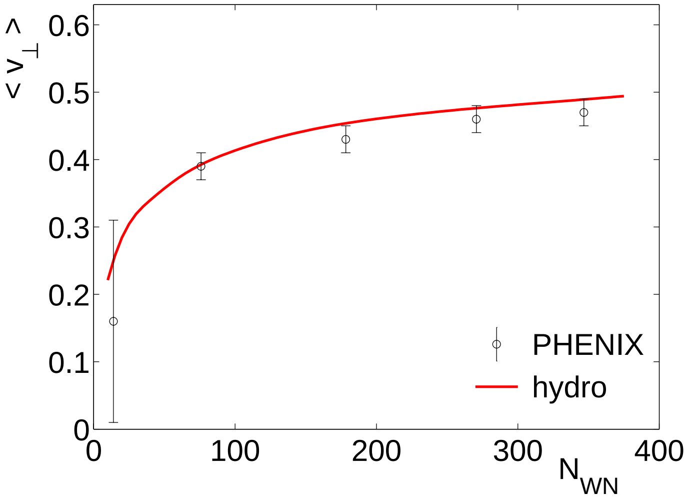

Figure 3.6: Mean transverse flow velocity obtained from fitting the hydrodynamical parametrization Eq. (3.4) to the PHENIX particle spectra of Section 3.1 [35]. The solid line is the mean transverse flow velocity on the freeze-out hypersurface in the full solution of the hydrodynamic equations.

describe the particle spectra under very simplistic assumptions (in particular a linear flow profile and homogeneous mass distribution of the emitting source, no geometrical aspects). The full hydrodynamic calculations are *pure predictions* for non-central collisions, with parameters adjusted to the most central collisions. That there is such good agreement between the model parametrization and the full calculation is remarkable.

3.5 Transverse Energy

Initially, energy is stored in the random thermal motion of the constituents of the system. Pressure gradients will then lead to a collective expansion, converting thermal energy into collective flow energy, thereby reducing the local temperature in the system. If there were no pressure gradients in the transverse plane, the system would only expand longitudinally (i.e. due to a Bjorken flow velocity field, Sec. 2.2.3) and only lead to a conversion of thermal energy into *longitudinal* work. Therefore the average *transverse* energy per particle decreases in time while the system expands longitudinally. Furthermore, with Bjorken flow, the entropy per unit rapidity dS/dy is conserved (Section 2.2.3). But the entropy per unit rapidity is proportional to the number of (charged) particles per unit rapidity in the final state dN_{ch}/dy, and therefore we expect that for such a system the average energy per particle decreases with the lifetime of the system. The lifetime of the system depends strongly on the impact parameter of the system and the amount of energy deposited in the transverse plane while the collision occurs (Section 2.1). As we have seen before we have to employ a dependence of the initial entropy density which increases more than linearly with the number of wounded nucleons in the collision. From this point of view, one expects that for a boost invariant source without transverse flow the transverse energy per particle is largest when the system is small (i.e. large impact parameter, small number of wounded nucleons) and decreases in more central collisions (large number of wounded nucleons), due to the extended lifetime.

The transverse pressure gradients from the wounded nucleon or binary collision profiles lead to transverse forces and transverse work being performed on the medium, converting thermal energy partially into transverse collective flow energy. This increases the dilution and cooling rate compared to a purely longitudinal expansion, thereby reducing the amount of transverse energy lost by longitudinal work done until freeze-out. One sees that the final transverse energy is an observable that intrinsically couples information on the interplay of longitudinal and transverse expansion. Fig. 3.7 shows corresponding results for

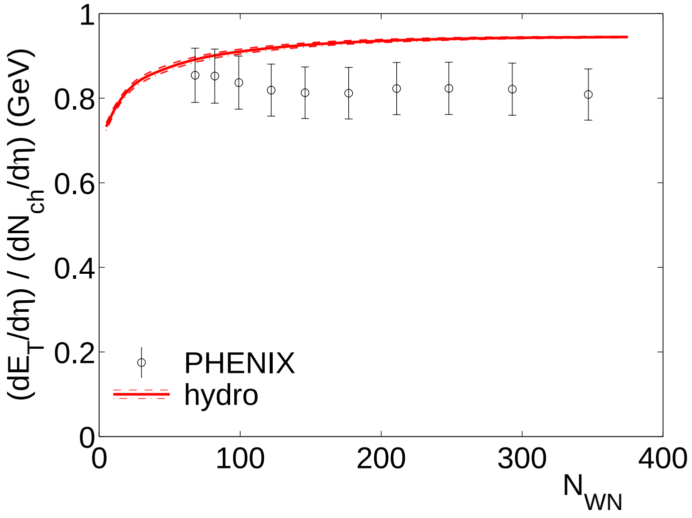

Figure 3.7: Transverse energy per produced charged hadron in the final state from hydrodynamics (with different contributions of binary collisions in the initial stage, see Fig. 3.4) and the PHENIX experiment [4].

the hydrodynamic model with longitudinal boost invariance (as in Fig. 3.4 we include results from different contributions of binary collision effects and find that E_T/N_{ch} is rather insensitive to the fraction of binary collisions). Here we have adapted our calculation according to the prescriptions given by PHENIX in [4], that the transverse energy is the sum of the kinetic energy of the observed nucleons and the total energy of all other particles – still there is systematic discrepancy of about 10 % that goes unaccounted for. Hadronic calorimetry is a very difficult topic, especially at the start-up of a new experiment. Therefore we refer from investigating and interpreting this discrepancy in further detail until confirmation by other experiments is available.

Important in the qualitative behavior is that the PHENIX data show an onset of an *increase* of transverse energy per charged particle with larger impact parameters, whereas the transverse energy from hydrodynamics decreases. The statistical significance of this increase is not clear, but its confirmation would have exciting implications. The easiest way to interpret it might be a breakdown of the longitudinal pressure in very peripheral collisions, due to incomplete thermalization. This would reduce the longitudinal work done by the medium, leaving more of the original transverse energy per particle in the transverse plane. Reduced longitudinal pressure was found to appear in transport models of the collision [45], and we will find other indications for such an effect in Section 5.4.

At the lower SPS energies ($\sqrt{s_{\mathrm{NN}}} = 17$ GeV) such an increase is not observed [11], and thus it is still open to debate if there is a new behavior to be found in the most peripheral collisions at high energies. Comparing further to results from the SPS one finds that the ratio $\frac{dE_{\mathrm{T}}}{d\eta} / \frac{dN_{\mathrm{ch}}}{d\eta}$ is not measurably changed by the higher initial energy densities. It appears that more longitudinal work at higher energies largely compensates for the larger thermal energy in the initial state.

4

ANISOTROPIC PARTICLE EMISSION

As was argued in Section 2.5, the anisotropy in the initial coordinate space configuration of a non-central collision rapidly transforms into an anisotropy in momentum space of the expanding fluid. Thereby the coordinate space anisotropy decreases and thus the initial cause for the generation of momentum anisotropy is reduced until it finally completely disappears. The imprint on the momentum anisotropy is carried over to the final state, but it has its origin from the earliest stage of the collision. This is of course the most interesting time of the collision as it probes the equation of state under the most extreme conditions of density and temperature as well as the concepts of thermal equilibration in the earliest stage of the expansion.

Larger flow fields along the x-axis than along the y-axis in the transverse plane will lead to flatter particle spectra (smaller slopes in a logarithmic plot of $\frac{dN}{dyp_{\mathrm{T}}dp_{\mathrm{T}}d\varphi_p}$) when observed from along the x-axis ($\varphi_p = 0$) than when observed from along the y-axis ($\varphi_p = \pi/2$). This is simply because a shining source of temperature T approaching with velocity v an observer who is at rest will appear *'blue-shifted'* (Eq. 3.4): Particles with $m \ll p_{\mathrm{T}}$ will have spectral slopes as emitted from a source at rest with apparent temperature

$$T_{\text{blue}} = T\sqrt{\frac{1+v}{1-v}}\,, \tag{4.1}$$

where v is the average transverse expansion velocity in the observed direction. Flatter particle spectra in direction of the impact parameter ($\varphi_p = 0$) than orthogonal to it ($\varphi_p = \pi/2$) also means that the total number of particles emitted into the reaction plane is larger than perpendicular to it ("out of plane"). To quantify this azimuthal sensitivity of particle emission, one performs a Fourier expansion of the transverse momentum spectra with respect to the azimuthal angle φ_p to the reaction plane (at $y = 0$):

$$\frac{dN}{p_{\rm T} dp_{\rm T} d\varphi_p dy}(b) = \frac{dN}{2\pi p_{\rm T} dp_{\rm T} dy}(b) \left(1 + 2\, v_2(p_{\rm T};\, b) \cos(2\varphi_p) + ...\right) . \qquad (4.2)$$

The way the coordinate system is defined (Fig. 2.1), the system's evolution is mirror symmetric with respect to the reaction plane, and therefore the observables under investigation respect the symmetry $f(\varphi) = f(-\varphi)$; this is true both in coordinate and momentum space, as the symmetries in coordinate space translate to symmetric gradients and driving forces for the momentum space evolution. Therefore the Fourier expansion, Eq. (4.2), does not contain any sinus terms. In addition, in the transverse plane we have by construction of our coordinate system reflection symmetry under $x \leftrightarrow -x$ leading (together with $y \leftrightarrow -y$) to the symmetry $f(\varphi) = f(\varphi+\pi)$ resulting in even expansion coefficients only. In reality we have spectator matter, leaving the transverse plane at $z = 0$ with a velocity that is approximately the same as the velocity of the nuclei before collision. This breaks the symmetry with respect to the transverse plane at $z = 0$ and leads to a non-zero coefficient v_1, i.e. a coefficient in the expansion Eq. (4.2), which describes an angular modulation with $\cos(\varphi_p)$. Because this spectator matter leaves the reaction zone with almost the speed of light it receives a small push from the fireball region from the earliest times and only for a very short timescale. This so-called *directed flow*, v_1, thus probes the earliest stages of the collision and exhibits presumably features from preequilibrium dynamics (see e.g. [63] and references therein). However, due to the strong longitudinal motion of the nuclei, it is difficult to disentangle the longitudinal dynamical features generated in the collision from the ones that were present before collision.

So far the most influential data from the RHIC experiments are taken around mid-rapidity, and we will focus on these in the following. Within hydrodynamic simulations, the fourth coefficient v_4 was found in simulations to be impractically small [74] and in fact to date no values have been published at SPS or RHIC energies.

When simply referring to 'elliptic flow', or 'v_2' one is referring to elliptic flow fully integrated over transverse momenta, which still depends on the impact parameter b, i.e.

$$v_2(b) = \frac{\int p_{\rm T}\, dp_{\rm T}\, v_2(p_{\rm T};\, b) \, \frac{dN}{p_{\rm T} dp_{\rm T} dy}(b)}{\int p_{\rm T}\, dp_{\rm T} \, \frac{dN}{p_{\rm T} dp_{\rm T} dy}(b)} . \qquad (4.3)$$

Generally, the momentum integrals are limited by experimental acceptance. When comparing to experimental data, we apply the same cuts as given by the experimental setup.

4.1 Elliptic flow from hydrodynamics

In section 3.1, we have shown that the centrality dependence of the φ_p-averaged transverse momentum spectra is well captured by the hydrodynamic model. Over a large variety of impact-parameters we thus get a good description of the normalization factor on the right hand side of Equ. (4.2). Now we proceed to test how the model reproduces the second coefficient v_2 of the Fourier expansion – elliptic flow.

4.1.1 Centrality dependence of elliptic flow

The spatial anisotropy ϵ_x is the cause for the anisotropy in momentum space ϵ_p, which can be directly related to elliptic flow v_2 [74]. Within hydrodynamics one finds that to a fair degree the elliptic flow is directly proportional to the initial spatial anisotropy $v_2/\epsilon_x \sim$ const, independently of the beam energy [92]. We have already seen in Figure 2.12 that the buildup of momentum anisotropy saturates early and at almost the same value for a wide range of initial energies. Furthermore, the generation of anisotropies proceeds faster the harder the equation of state is (the higher the speed of sound $c_s = \sqrt{\partial p/\partial e}$). Fig. 4.1 displays the ratio v_2/ϵ_x, as a function of impact parameter and the detailed analysis reveals that there are small deviations from this simple proportionality only at large impact parameters (note the strongly suppressed zero of the vertical axis in Fig. 4.1). Collisions with small initial energy densities (e.g. at AGS energies) show that the elliptic flow cannot fully react to the initial deformation as the system freezes out

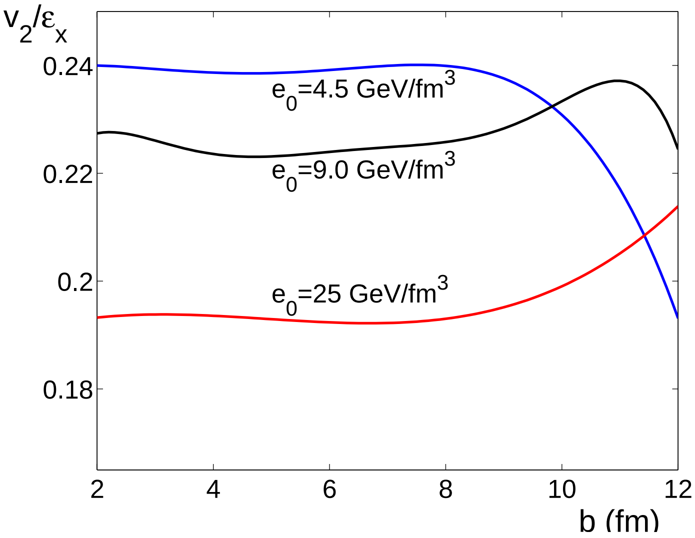

Figure 4.1: Centrality dependence of v_2/ϵ_x for three different initial energy densities leading to multiplicity densities as observed at the AGS (e_0 = 4.5 GeV/fm^3), the SPS (e_0 = 9.0 GeV/fm^3) and RHIC (e_0 = 25 GeV/fm^3).

too early in very peripheral collisions. Without the buildup of radial flow there can be no elliptic flow[1] [69]. Therefore v_2/ϵ_x drops monotonously with increasing impact parameter. For SPS energies however, before the ratio drops to zero in this way at large impact parameters there is a faint bump where the system reacts more strongly to the initial anisotropy than in the more central collision! This behavior shifts to larger impact parameters at RHIC energies resulting in a monotonous *increase* of v_2/ϵ_x as function of impact parameter up to impact parameters of $b \sim 13$ fm before it drops to zero.

By varying the centrality of the collision one has a handle on varying the energy densities in the system as discussed in Section 2.1. Therefore we will understand this phenomenon most easily when discussing the excitation function of elliptic flow in the next subsection. For the moment it is important to note that v_2/ϵ_x is surprisingly constant over a large range of impact parameters (considering the rich dynamics of the evolution which was the subject of Section 2.5).

As discussed earlier, the impact parameter and therefore the spatial eccentricity of each individual collision cannot be directly accessed experimentally, and hence the centrality is classified by other observables. In the first reported study of elliptic flow in collisions at RHIC at $\sqrt{s_{\rm NN}} = 130$ GeV, which was published even while the RHIC experiments were still collecting data in the first run [2], the collisions were classified in 8 centrality bins simply with respect to the total number of emitted charged hadrons for each collision. In Fig. 4.2 we compare the experimental data to hydrodynamic calculations,[2] with the parameters tuned to fit the particle spectra from *central* collisions (Sec. 2.4). As the freeze-out temperature carries still a large uncertainty (the central single particle spectra are almost equally well described when varying $T_{\rm dec}$ by ±3%, due to the interplay of decoupling temperature and transverse flow) we give results for $T_{\rm dec} = 130 \pm 4$ MeV (the upper line corresponds to smaller temperature). Given the experimental uncertainties (systematic errors are not included in the experimental error bars), we find that the experimental anisotropies reach the hydrodynamic extreme for impact parameters $b \leq 7$ fm (corresponding to $n_{\rm ch}/n_{\rm max} \gtrsim 0.5$). This is even more impressive, considering elliptic flow studies at the SPS [12, 96, 97], where at these impact parameters the experimental data fell short by a factor of 2

---

[1] A strongly deformed freeze-out hypersurface can in principle also lead to anisotropic particle emission. However it was shown [69] that large anisotropies can only be achieved with unrealistic parameters. In addition, the qualitative behavior of the momentum dependence of elliptic flow can only be reproduced by including transverse flow.

[2] The experimental data studied in this work are generally averages over a finite pseudorapidity window, e.g. for the STAR elliptic flow analysis $|\eta| < 1.3$. This introduces a small correction [79] when comparing the results to $\eta = 0$ and $y = 0$, see Equ. (2.16). In all studies we adjusted this corrections for the individual acceptance of the experiment.

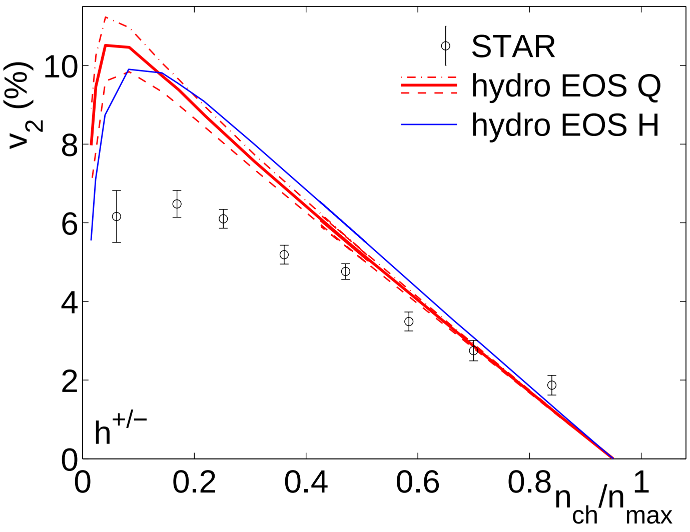

Figure 4.2: Centrality dependence of elliptic flow for charged hadrons [2]. The centrality is characterized through the number of produced particles, i.e. most central collisions are to the right. Hydro results including a phase transition (EOS Q) are for $T_{\rm dec}$ = 134 (dashed), 130 (thick solid), and 126 MeV (dash-dotted). Results for a purely hadronic gas are given for $T_{\rm dec}$ = 130 MeV (thin solid).

when integrated over all transverse momenta [96]. Only in a small range of transverse momenta up to $p_T = 0.35$ GeV, the elliptic flow of pions is in agreement with hydrodynamic calculations at $b \sim 7$ fm [74, 77], suggesting that at the SPS equilibration is not sufficient in non-central collisions for an ideal hydrodynamic treatment.

At RHIC this complete mapping of coordinate anisotropy to momentum anisotropy is a first indication that hydrodynamic conditions have been achieved. The overprediction of elliptic flow at large impact parameters is fully expected: in very peripheral collisions the initial particle densities and the fireball volume are too small to allow for rapid thermalization, and we will show in Sec. 4.2 that this leads to a reduced elliptic flow. Furthermore we have mentioned in Section 3.1 that simple 'thermal + flow' fits to the particle spectra indicate higher freeze-out temperatures in peripheral collisions and that this can be expected from the smaller system sizes. It also appears that the most peripheral collisions freeze out at such large temperatures (Section 3.4) that a full saturation of the elliptic flow before freeze-out is no longer possible. The mapping of the initial spatial anisotropy to momentum space is then incomplete. This effect is already visible in Fig. 4.2 when we increase $T_{\rm dec}$ from 126 to 134 MeV.

The influence of the phase transition and the curve labeled EOS H in Fig. 4.2 will be discussed in Section 4.3.

4.1.2 Excitation function for elliptic flow

Excitation functions are always of particular interest when studying phase transitions, as they might show threshold effects once the critical energy density for the transition is reached. Elliptic flow is a particular good candidate to exhibit critical features, as first found within microscopic model calculations [121]. Due to the softening of the equation of state, in the phase transition region, the development of elliptic flow should be inhibited, leading to a plateau in an otherwise monotonically rising function of the beam energy [120, 62]. Hydrodynamics predicts an even more dramatic influence of the mixed phase on the excitation function. This is shown in Fig. 4.3 where v_2 at fixed impact parameter ($b = 7$ fm) is given as a function of the final particle multiplicity to characterize the beam energy. The rich interplay between hard plasma phase, soft mixed phase and hadronic stage leads to a sharp maximum of elliptic flow at SPS collision energies followed by a relative minimum in the RHIC energy domain, where the excitation function turns again over to rise monotonically up into the LHC domain. At the lowest energies, the system apparently freezes out before the anisotropic pressure gradients could have generated all the flow anisotropies that they potentially can. Only if the system has enough time and freeze-out occurs sufficiently late, the coordinate space anisotropies can be fully transformed to momentum space anisotropies while the coordinate anisotropies reduce themselves to $\epsilon_x \approx 0$, see Section 2.5 and Fig. 2.12. At higher energies, the self-similar expansion in the mixed phase with its vanishing pressure gradients gets influential. While at RHIC energies, the momentum anisotropy does not change largely in the mixed

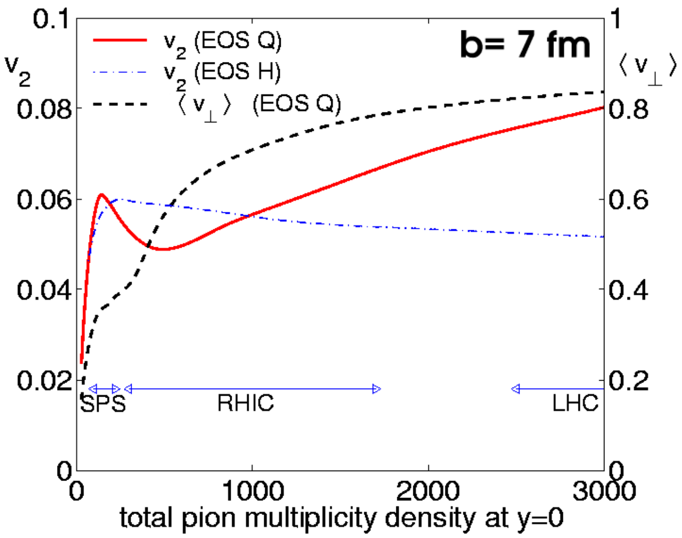

Figure 4.3: Excitation function of elliptic flow at ultra-relativistic beam energies (SPS, RHIC and LHC). The horizontal axis classifies the beam energy in terms of the produced particle density dN_π/dy. Shown are results for systems with and without phase transition, together with the average transverse flow for a system with EOS Q.

phase, the self similar expansion leads to a reduction of the coordinate anisotropy, thereby further reducing the driving force for a generation of elliptic flow in the hadronic stage. With the influence of the mixed phase getting stronger, we observe a reduction of the momentum anisotropies with beam energy, i.e. v_2 drops. At the highest energies, all momentum space anisotropies are generated already in the hard plasma stage of the collision. By the time the system enters the mixed phase we already have $\epsilon_x \approx 0$ and we therefore obtain a larger signal at the LHC than at RHIC energies. Whereas the momentum space anisotropy ϵ_p saturates as a function of beam energy (see also Fig. 2.12), the slopes of the particle spectra continue to grow, i.e. particle production of particles with high transverse momentum increases relative to low p_{T}-particles. As high p_{T} particles carry larger elliptic flow (see next Section), $v_2(\sqrt{s})$ continues to grow. Fig. 4.3 also contains the excitation function with a soft equation of state and no phase transition, labeled by 'EOS H'. Here of course we do not observe the minimum whose origin we could relate to the vanishing pressure gradients in the mixed phase of the equation of state. However it is intriguing to see that the hadronic equation of state also leads to a maximum in $v_2(\sqrt{s})$, and keeps decreasing slightly as a function of energy (or produced particles). This is a result of the softness of this equation of state ($\partial p/\partial e \approx 0.15$). While the system builds up momentum space anisotropy it will eventually overshoot to negative values of ϵ_x. If the system has time enough, it will then reduce the initially produced momentum anisotropies. This effect is stronger for the purely hadronic system than for the one with EOS Q, as its soft equation of state reacts more slowly on the coordinate space anisotropies. Therefore it overshoots to larger negative values of ϵ_x and needs a longer time (during which momentum anisotropies are reduced) to counterbalance these.

Now it is easy to understand the impact parameter dependence of the ratio v_2/ϵ_x from Fig. 4.1. Moving in Fig. 4.1 on a curve of fixed e_0 to larger impact parameters is rather similar to moving on the excitation function from higher multiplicities to lower multiplicities, where the multiplicity at the given e_0 sets the starting point on the horizontal axis. For AGS energies ($e_0 = 4.5$ GeV/fm^3), we are to the left of the peak in Fig. 4.3. With SPS energies we start a little to the right of the peak and sample it out by moving to larger impact parameters. With RHIC 1 energies we start close to the minimum of v_2 and the maximum response shows up only at the largest impact parameters.

Note that the dip in the excitation function of v_2, if experimentally confirmed, is a direct confirmation of the existence of a phase transition (with its associated softening of the equation of state). This sets it apart from many other quark-gluon plasma signatures which are only sensitive to the existence of a different kind of matter at high collision energies, but do not demonstrate that it is separated from normal matter by a phase transition. However, our argument is based on hydrodynamics and thus requires perfectly equilibrated systems at the discussed impact parameters, a prerequisite that is not met at the SPS as we have seen earlier. Due to the improving equilibration at energies above the SPS the experimental data point towards a monotonically increasing excitation function for v_2 [133]. (Other interesting phenomena occur at lower energies for which we refer to [42, 43]).

It is unfortunate that the hadronization phase transition may thus be shrouded by non-equilibrium features; the dip in the v_2-excitation function is the best candidate for a phase-transition signature in a single particle observable which has been suggested so far. Under this aspect, central collisions between properly oriented deformed nuclei such as U+U acquire a new importance. They allow for a study of the excitation function of v_2 in much larger systems than those formed in semi-central Pb+Pb collisions, and may thus reduce the importance of non-equilibrium dynamics. Experimentally it might not be possible to trigger exactly on the side-on-side configuration (see Fig. 4.4), but only on collisions with full overlap (zero spectators), thereby reducing the effective spatial deformation ϵ_x in the initial state and thus the expected momentum anisotropy and v_2. However these systems may still allow to observe the hydrodynamically predicted non-monotonic behavior of $v_2(\sqrt{s}\,)$.

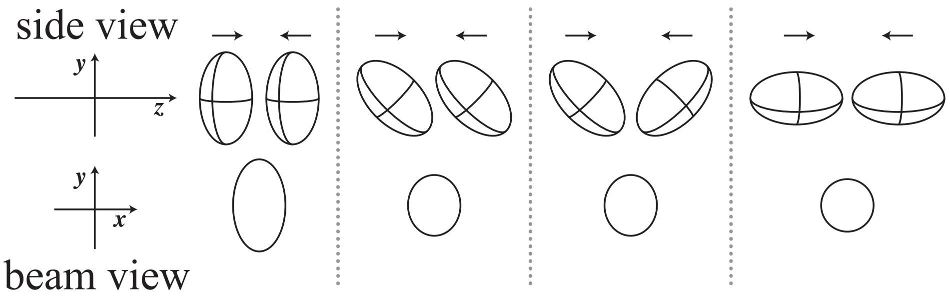

Figure 4.4: Possible configurations of collisions of deformed nuclei with no spectator matter. The top row shows a side-view of a side-on-side collision at the very left, and a tip-on-tip collision at the very right. The lower row are the corresponding projections in the transverse plane, showing large anisotropy in the side-on-side configuration and azimuthal symmetry for the tip-on-tip collision.

Fig. 4.3 furthermore shows the excitation function of the mean transverse flow of Section 3.4. The mean transverse flow is also sensitive to the reduced pressure gradients from the phase transition region, but even for a strong first order transition the corresponding effects do not generate a non-monotonic structure in the excitation function. The bend in the excitation function of $\langle v_\perp \rangle$ is a much weaker phase transition signature than the dip in the excitation function of v_2.

4.1.3 MOMENTUM DEPENDENCE OF ELLIPTIC FLOW

The first set of available data was also investigated for anisotropies as function of the transverse momentum of the particles, averaging over all collected events ('minimum bias' collisions). Weighting with the particle multiplicities observed at each impact parameters minimizes the experimental error [2], and we therefore use the same prescription,

$$v_2(p_\mathrm{T}) = \frac{\int b\,db\, v_2(p_\mathrm{T};\, b) \frac{dN_\mathrm{ch}}{dy p_\mathrm{T} dp_\mathrm{T}}(b)}{\int b\,db\, \frac{dN_\mathrm{ch}}{dy p_\mathrm{T} dp_\mathrm{T}}(b)}\,. \tag{4.4}$$

Both integrals run from zero to b_max, which is given by the experimental cut-off on which collisions still have sufficient particle multiplicities to be regarded in the data set. In the following we will use $b_\mathrm{max} = 13.5$ fm, corresponding to the 'minimum bias cut' given by STAR [2].

Fig. 4.5 shows striking agreement of hydrodynamic calculations and experimental anisotropies over the full shown transverse momentum range. (Note that fewer than 1 % of all particles have $p_\mathrm{T} > 2$ GeV.) This is of special interest as other models, in particular microscopic models, give much less flow anisotropies. The 'low density limit' [62], where anisotropies are generated by at most one single interaction of each individual particle, gives anisotropies of about a factor 2 smaller, even under the most optimistic assumptions [77]. Traditional parton cascades with initial densities such as those expected from perturbative QCD calculations give even less than half of the observed value, and only by assuming initial gluon densities or partonic cross sections an order of magnitude larger than traditional estimates, the measured anisotropies can be reproduced [91].

Obviously the microscopic dynamics of the collision are not under theoretical control, and the rescattering in the expanding system is larger than anything known before. This has caused a spur for the invention of new microscopic scattering mechanisms. String models claim to be able to reproduce the large anisotropies by exciting the strings via color exchange [135] or by 'melting' of the produced strings [86]. Both are very recent ideas, and it remains to be seen, which of the models provide greater consistency with the overall body of experimental observables.

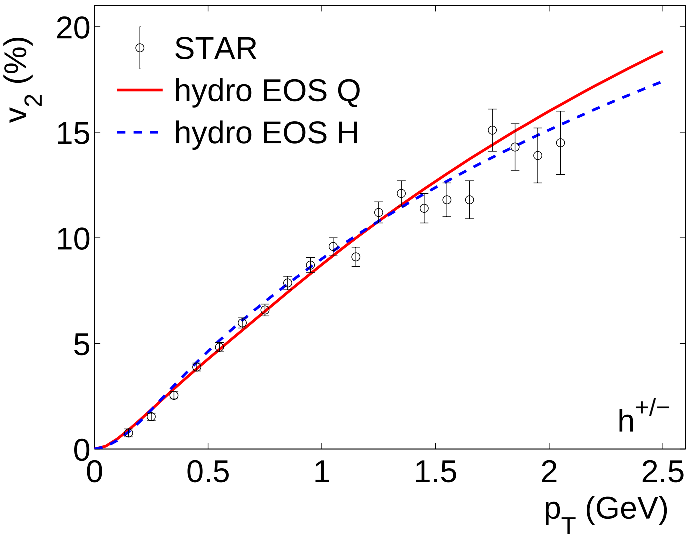

Figure 4.5: Elliptic flow of charged hadrons for minimum bias events; hydrodynamics compared to first published data from RHIC [2]. The influence of the freeze-out temperature (see Fig. 4.2) is within the line-width of the hydro curves. The dashed line shows results with the hadronic EOS.

4.1.4 Elliptic flow at high transverse momentum

From the observation discussed up to now we conclude that the created fireball shows signs of strong rescattering, unequivocally observed by the large anisotropies of particle emission. However at very high transverse momentum not all particles can have been completely equilibrated: the fastest particles simply escape from the reaction zone before having undergone a sufficient number of collisions to equilibrate their transverse momentum with the rest of the medium. From this argument, one expects elliptic flow to increase at low transverse momentum following the hydrodynamic prediction, but then fall below the hydrodynamic limit and eventually turn back to $v_2 \equiv 0$ at asymptotically high p_T (due to asymptotic freedom, very high p_T particles should not rescatter at all) [129]. The high-p_T particles in between hydrodynamic and asymptotic limit suffer radiation loss: in the high temperature phase particles with high energies are stimulated to radiate soft gluons, thereby reducing their momentum [54]. If the volume through which the partons travel is deformed in coordinate space, this energy loss will vary with the direction of the emitted partons. For an out-of-plane oriented ellipsoidal shape, as in the case of non-central heavy ion collision, the initial 'jets' traveling in the short direction will experience less energy loss than the ones traveling in the long direction of the initial oval, resulting in finite, positive elliptic flow also for non-equilibrated high p_T particles [129, 55]. However, by taking into account that the medium is not static but rather includes the strong transverse expansion the anisotropies due to energy-loss are smaller [56].

The most recent (preliminary) data on elliptic flow with sufficient statistics up to $p_\mathrm{T} \sim 4$ GeV clearly show deviations from the hydrodynamic anisotropies.

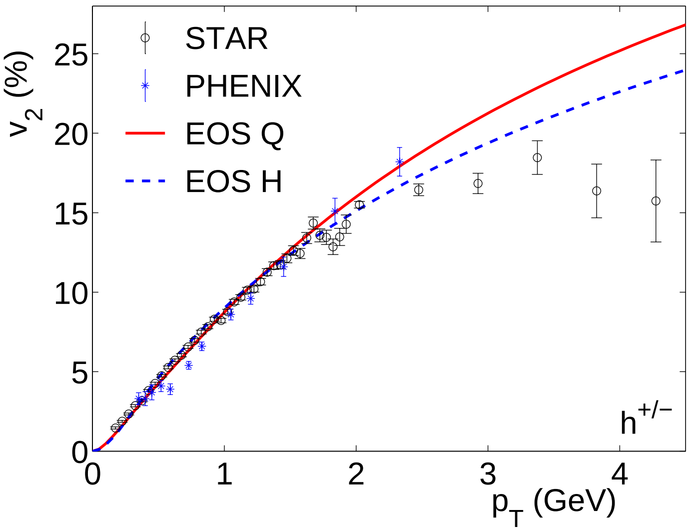

Figure 4.6: Preliminary results on elliptic flow of charged hadrons with high transverse momentum from STAR [115] and preliminary data from PHENIX [80] in comparison with hydrodynamic calculations with and without a phase transition.

In fact the experimental results saturate at $v_2 \approx 15\%$ whereas the hydrodynamic results keep increasing monotonically,[3] Fig. 4.6. Particles with momenta up to $p_\mathrm{T} \sim 2$ GeV seem to be fully equilibrated. Looking at the single-particle spectra, this represents more than 99% of all produced particles!

4.1.5 ELLIPTIC FLOW OF IDENTIFIED PARTICLES

Flow phenomena are known to have a strong influence on the mass systematics of particle spectra. This can be studied by taking the derivative of the logarithm of the transverse mass spectrum Eq. (3.4) [84, 109] which gives the slope of the spectrum in a semi-logarithmic plot. One quickly finds [109] that in the high m_T-limit the slope is given by $T_\mathrm{blue} = T\sqrt{\frac{1+v}{1-v}}$, (Eq. 4.1), independently of the particle rest mass (v is the average velocity of the fluid on the freeze-out hypersurface, T is the temperature according to which the particles are distributed in the local rest-frame of the fluid-cells). At smaller m_T the spectra show a characteristic curvature, which is the stronger the larger the transverse flow is. In this m_T-region the transverse mass spectra of particles with higher rest mass are flattened more strongly than those of light particles.

To obtain a similar qualitative understanding for the mass-dependence of flow anisotropies we investigate as a simple model four point like sources of which two travel with velocity $\pm v_x$ in the reaction plane along the x-axis and the two other

---

[3] The (nonphysical) limit of our calculations is $v_2 = 100\%$, as particles of highest p_T are strongly biased towards the cells traveling with larger velocities in x-direction.

with velocity $\pm v_y$ along the y-axis, and we assume $v_x > v_y$ [68]. In the Boltzmann approximation, these four sources lead to a particle distribution with an angular dependence given by

$$\frac{dN}{dyp_\mathrm{T}dp_\mathrm{T}d\varphi_p} \propto e^{-\gamma_x E/T}\cosh\left(\frac{\gamma_x v_x}{T}p_\mathrm{T}\cos\varphi_p\right) + e^{-\gamma_y E/T}\cosh\left(\frac{\gamma_y v_y}{T}p_\mathrm{T}\sin\varphi_p\right) . \tag{4.5}$$

Using the integral representation of the modified Bessel function $\mathrm{I}_n(z) = \pi^{-1}\times \int_0^\pi d\varphi\, e^{z\cos\varphi}\cos(n\varphi)$ [1] we can easily evaluate the elliptic flow $\langle\cos 2\varphi\rangle$ of this distribution to arrive at

$$v_2(p_\mathrm{T};m) = \frac{\mathrm{I}_2\left(\frac{\gamma_x v_x}{T}p_\mathrm{T}\right) - e^{\frac{\gamma_x-\gamma_y}{T}E}\,\mathrm{I}_2\left(\frac{\gamma_y v_y}{T}p_\mathrm{T}\right)}{\mathrm{I}_0\left(\frac{\gamma_x v_x}{T}p_\mathrm{T}\right) + e^{\frac{\gamma_x-\gamma_y}{T}E}\,\mathrm{I}_0\left(\frac{\gamma_y v_y}{T}p_\mathrm{T}\right)} , \tag{4.6}$$

where the energy $E = \sqrt{m^2 + p_\mathrm{T}^2}$ is the only expression which carries the mass dependency (we study again particles at midrapidity, $y = 0$). The difference in the numerator shows that particles with high mass have smaller elliptic flow at the same transverse momentum (for $v_x > v_y$).

In the previous section we have seen that for intermediate transverse momenta, the elliptic flow scales approximately linearly with the momentum. We can understand this by expanding the Bessel functions for large arguments as $\mathrm{I}_n(z) = \frac{e^z}{\sqrt{2\pi z}}(1 - \frac{4n^2-1}{8z} + ...)$ which makes the 'difference/sum'-structure of Eq. (4.6) collapse into

$$v_2(p_\mathrm{T};\, m) \approx \tanh\left(\frac{\kappa p_\mathrm{T} - \lambda m_\mathrm{T}}{2T} + \mu/4\right) \tag{4.7}$$

with $\kappa = \gamma_x v_x - \gamma_y v_y$, $\lambda = \gamma_x - \gamma_y$ and $\mu = \ln\frac{\gamma_x v_x}{\gamma_y v_y}$. For $p_\mathrm{T} \gg m$ this simplifies even further (keeping only the dominant term with the p_T dependence and neglecting the term $\sim \mu/4$) to

$$v_2(p_\mathrm{T}) \approx \tanh\left((T_y^{-1} - T_x^{-1})p_\mathrm{T}/2\right) \text{ , with } T_i = T\sqrt{\frac{1+v_i}{1-v_i}} . \tag{4.8}$$

Because elliptic flow is smaller for heavier particles, we also note that the turnover of $v_2(p_\mathrm{T})$ from a quadratic behavior at low p_T [41] to the observed linear (or better tanh-, Eq. (4.7)) dependence on p_T occurs at larger transverse momenta the heavier the particle under consideration is.

We can understand the dependence on the freeze-out temperature by taking the derivative of Eq. (4.7) with respect to T, which results in

$$\frac{\partial v_2}{\partial T}(p_\mathrm{T};m) \approx \frac{\lambda m_\mathrm{T} - \kappa p_\mathrm{T}}{2T^2}\cosh^{-2}\left(\frac{\kappa p_\mathrm{T} - \lambda m_\mathrm{T}}{2T} + \mu/4\right) . \tag{4.9}$$

With $\kappa > \lambda$ we see that the sign of this derivative depends on the mass of the particle (at fixed p_{T}). The elliptic flow of light particles can decrease with a higher temperature, whereas the elliptic flow of heavier particles can simultaneously increase, and vice versa.

After having gained a qualitative understanding on the mass-dependence of elliptic flow, we now compare the full hydrodynamic calculation to elliptic flow of identified particles in minimum-bias collisions. Figure 4.7 shows that the full hydrodynamic calculation is quantitatively in excellent agreement with the experimental data of identified pions. The hydrodynamic calculations are shown for three different freeze-out temperatures as in Fig. 4.2 ($T_{\mathrm{dec}} = 126$ (dash-dotted), 130 (solid) and 134 MeV (dashed line)). Proton anisotropies appear a little large when compared to the data. With EOS H (thin solid line) the disagreement is much worse; this will be discussed in Sec. 4.3. The slight discrepancies in the proton anisotropies might be attributed to the larger cross sections of the protons which could lead to a lower freeze-out temperature for this particle species. In the qualitative discussion above, we have seen that a lower freeze-out temperature would in fact lead to smaller elliptic flow, as suggested by the data. However our freeze-out temperature is trimmed to fit the single particle spectra of antiprotons in central collisions - this fit would be endangered by a large variation of the decoupling temperature. And as Figure 4.7 suggests, varying the decoupling temperature by 3% does not change the elliptic flow very much. On the other hand, a softer equation of state with an even larger latent heat would also lead to a bigger suppression of elliptic flow [124, 126]. This would also have a larger influence on the particles the higher their mass is, while it would not destroy the fit to the single particle spectra.

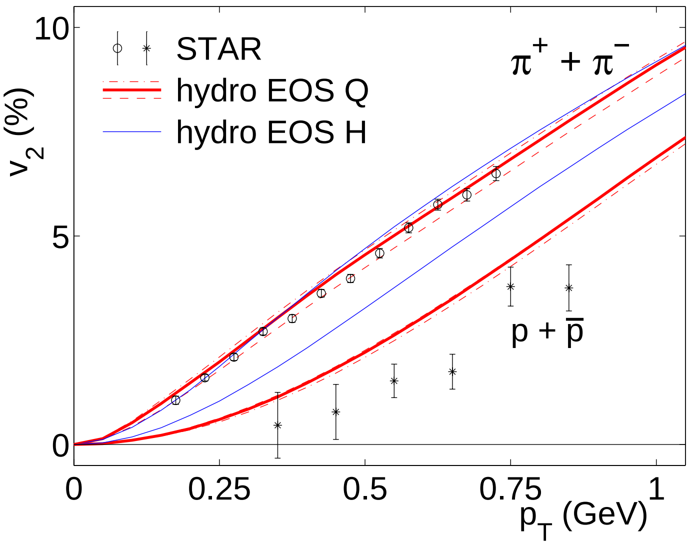

Figure 4.7: Minimum bias elliptic flow for identified particles from STAR [9] compared to full hydrodynamic calculations. Results for a system including a phase transition are given for $T_{\mathrm{dec}} = 126$ (dash-dotted), 130 (solid) and 134 MeV (dashed line), results for a purely hadronic system are for $T_{\mathrm{dec}} = 130$ MeV (thin solid).

4.1.6 Fully differential elliptic flow

The results on p_T-dependent elliptic flow presented so far always included an averaging over all impact parameters (minimum bias). As we argued before, the hydrodynamic description is likely to break down at large impact parameters, and therefore the qualitative agreement of hydrodynamics and the experimental data is even more surprising. However, large impact parameters are suppressed by the weighting of the centralities with the corresponding multiplicities (Eq. 4.4). The ultimate tool for a comparison of data with hydrodynamic results is the differential elliptic flow of different particle species in small centrality bins. First results of this kind were recently reported by the STAR collaboration [9] and are reproduced in Fig. 4.8 together with the hydrodynamic results in corresponding impact parameter bins.

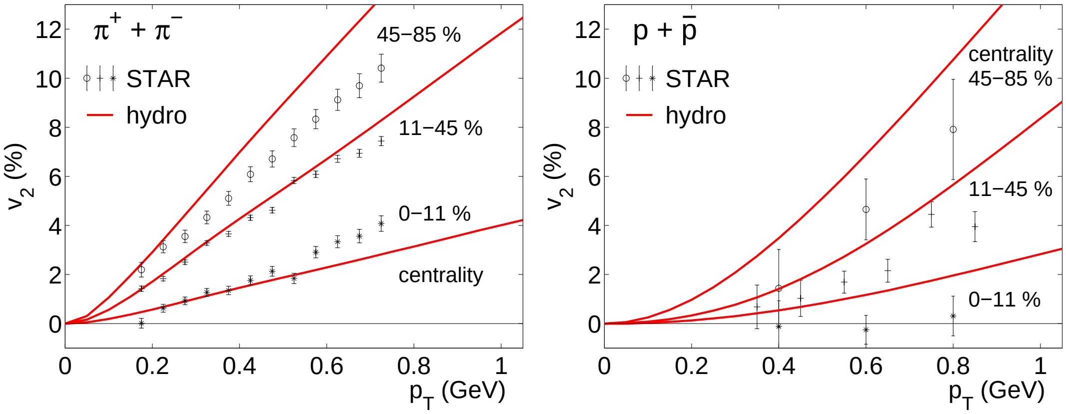

Figure 4.8: Elliptic flow in three different centrality bins for pions (left) and protons (right) from the STAR experiment [9], compared to hydrodynamic calculations at three different centralities (see text).

As in the STAR analysis of the centrality dependence of p_T-integrated elliptic flow, the centrality is again determined by the particle multiplicity in the final state. In Table 4.1 we summarize the STAR centrality cuts in terms of the fractional cross sections, the particle yield and the corresponding hydrodynamic impact parameter cuts. These impact parameters define the integration region of the integrals in Eq. (4.4).

Figure 4.8 nicely shows the good agreement of hydrodynamics and the pion data at low p_T and collisions with not too large impact parameters. For the most peripheral collisions with impact parameters larger than 9 fm the agreement is lost. The proton elliptic flow turns out a little too large in the hydrodynamic calculation, for all three centrality cuts (see the discussion in the previous subsection).

Bin	fraction of total cross section	$n_{\text{ch}}/n_{\max}$	$b_{\min} - b_{\max}$
1	0 – 11 %	1 – 0.63	0 – 5.5 fm
2	11 – 45 %	0.63 – 0.207	5.5 – 9.0 fm
3	45 – 85 %	0.207 – 0.023	9.0 – 13.5 fm

Table 4.1: Centrality binning of the STAR data and the hydrodynamic impact parameter cuts for the differential elliptic flow study in Fig. 4.8.

4.2 INDICATIONS FOR *early* THERMALIZATION

The large anisotropies in the particle emission are a collective phenomenon: if the nucleus-nucleus collisions were a simple superposition of independent nucleon nucleon collisions, the resulting particle emission would be isotropic in momentum space. The individual reaction processes would be 'blind' to the geometry of the collision. Only strong rescattering can transform the initial spatial anisotropies to momentum anisotropies. In fact, it turns out that in the hydrodynamic picture the initial spatial anisotropy is approximately proportional to the final state momentum anisotropy measured by the elliptic flow v_2. This is true for a large domain of centralities at various beam energies, as shown in Figure 4.1.

Now if thermalization were not to set in so early, but the system would dilute simply as a result of the random, locally azimuthally symmetric motion of the partons for an extended time period, the initial ellipsoid would get blown up in space and the coordinate space anisotropy (i.e. the ratio of the long to the short direction) would be strongly reduced. If thermalization and pressure build-up would occur only at the end of this free-streaming period, the resulting value of ϵ_x and therefore the anisotropies in the pressure gradients would be much smaller, leading to a much lower momentum anisotropy v_2. Here we give a short estimate of this effect. In Subsection 5.4.1 and Appendix C we will treat such a pre-equilibrium scenario in even more detail.

Let us consider massless particles emitted with zero longitudinal momentum $y = 0$ in the transverse plane $z = 0$ (the following generalizes an argument first presented in [75]). If our initial transverse momentum distribution needs an additional time Δt for thermalization, the free-streaming prescription gives the transverse momentum distribution at that later time $t_0 + \Delta t$ as

$$f(\vec{r}_\perp,\, t_0 + \Delta t;\, \vec{p}_\mathrm{T}) = f(\vec{r}_\perp - \vec{e}_p\,\Delta t,\, t_0;\, \vec{p}_\mathrm{T})\,. \tag{4.10}$$

At this later time we obtain for the spatial anisotropy ϵ_x (Eq. 2.7) the value

$$\begin{aligned}\epsilon_x(t_0 + \Delta t) &= \frac{\int dxdy\,(y^2 - x^2)\,\int d^2p_\mathrm{T}\, f(\vec{r}_\perp - \vec{e}_p\,\Delta t,\, t_0;\, \vec{p}_\mathrm{T})}{\int dxdy\,(y^2 + x^2)\,\int d^2p_\mathrm{T}\, f(\vec{r}_\perp - \vec{e}_p\,\Delta t,\, t_0;\, \vec{p}_\mathrm{T})} \qquad (4.11)\\ &= \frac{\int dxdyp_\mathrm{T}dp_\mathrm{T}d\varphi_p\,\left((y + \Delta t \sin\varphi_p)^2 - (x + \Delta t \cos\varphi_p)^2\right)\, f(\vec{r}_\perp,\, t_0;\, \vec{p}_\mathrm{T})}{\int dxdyp_\mathrm{T}dp_\mathrm{T}d\varphi_p\,\left((y + \Delta t \sin\varphi_p)^2 + (x + \Delta t \cos\varphi_p)^2\right)\, f(\vec{r}_\perp,\, t_0;\, \vec{p}_\mathrm{T})}\,.\end{aligned}$$

Using that $f(\vec{r}_\perp,\, \vec{p}_\mathrm{T}, t_0)$ is even in x and y and assuming that at the initial time t_0 the partons have a locally isotropic momentum distribution, we arrive at

$$\epsilon_x(t_0 + \Delta t) = \epsilon_x(t_0)\frac{1}{1 + \frac{\Delta t^2}{\langle x^2 + y^2\rangle}} \tag{4.12}$$

So for typical system sizes resulting from collisions with finite impact parameter with (approximate) average Gaussian radii of $R \sim$ 3–4 fm, an additional preequilibrium period of 1 – 2 fm/c would already result in a reduction of the elliptic flow signal of approximately 10 – 30 %. This is of course the most straightforward possible explanation of the shortfall of elliptic flow in the very peripheral collisions of Fig. 4.2: larger impact parameters lead to less dense systems, therefore the system needs a larger time to allow for sufficient rescattering that drives the system into local equilibrium. In addition, as we have argued earlier, the smaller systems created at finite impact parameters are also expected to freeze out at higher temperatures. If this temperature effect is sufficiently large, the system freezes out before all of the elliptic flow can be generated, driving the flow anisotropies down even further and bringing the pure hydrodynamic results of Figure 4.2 in agreement with experimental data even in the most peripheral collisions. Of course, this is a qualitative argument and it remains to be seen whether it can be made quantitatively (which we don't do here).

4.3 Elliptic flow and the phase transition

In some of the results presented in Section 4.1 we included results from calculations with an underlying purely hadronic equation of state which does not undergo a phase transition to a hard plasma stage at any temperature (EOS H from Section 2.2.2). The initial parameters of these simulations were tuned in the spirit of the other calculations, such as to reproduce pion and proton spectra from *central* collisions, giving fits equivalent to the ones presented in Figure 2.10. The relevant parameters are given in Table 2.1.

The anisotropic flow of all charged hadrons does not show a large sensitivity on the equation of state, neither when plotted versus centrality (Fig. 4.2) nor when shown as a function of transverse momentum (Fig. 4.5). This is, however, to our advantage, as it implies that the analysis of 'all charged hadrons' is not strongly influenced by our ignorance and limited knowledge of the details of the nuclear equation of state. It appears that the anisotropic flow of all hadrons finds a limiting, maximum value well before freeze-out independently of the equation of state. Even if the pressure gradients are as small as in a hadronic resonance gas, with a speed of sound of only $c_s = \sqrt{\partial p/\partial e} \approx \sqrt{0.15}$, the initial spatial anisotropy can be fully transformed into anisotropic flow before freeze-out occurs. In every case the same large elliptic flow signal is produced. Important is that the transformation of spatial to momentum anisotropy within the hydrodynamic evolution has to start early and the anisotropies are generated by *early pressure*.

However, with the rest mass dependence of the elliptic flow we have identified an observable which shows large sensitivity to the equation of state, see Figure 4.7. Again, the light particles, the pions, do not show sensitivity to the equation of state (therefore the sensitivity of 'all charged hadrons' is minute, as they are dominated by the large pion abundances). The heavier protons however show a much later onset of elliptic flow as a function of the transverse momentum in the case of a phase transition to a hard plasma phase. The data on anisotropic flow of protons clearly favor the phase transition scenario. Within a hybrid model, Derek Teaney et al. found from similar arguments that the data favor an equation of state with a latent heat between 0.8 and 1.6 GeV/fm^3 [125, 126].

In this context it remains to be stressed again that a profound maximum in the excitation function of elliptic flow at a fixed impact parameter, Figure 4.3, can be traced back uniquely to the mixed phase of the underlying equation of state. However we have cautioned that this feature is only observable if equilibration in non-zero collisions is achieved over a large variety of collision energies (Section 4.1.2).

4.4 A BLAST WAVE MODEL FOR ANISOTROPIC PARTICLE EMISSION

It is desirable to have a simple parametrization of the particle emitting source which captures the main features and phenomena one wants to investigate. Such descriptions then allow for rapid fitting procedures to the experimental data without running a full, time consuming microscopic/macroscopic calculation to incorporate the dynamical evolution of the systems. The results do not only lead to a powerful classification of the observables, but also reveal important systematics that can be used to extract physical processes which underlie the data sample. On the other hand, of course, true physical understanding only arises after making sure that the fit parameters extracted from the data are indeed compatible with a full dynamical calculation.

Effective parametrizations of this kind are readily available for central collisions, with different degrees of sophistication. These parametrizations allow for example the description of the hadronic particle spectra in terms of only two variables, the average radial flow velocity at freeze out and the decoupling temperature [113, 58, 109]. This has led to an understanding of the flattening of the particle spectra with increasing system size and/or increasing beam energies as being mostly due to increased transverse flow [8, 43, 33].

For the purposes of describing the new feature of anisotropic particle emission in non-central collisions, we modify the simple Siemens and Rasmussen blast wave model [113] by replacing their spherical fireball by a cylindrical collision region, as more appropriate for RHIC energies, and implementing a radial rapidity $\rho(\vec{r}_\perp)$, which has a modulation of amplitude $\rho_a(r)$ with respect to the azimuth $\varphi_s = \arctan(x/y)$ such that

$$\rho(r,\, \varphi_s) = \rho_0(r) + \rho_a(r) \cos 2\varphi_s \,. \tag{4.13}$$

A positive amplitude ρ_a then indicates larger flow velocities in x- than in y-direction. Together with the longitudinal Bjorken flow field (Section 2.2.3) the four flow velocity then becomes

$$u^\mu(x) = \cosh\rho\, (\cosh\eta,\, \tanh\rho \cos\varphi_s,\, \tanh\rho \sin\varphi_s,\, \sinh\eta) \tag{4.14}$$

and therefore

$$u^\mu p_\mu = \frac{m_{\mathrm{T}} \cosh\rho}{T} \cosh(\eta - y) - \frac{p_{\mathrm{T}} \sinh\rho}{T} \cos(\varphi_s - \varphi_p)\,. \tag{4.15}$$

Furthermore, we assume for simplicity that the particles with low transverse momenta p_{T}, which are investigated here, are emitted *in a flash*, at a fixed longitudinal proper time τ_f which is independent of $\vec{r}_\perp$ (we will study the time-sequence of particle emission in more detail in Section 5.1 and justify this assumption there). This reduces the four product of the momentum of the particle and the normal vector on the freeze-out hypersurface, Eq. (A.28), as it appears in the integral for the evaluation of the particle spectra, Eq. (2.23), to the simple expression [104, 108]

$$p^\mu d^3\sigma_\mu = m_{\mathrm{T}} \cosh(\eta - y)\, \tau_f(x,\, y)\, dx dy d\eta\,. \tag{4.16}$$

After integrating over the space-time rapidity as in Appendix A.2 one arrives at the transverse momentum spectrum

$$\begin{aligned} \frac{dN}{dy p_{\mathrm{T}} dp_{\mathrm{T}} d\varphi_p} &= \frac{2\, g_i\, m_{\mathrm{T}}}{(2\pi)^3} \sum_{n=1} (\mp)^{n+1}\, e^{n\,\mu/T} \times \\ & \times \int dr d\varphi\, \tau_f\, r\, e^{n\,\alpha_\perp(\varphi+\varphi_p)\cos\varphi} \mathrm{K}_1(n\,\beta_\perp(\varphi+\varphi_p))\,, \end{aligned} \tag{4.17}$$

with the two abbreviations

$$\beta_\perp(\varphi) = \frac{m_{\mathrm{T}}}{T} \cosh(\rho(r,\, \varphi)) \quad \text{and} \quad \alpha_\perp(\varphi) = \frac{p_{\mathrm{T}}}{T} \sinh(\rho(r,\, \varphi))\,. \tag{4.18}$$

In the spirit of the blast wave model, we assume particle freeze-out only from a thin shell of the collision region, leading to a collapse of the radial integration in Eq. (2.23) which can only be done numerically. (This process can be thought of as replacing the radial rapidity profile $\rho(r, \varphi_s)$ by a fixed radial average value $\bar{\rho}(\varphi_s)$.) Elliptic flow is then evaluated as the average of $\cos(2\varphi_p)$ over this distribution and after some trivial manipulations and using the integral definition of the Bessel function of the first kind

$$\mathrm{I}_k(\alpha) = \frac{1}{2\pi} \int_0^{2\pi} d\psi\, e^{\alpha \cos\psi} \cos k\psi\,, \tag{4.19}$$

one arrives (neglecting chemical potentials) at [68]

$$v_2(p_{\mathrm{T}}) = \frac{\sum_{n=1} (\mp)^{n+1} \int d\varphi\, \cos 2\varphi\, \mathrm{I}_2(n\,\alpha_\perp(\varphi)) \mathrm{K}_1(n\,\beta_\perp(\varphi))}{\sum_{n=1} (\mp)^{n+1} \int d\varphi\, \mathrm{I}_0(n\,\alpha_\perp(\varphi)) \mathrm{K}_1(n\,\beta_\perp(\varphi))}\,, \tag{4.20}$$

where the minus sign applies for Fermions and the plus sign for Bosons.

For small transverse momenta up to $p_{\mathrm{T}} \approx 0.6$ GeV this simplistic model is in good agreement with the full hydrodynamic calculation when choosing appropriate parameters T, ρ_0 and ρ_a. It also reproduces the important features of the mass dependence of elliptic flow that were discussed earlier already in the Boltzmann approximation (keeping only the first terms in the sums). In this approximation, the STAR collaboration has used this formula to fit to elliptic flow data of pions, kaons and protons at low p_T [8], and extracted the parameters $T_\mathrm{dec} = 135 \pm 19$ MeV, $\rho_0 = 0.58 \pm 0.03$ and $\rho_a = 0.09 \pm 0.02$. The collaboration argued, that better fit results were obtained by introducing still another parameter to characterize a possible spatial anisotropy of the density of emitters. However, I find that giving up the Boltzmann approximation and keeping, at least for pions, more terms in the sums of Eq. 4.20 strongly improves the fit to the data, essentially eliminating the need for an additional azimuthal density modulation. Figure 4.9 shows the experimental data for pions and protons together with the blast wave curves for $T_\mathrm{dec} = 140$ MeV, $\rho_0 = 0.58$ and $\rho_a = 0.09$.

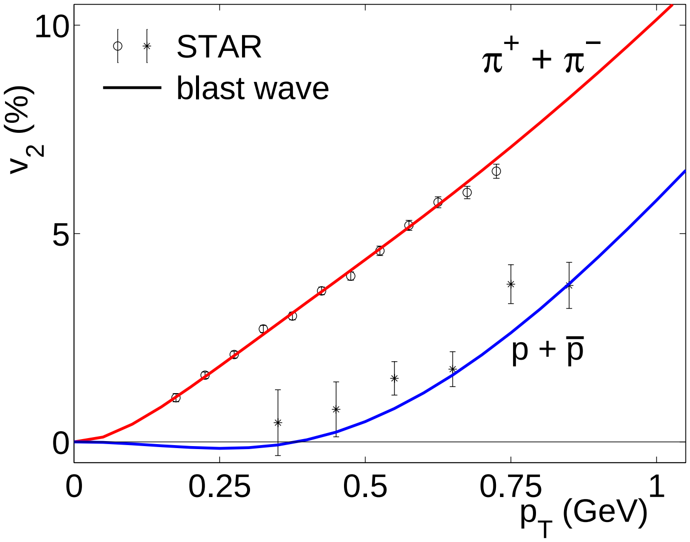

Figure 4.9: Elliptic flow from the blast wave model with $T_\mathrm{dec} = 140$ MeV, average radial rapidity $\rho_0 = 0.58$ and modulation amplitude $\rho_a = 0.09$.

Even though there is apparently nice agreement between the blast wave model and experimental data for elliptic flow at low p_T (Fig. 4.9), it should be used and its results interpreted with care. After all it relies on a blast wave freeze-out, i.e. it only considers particles emitted from a thin shell. This is known to lead to qualitative features like a peak in the transverse momentum spectra (the so called 'blast wave peak'), which is not observed in the data. It was found to disappear in more realistic models of freeze-out from a filled fireball, which consider freeze-out from a finite volume in space time [108]. For this reason, the application of Eq. 4.20 might also have its caveats. However, this possible drawback can be easily circumvented by numerically performing the radial integration in Eq. 4.17 and using a monotonically increasing profile for the radial rapidity $\rho_0(r)$ [89]. I have refrained from doing so because of the availability of fully dynamical hydro calculations which have all these features implemented anyway. It is only mentioned for the benefit of "data fitters" who want to use a semi-realistic blast wave model.

5

HBT RADII FROM HYDRODYNAMICS

In the preceding chapters the evidence for early thermalization and a subsequent hydrodynamic expansion was presented. The quality of the hydrodynamic description of essentially all momentum-space features of the data is impressive. The hydrodynamic description is therefore also expected to give a good representation of the space-time aspects of particle emission, i.e. the shape of the particle emitting surface and the time duration of the emission process. Experimentally this information is accessible through *correlations* in momentum-space, by using two-particle interferometry (the Hanbury-Brown and Twiss (HBT) effect [57]). Earlier hydrodynamic calculations [66, 103], have predicted that if the nuclear equation of state features a first order phase transition the system should show very long lifetimes, reflected in a long duration of the particle emission process. This in turn would leave signals in the parameters of the HBT-analysis, the HBT radii. Especially famous became the so-called $R_{\mathrm{out}}/R_{\mathrm{side}}$–ratio which was argued for to be a direct measure of the lifetime of the system, disentangling the dynamical effects of the expansion [103]. As we have seen, the prerequisites are fulfilled – however the large anticipated signal was not found at RHIC 1 [6, 70]. Instead of a predicted value $R_{\mathrm{out}}/R_{\mathrm{side}}$ of around 5 [103], it was found to be approximately 1, very similar to the ratio already observed at SPS energies [6]. Although our hydrodynamical calculations (whose initial and freeze-out conditions are much better constrained by data) give a considerably smaller $R_{\mathrm{out}}/R_{\mathrm{side}} \lesssim 2$ (see below), the problem relative to RHIC data persists. One might worry that by increasing the center of mass energy by an order of magnitude from SPS to RHIC 1 energies one has shot past the observability of a signal that might peak at energies in between. Runs at intermediate energies are planned for the near future which will also address this issue. However, given the success of our hydrodynamical model for the single-particle observables, it is difficult to believe that we got the time scales for the fireball evolution wrong by a large factor.

The HBT problem is not unique to hydrodynamic descriptions. So far no dynamical model calculation has been presented which can simultaneously explain the single particle spectra and HBT radii. In the following we will elucidate why the idealized hydrodynamic scenario (and in fact all other available models) give incorrect geometrical measures. We will show how the duration of particle emission and the regions of correlated particle emission are related to the observed R_{out} and R_{side}. In comparison with experimental data, we find that the former turns out too large in our calculations whereas the latter is too small. Possible resolutions of this discrepancy will be investigated.

5.1 THE SOURCE FUNCTION

In Section 2.3 we have discussed and motivated freeze-out of particles from a space-time hypersurface Σ which is defined in terms of a decoupling energy density e_{dec} or decoupling temperature T_{dec}. The contribution of an infinitesimal element $d^3\sigma_\mu(x)$ of this hypersurface to the total number of produced particles with momentum K^μ is given by the product of $K^\mu d^3\sigma_\mu$ and the local particle distribution function $f(u_\mu K^\mu,\, x)$. The source function is a function in four-dimensional space-time; it is zero everywhere except on the freeze-out hypersurface Σ where it amounts to the infinitesimal contribution just described. For hadrons of degeneracy g_i it is therefore given by [106, 37]

$$S_i(x,K) = \frac{g_i}{(2\pi)^3} \int_\Sigma \frac{K^\mu d^3\sigma_\mu(x')\delta^4(x-x')}{\exp\{\beta(x')[K\cdot u(x') - \mu_i(x')]\} \pm 1} \quad , \tag{5.1}$$

where $\beta = 1/T$ is the inverse temperature, μ_i the chemical potential and u the flow field (the upper sign applies for Fermions, the lower sign for Bosons).

Integrating the source function over space-time eliminates the δ-function and returns the Cooper-Frye prescription [39] for the particle spectra, which we encountered already in Eq. (2.23):

$$\int d^4x\, S_i(x,p) = \int_\Sigma p_\mu\, d^3\sigma(x)^\mu\, f_i(x,p) = E\frac{dN_i}{d^3p}\,. \tag{5.2}$$

This expression shows that the single-particle spectrum provides no information at all about the space-time structure of particle emission, since the latter has been integrated over.

In Appendix A.1.4 we show in detail how the assumption of longitudinal Bjorken flow leads to the normal vector on the freeze out hypersurface

$$d^3\sigma^\mu = \Big(\cosh\eta,\, \vec{\nabla}_\perp\tau_f(x,\,y),\, \sinh\eta\Big)\; \tau_f(x,\,y)\, dxdyd\eta\,, \tag{5.3}$$

where $\tau_f(x,\, y)$ is the parametrization of the freeze out hypersurface in the transverse plane ($\vec{\nabla}_\perp = (\partial/\partial x,\, \partial/\partial y)$). Writing the four-momentum of the particle as $K^\mu = (m_\mathrm{T} \cosh y_K,\, \vec{K}_\perp,\, m_\mathrm{T} \sinh y_K)$, see Eq. (A.23), one quickly arrives at

$$\begin{aligned} S_i(x,K) &= \frac{g_i}{(2\pi)^3} \int dx'dy'd\eta' \left(m_\mathrm{T} \cosh(y_K - \eta') - \vec{K}_\perp \cdot \vec{\nabla}_\perp \tau_f(x',\, y') \right) \\ &\quad \times \tau_f(x',y') f(x',y',K) \delta(x-x') \delta(y-y') \delta(z-z') \delta(t'(x',y',z')-t) \\ &= \frac{g_i}{(2\pi)^3} \left[m_\mathrm{T} \cosh(y_K - \eta) - \vec{K}_\perp \cdot \vec{\nabla}_\perp \tau_f(x',\, y') \right] \\ &\quad \times f(x,K) \delta(\tau - \tau_f(x,y)) \,. \end{aligned} \tag{5.4}$$

The last step was achieved by the transformation of the δ functions

$$\delta(z-z')\delta(t-t') = \frac{1}{\tau} \delta(\eta - \eta') \delta(\tau - \tau') \,, \tag{5.5}$$

and performing the then trivial coordinate integrals.

The source function is still a function of 4 space-time coordinates, although it is zero everywhere except on the freeze-out hypersurface Σ. It also depends on the particle four momentum K^μ. In Figure 5.1, we investigate the emission of charged pions with $m_\pi \approx 0.1396$ GeV and momenta $\vec{K}_\perp = 0$ and $0.5\, \vec{e}_x$ GeV (left and right column) and vanishing longitudinal momentum $K_l = 0$ ($y_K = 0$). To visualize the four dimensional function $S_\pi(x,\, K)$ at fixed K, we integrate out two of the Cartesian space-time coordinates. Integrating over $(z,\, t)$ allows to present the emissivity projected onto the transverse plane $(x,\, y)$, as displayed in the upper row of Fig. 5.1. Integrating over $(z,\, y)$ gives a representation of the time dependence of particle emission versus the transverse coordinate x which is shown in the lower row. The source function displayed is for central ($b = 0$) collisions at RHIC energy, namely the 'RHIC 1' configuration of the previous chapters. In the lower row of Fig. 5.1 we also indicate the shape of the freeze-out hypersurface $\tau_f(x)$ (dashed line). It shows three distinct phases: During the first few fm/c, transverse dynamics is gradually developing. In the beginning, however, it is not strong enough to keep up with the evaporation of the dilute rim of the overlap-functions, see Fig. 2.7. Therefore the radial size of the freeze-out hypersurface first shrinks. After some fm/c the transverse flow that has built up is strong enough to balance the evaporation from the surface by matter-transport from the dense interior; it even makes the hot core grow in the radial direction. Finally the interior core runs out of matter to keep up with the strong transverse plus longitudinal cooling and a rather sudden decoupling of the entire interior of the system takes place about 16 fm/c after the start of the hydrodynamic evolution. This happens almost instantaneously i.e. at constant longitudinal proper time,

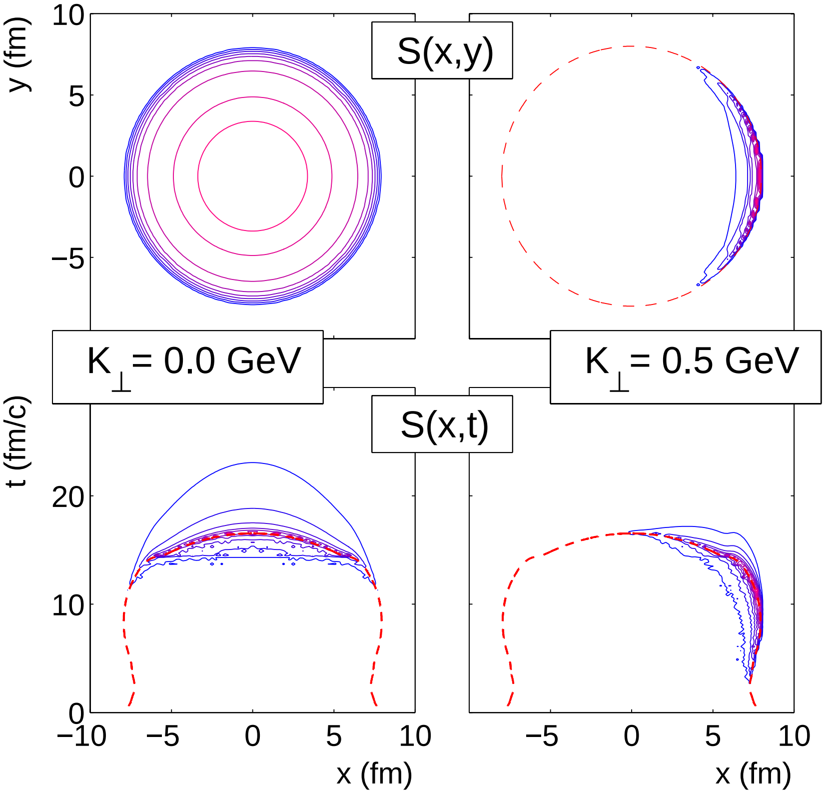

Figure 5.1: Source function for central RHIC 1 collisions with $K_\perp = 0$ (left column) and $0.5\,\vec{e}_x$ GeV (right column). The upper row has the longitudinal and time coordinate integrated out, the lower row the longitudinal and y-coordinate. The lower row also displays the freeze out hypersurface $\tau_f(x,\, y = 0)$ as the dashed line. The circle in the top right plot indicates the maximum inflation of the freeze-out hypersurface. Contours are plotted for 10, 20, ..., 90 % the maximum value.

just as we assumed in the blast wave calculations of Section 4.4. This freeze-out hypersurface is again displayed and discussed in more detail in Figure 5.5.

It is apparent that low momentum particles are emitted late in the collision and from a relatively large region centered near the origin. They are preferentially produced near the fireball center, because flow velocities are smallest there (the radial flow velocity must vanish by symmetry at $r = 0$). Therefore particles in the center experience the smallest 'blue-shift'. This is to be contrasted with the particles of non-zero transverse momentum, e.g. $K_x = 0.5$ GeV. Their production is already strongly biased towards the regions where the system develops its largest flow velocities. This happens rather late and from the largest possible

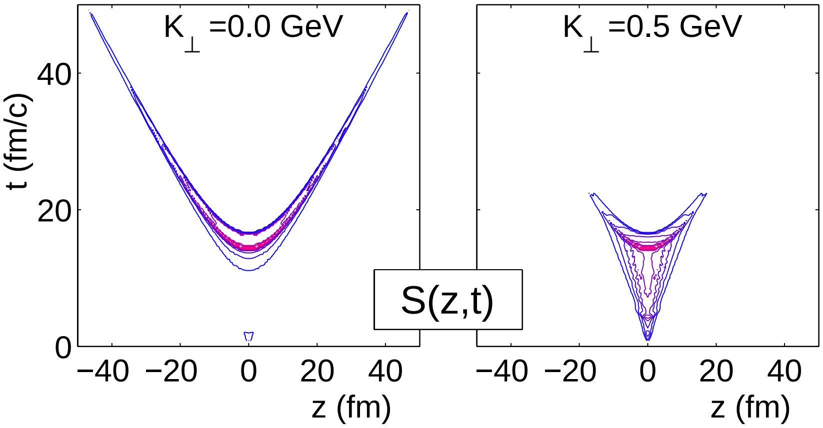

Figure 5.2: Source function as in Fig. 5.1 integrated over the transverse coordinates to show the emission density in the (z, t) plane. Contours are plotted for 10, 20, ..., 90 % the maximum value.

radial distances, when the system has reached its largest inflation, before the cooling process leads to the rapid evaporation of the entire fireball.

Even though particle emission in the transverse plane at $z = 0$ stops after $\tau_{\rm dec} \sim 16.5$ fm/c, there are contributions from slices of non-zero space-time rapidity η ($|z| > 0$), where the evolution is time-dilated by the gamma factor $\gamma = \cosh\eta$. This is apparent when investigating the emissivity as a function of (z, t), which is obtained after integrating the source function over (x, y), Figure 5.2. There the time dilation effects at finite z show up as prominent (approximate) hyperbolae along $\tau(z) = \sqrt{\tau^2(z=0) + z^2}$. Particle emission of particles with low momenta occurs rather late as we have seen in Figure 5.1. At late times, the longitudinal Bjorken flow field $v_z = z/t$ has only a small longitudinal gradient. Therefore a large number of particles with zero longitudinal rapidity is emitted form non-zero z's, where the random thermal motion can cancel the collective longitudinal motion). Therefore the contours of the source function are very similar to hyperbolae up to large values of z and t. This also results in a rather large non-Gaussian tail in the *emission duration* which we have already encountered in the (x, t) plane (lower left panel of Fig. 5.1). These important observations will play a significant role in our discussion of the HBT radii below.

5.2 Correlation lengths

The effective centers and widths of the emission regions in space-time can be quantified by studying the averages of the emission coordinates $\langle x\rangle$, $\langle y\rangle$, $\langle z\rangle$ and $\langle t\rangle$, and the *correlation lengths* defined as $\sqrt{\langle x_\mu x_\nu\rangle - \langle x_\mu\rangle\langle x_\nu\rangle}$, where the averages are to be taken with respect to the source function $S(x,K)$. For a general function of the coordinates $g(x,y,z,t)$ this average is

$$\langle g(x,y,z,t)\rangle(K) := \frac{\int d^4x\, g(x,y,z,t)\, S(x,K)}{\int d^4x\, S(x,K)}\,. \tag{5.6}$$

Note that it depends on the momentum K of the observed particles.

Again, the assumption of boost invariance helps to perform two of the four integrals in the numerator and the denominator analytically. This is executed in detail in Appendix B. Here we skip the technical details and concentrate on the results of the calculation. Figure 5.3 shows the various correlation lengths for RHIC 1 collisions, i.e. the correlation lengths of the source function whose projections onto two coordinates we have discussed in Figures 5.1 and 5.2.

The figure clearly shows the trend that particles with the largest transverse momentum $K_\perp$ are emitted from the rim of the hypersurface at its largest extension: Both $\langle x\rangle$ and $\langle x^2\rangle^{1/2}$ slowly converge to $r_{\text{max}} = 8$ fm in the limit of large $K_\perp$. Naturally $\langle x\rangle$ vanishes for $K_\perp = 0$ by symmetry, but $\langle x^2\rangle^{1/2} \approx 4$ fm there. As $K_\perp$ increases, the width of the emission region $\sqrt{\langle x^2\rangle - \langle x\rangle^2}$ decreases, because it gets more and more strongly pushed towards the edge (see Fig. 5.1, top right panel).

In y-direction (i.e. perpendicular to $\vec{K}_\perp$), the emission zone looks quite different: $\langle y\rangle$ vanishes for all $K_\perp$ due to reflection symmetry with respect to the x-axis. At $K_\perp = 0$ we have $\langle y^2\rangle(K_\perp = 0) = \langle x^2\rangle(K_\perp = 0)$ due to the azimuthal symmetry of the reaction zone in central collisions which is only broken by the direction of $\vec{K}_\perp$ if $K_\perp \neq 0$. As $K_\perp$ increases, $\langle y^2\rangle$ decreases similarly to $\sqrt{\langle x^2\rangle - \langle x\rangle^2}$, but not quite as strongly. This reflects the crescent shape of the emission region in Fig. 5.1 (top right panel), which is clearly wider in y than in x-direction.

For the longitudinal coordinate, $\langle z\rangle$ vanishes due to reflection symmetry around $z = 0$ if $y_K = 0$ ($K_l = 0$), see also Figure 5.2. As we have already discussed along the lines of this figure, it also explains why the longitudinal width $\langle z^2\rangle^{1/2}$ turns out so large, reaching up to 20 fm for $K_\perp$=0. Particles with low transverse momentum are frozen out rather late, when longitudinal velocity gradients are small. Therefore regions of large z still contribute a significant amount of particles with vanishing longitudinal momentum as the random thermal motion can cancel the

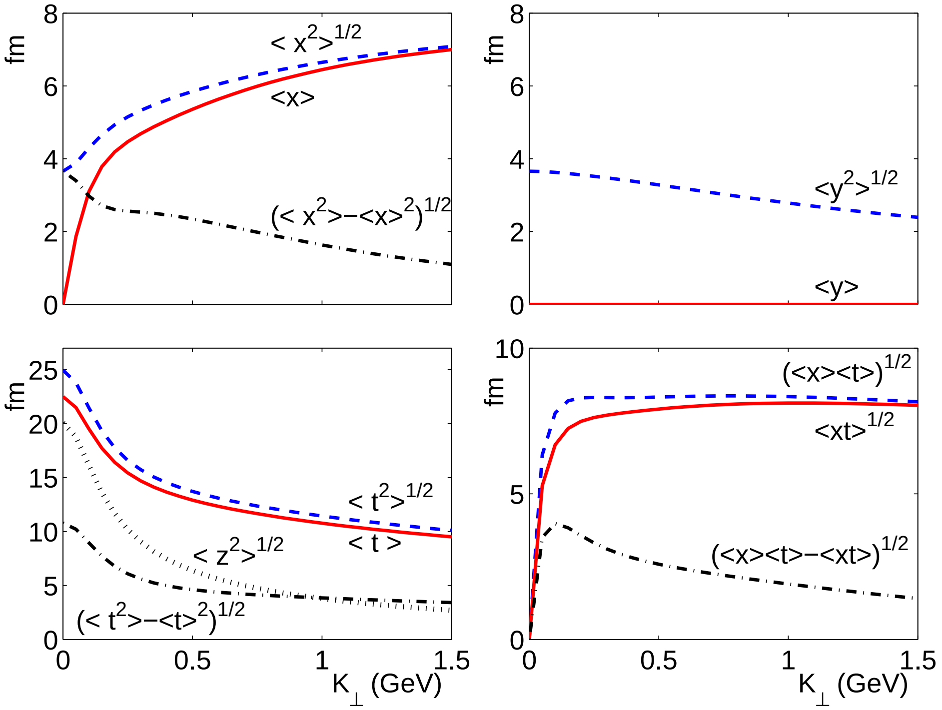

Figure 5.3: Average emission points and correlation lengths for RHIC 1 collisions for particles with $K_l = 0$ ($y_K = 0$) (using the source function also considered for Figures 5.1 and 5.2). The top row shows the average emission points and widths of emission regions for the transverse coordinates (x, y). The bottom row contains longitudinal and time averages and correlations. Note that at $y_K = 0$, $\langle z\rangle = 0$ due to symmetry. Similarly, $\langle y\rangle = 0$ if $\vec{K}_\perp \parallel \vec{e}_x$, due to reflection symmetry with respect to the (x, z)–plane.

collective longitudinal motion. The same discussion applies for the emission time duration which is in turn reflected in $(\langle t^2\rangle - \langle t\rangle^2)^{1/2}$. Even though at $z = 0$ ($\eta = 0$), the system has decoupled completely after $\tau_{\rm dec} \approx 16.5$ fm the average emission time reaches up to 22 fm/c for $K_\perp = 0$ (lower left panel of Fig. 5.3). The x-t-cross terms in the lower right panel of Figure 5.3 will become of interest in the next sections.

5.3 HBT RADII FROM CENTRAL COLLISIONS

Experimentally, the geometry of the collision region is accessible via two-particle correlations. Due to the statistical properties of the particles, they tend to cluster together in phase-space (Bosons) or avoid each other in phase-space (Fermions). Measuring this correlation by an enhancement of particles (in the following we focus on pions, i.e. Bosons), which lie close in momentum space thus allows to trace back the size in coordinate space from where the particles were emitted. Experimentally, this is accessible via the two-particle correlation function, which is obtained in terms of the single particle spectra EdN/d^3p and the two-particle coincidence distribution $E_1E_2dN/d^3p_1d^3p_2$ (which are normalized to the average number of emitted particles $\langle N\rangle$ and number of particle pairs $\langle N(N+1)\rangle$ respectively [131]) ,

$$C(\mathbf{p}_1,\mathbf{p}_2) = \left(\frac{dN}{d^3p_1\,d^3p_2}\right) \Big/ \left(\frac{dN}{d^3p_1}\cdot\frac{dN}{d^3p_2}\right) . \tag{5.7}$$

If there is no correlation between the emitted particles, i.e. if there are no quantum statistical effects, as happens for unlike particles or particles with large separation in phase-space, the correlator is identical to 1. Due to the clustering in phase-space however one finds an enhancement for particles lying close in momentum space, i.e. $\mathbf{p}_1 \approx \mathbf{p}_2$. The relative momentum difference of the corresponding on-shell four-momenta is denoted by $q = p_1 - p_2$, the average of the two four-momenta is $K = (p_1 + p_2)/2$ (the particle pair momentum). These four-vectors then fulfill the *mass-shell constraint* (or *orthogonality relation*)

$$K_\mu q^\mu = 0\,. \tag{5.8}$$

As the final state particles must be on-shell, the vectors K and q are off-shell.

The connection of the correlator to the source function [110] is straightforward if one assumes chaotic emission from the source. It is given by (see [59, 131] for detailed reviews)

$$C(\mathbf{p}_1,\mathbf{p}_2) = C(q,K) = 1 + \frac{|\int d^4x\,S(x,\,K)\,e^{iq\cdot x}|^2}{\int d^4x\,S(x,\,K+q/2)\int d^4y\,S(y,\,K-q/2)}\,. \tag{5.9}$$

In heavy ion collisions the correlations appear only around very small values of q relative to K which validates an on-shell ($K_0 \approx \sqrt{m^2+\mathbf{K}^2}$) and smoothness approximation ($S(x,K+q/2) \approx S(x,K-q/2) \approx S(x,K)$) [98], leading to the simpler connection

$$C(\mathbf{q},\mathbf{K}) \approx 1 + \left|\frac{\int d^4x\,S(x,\,K)\,e^{iq\cdot x}}{\int d^4x\,S(x,\,K)}\right|^2 . \tag{5.10}$$

This is usually parameterized by a Gaussian function in relative momentum space

$$C(\mathbf{q},\mathbf{K}) = 1 + e^{-q_\mu q_\nu\langle\tilde{x}^\mu\tilde{x}^\nu\rangle(K)} \tag{5.11}$$

where

$$\tilde{x}^\mu = x^\mu - \langle x^\mu \rangle(K) \tag{5.12}$$

and the averages are to be taken over the source function just as defined in Eq. (5.6). Because of the orthogonality constraint, Eq. (5.8), not all of the four components of q are independent, but we can rather eliminate q_0 via

$$q_0 = \mathbf{q} \cdot \frac{\mathbf{K}}{K_0}\,. \tag{5.13}$$

For the moment we turn our attention to central collisions and define a convenient coordinate-system for our purposes (the 'out-side-long-system'). The 'long'-axis points in the beam direction, the 'out'-axis is defined by the transverse component of the particle pair momentum, and the 'side'-axis is orthogonal to both, such that we have for the particle pair momentum $\mathbf{K} = (K_\perp,\, 0,\, K_l) = K_0(\beta_\perp,\, 0,\, \beta_l)$, where we have introduced $\beta_\perp$ and β_l as the velocity components of the particle pair. Exploiting the reflection symmetry around the side axis for central collisions, the parametrization of Equ. (5.11) becomes [38]

$$C(\mathbf{q}, \mathbf{K}) = 1 + e^{-R^2_{\mathrm{side}} q^2_{\mathrm{side}} - R^2_{\mathrm{out}} q^2_{\mathrm{out}} - R^2_{\mathrm{long}} q^2_{\mathrm{long}} - 2R^2_{\mathrm{ol}} q_{\mathrm{out}} q_{\mathrm{long}}}\,, \tag{5.14}$$

where we have introduced the so-called HBT radii (from Hanbury-Brown and Twiss [57]) which are given by [38]

$$\begin{aligned}
R^2_{\mathrm{side}}(K) &= \langle\, \tilde{y}^2 \,\rangle\,, && (5.15)\\
R^2_{\mathrm{out}}(K) &= \langle\, (\tilde{x} - \beta_\perp \tilde{t})^2 \,\rangle\,, && (5.16)\\
R^2_{\mathrm{long}}(K) &= \langle\, (\tilde{z} - \beta_l \tilde{t})^2 \,\rangle\,, && (5.17)\\
R^2_{\mathrm{ol}}(K) &= \langle\, (\tilde{x} - \beta_\perp \tilde{t})(\tilde{z} - \beta_l \tilde{t}) \,\rangle\,. && (5.18)
\end{aligned}$$

Again, we devote our interest to observables with rapidity $y = 0$, which implies $K_l = 0$ and $\beta_l = 0$. This leads to an additional symmetry with respect to the long-axis (z-axis), bringing R_{ol} to vanish identically.

What remains is then only a combination of the correlation lengths which we have evaluated in the previous section, and we arrive at ($\mathrm{Var}(f) = \langle\, f^2 \rangle - \langle\, f\,\rangle^2$ and $\mathrm{Var}(f, g) = \langle\, f\, g \,\rangle - \langle\, f\,\rangle \langle\, g\,\rangle$)

$$\begin{aligned}
R^2_{\mathrm{side}}(K_\perp) &= \mathrm{Var}(y), && (5.19)\\
R^2_{\mathrm{out}}(K_\perp) &= \mathrm{Var}(x) + \beta^2_\perp \mathrm{Var}(t) - 2\,\beta_\perp \mathrm{Var}(x, t)\,, && (5.20)\\
R^2_{\mathrm{long}}(K_\perp) &= \mathrm{Var}(z)\,. && (5.21)
\end{aligned}$$

The HBT radii measure the spatial widths of the emission regions, which are often referred to as the regions of *homogeneity* [114]. The sidewards radius measures only geometrical aspects of the system whereas, due to the mass-shell constraint (Eq. 5.8), the outward radius includes effects of the emission duration Var(t). Eqs. (5.19, 5.20) show that even though R_{out} is strongly influenced by the emission duration Var(t), the ratio $R_{\mathrm{out}}/R_{\mathrm{side}}$ is not a direct measure of the emission duration, and that in fact the latter can not be unambiguously extracted from the HBT radii. However, within a given source model (e.g. our hydrodynamical source), Eqs. (5.19 - 5.21) show how the spatial and temporal features of the source affect the HBT radii and this allows for a detailed understanding of the origins of the observed discrepancies with the data below.

Within this formalism, the HBT radii can now be derived by a straightforward combination of the correlation lengths of Section 5.2. The results for central RHIC 1 collisions are shown in Figure 5.4 together with experimental data from STAR [6] and PHENIX [5]. In addition to the results from 'traditional' hydrodynamic results (black solid lines), other graphs are displayed which will be discussed in the next subsection. We observe serious discrepancies between the experimental data

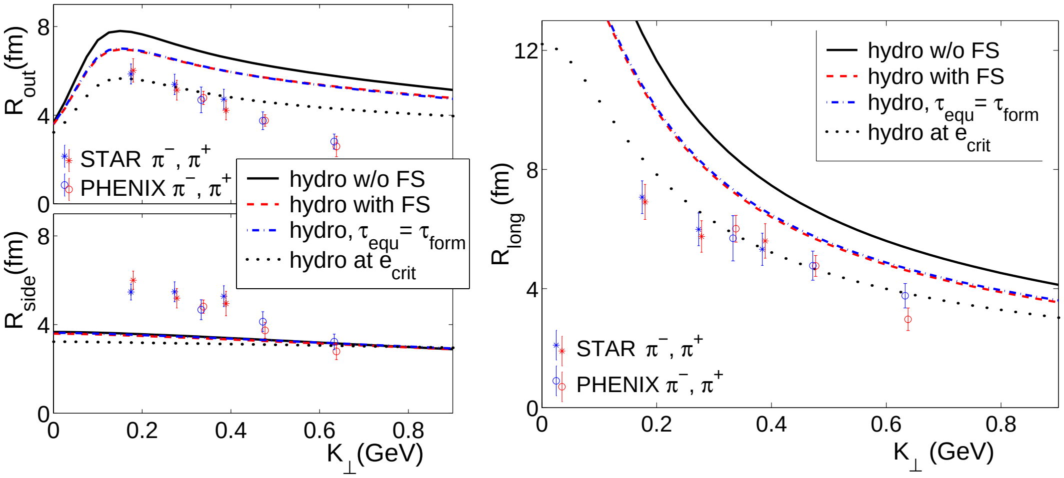

Figure 5.4: HBT radii from the hydrodynamic freeze-out hypersurface in comparison to experimental data [6, 5]. Also shown are possible effects of a preequilibrium dynamical scenario (see Section 5.4.1) and results for generation of the HBT radii at hadronization ($e_{\mathrm{dec}} = e_{\mathrm{crit}}$).

and hydrodynamic calculations. Even though we found that momentum-space observables show the strong signals expected from a hydrodynamic evolution, we conclude that the geometry in coordinate space is not well captured in this model description. We see that the hydrodynamic calculations underestimate the sidewards radius R_{side} by 30-40 %. The data indicate that the width of the emission region $\langle \tilde{y} \rangle$ (measured orthogonal to the direction of the particle pair momentum) is larger in the actual reaction and the crescent shown in the top right panel of Figure 5.1 must actually be larger, which can only be achieved if the system expanded to larger radii before decoupling. On the other hand, we have already seen that the longitudinal radius R_{long} is related to the mean emission time: If the system decouples late, the longitudinal flow velocity gradient is small and R_{long} comes out big, due to the larger the width of the emitting source in z-direction. Furthermore, particle emission from regions of large z happens late due to the time dilation effects in transverse planes traveling along the z-direction. This causes a large emission time duration $\mathrm{Var}(t)$ (left panel of Fig. 5.2), which contributes to R_{out}, rendering it larger than the data by $\sim 20\%$. Altogether this indicates that the system explodes even more violently than in the hydrodynamic prescription: The data suggest that the system reaches larger radial expansions in a shorter time - an observation which continues to puzzle the entire heavy ion community. Significant effort is now being put into the resolution of this issue.[1] In the following we discuss the discrepancy and possible resolutions from the viewpoint of the hydrodynamic expansion scenario.

5.4 Failure of HBT predictions

We continue the discussion of the unexpected experimental results on R_{out}, R_{side} and R_{long}. In particular we investigate the idealizations of the hydrodynamic prescription and their influence on the dynamical evolution and particle freeze-out.

Some of the ideas outlined in this section are very speculative and are simply meant to discuss extreme possibilities of dynamical scenarios that would drive the system to larger spatial extensions and induce earlier freeze-out. As we have seen before, this might provide a cure for the observed discrepancies with the measured HBT parameters. However, to arrive at a conclusive picture one has to ensure that the other observables, in particular the transverse momentum spectra and elliptic flow in non-central collisions, are still in agreement with the experimental data and the hydrodynamic limit.

---

[1] The most recent manifestation of the interest generated by this puzzle is the INT/RHIC Winter Workshop 2002 on "Correlations and Fluctuations in Heavy Ion Collisions at RHIC" (RWW02), January 4-6, 2002, Institute for Nuclear Theory, Seattle, Washington.

5.4.1 PREEQUILIBRIUM DYNAMICS

Traditionally, hydrodynamic calculations are initialized after a certain equilibration time τ_{equ}, which is a free parameter to be determined from the observed single particle spectra. Particle formation in the multiparticle wave-function of the initial state of the collision is estimated to happen at a time scale corresponding to the inverse of the saturation momentum, which allows the produced partons to geometrically cover up the overlap region of the two initial nuclei in the transverse plane. With $\tau_{\text{form}} = 1/p_{\text{sat}}$ one arrives at formation times of $\tau_{\text{form}} \sim 0.2$ fm/c at RHIC [47]. In the short timespan $\Delta\tau$ between formation and equilibration, the partons are assumed to undergo sufficient collisions among each other that local thermal equilibrium is established and pressure and pressure gradients are generated. Then, at τ_{equ} the system is assumed to behave fully hydrodynamically. Subsequently, transverse flow fields develop as a result of the transverse pressure gradients, and the evolution is fully determined by the conservation laws and the equation of state as described in chapter 2. In the usual hydrodynamic approach, as described up to now, the pressure gradients are switched on suddenly at τ_{equ}, and no collective transverse flow dynamics is generated before that point. This is clearly an approximation at best. Given the problems with the HBT radii and our diagnosis that this may point towards earlier freeze-out than given by hydro with standard initialization, we will now explore alterations to this approximation. Now we want to estimate the largely ignored influence of the preequilibrium stage by means of two extremes. In one case we can investigate the results from a completely free streaming partonic gas in the interval $\Delta\tau$ whereas the other extreme is given by a full hydrodynamic calculation already starting at formation time.

To understand how free-streaming can lead to a correlation of coordinate and momentum-space, imagine an ensemble of massless particles flying around in random directions inside a confining sphere of radius R_0. If at a certain time τ, the confining hull is taken away, the particles will leave their initial confining volume and stream away in random directions. After a certain time-span $\Delta\tau$ a few particles will have traveled to radial distances $\approx R_0 + \Delta\tau$ - if they were traveling radially outwards and started their journey from a position close to the wall of the confining sphere. In this way, a distinct profile of average velocities develops at radial distances from $R_0 - \Delta\tau$ to $R_0 + \Delta\tau$. This distribution of average velocities is calculated analytically in Appendix C.2 after the formalism for the calculation is presented in Appendix C.1. Appreciable flow fields are also obtained if the initial density distribution is not a box-profile but rather a smooth field given by the density of wounded nucleons and/or binary collisions as in our initialization (see Appendix C.1).

Whereas this scenario leads to an organization of the initially random velocities of the constituents and therefore global velocity fields, the full hydro scenario builds up early radial flow velocities from pressure. In both cases we will have finite radial flow velocities already at equilibration time, in contrast to traditional hydrodynamic calculations, which assume all transverse flow to be built up only after thermalization. The radial flow velocities from these scenarios are appreciable already after $\Delta\tau = \tau_{\text{equ}} - \tau_{\text{form}} = 0.4$ fm/c, reaching up to 0.4 c at the edge of the system, see Figure C.1.

The ultimate observables of the simulation are still the particle spectra. Therefore, due to stronger transverse flow in these calculations, we have to employ higher freeze-out temperatures in order to keep the slope of the particle spectra as observed. For both 'preequilibrium' extremes, we find that $T_{\text{dec}} = 138$ MeV leads to adequate fits to the φ_p-averaged single particle spectra as in Figure 2.10 (we have not checked the influence on v_2 of these modified initial conditions). Stronger transverse flow also leads to a faster inflation of the system, eventually producing larger transverse extensions than the traditional calculations. The higher freeze-out temperatures however work against this effect, leading to a maximum inflation which is about the same as in the traditional method. However the system's lifetime is reduced by about 20 %. Figure 5.5 shows the freeze-out hypersurface of the system under the various circumstances. It is described as the time evolution (vertical axis) of the radial distance of the freeze-out temperature (along the horizontal axis). The solid line is the result of the traditional calculation with freeze-out temperature $T_{\text{dec}} = 130$ MeV, which was also included in the lower row of Figure 5.1. At early times, this solution shows a rather large reduction of the initial extension due to the evaporation of the soft rim of the initial energy distribution, which is proportional to the density of the wounded nucleons and binary collisions (Section 2.1). Including velocity fields from a preequilibrium stage leads to an immediate push from the hot interior core, reducing the evaporation effect and driving the system outwards at earlier times. Note that the effect is very much the same, whether the dynamics between τ_{form} and τ_{equ} is generated by free streaming or by hydrodynamics! The two solutions for a preequilibrium time of $\Delta\tau$ are almost indistinguishable. Figure C.1 reveals, that the radial flow velocity fields at τ_{equ} are very similar in both cases. Marked differences appear only in the region where the hydrodynamic evolution is governed by the mixed phase, and collective flow velocities cannot develop hydrodynamically due to the vanishing pressure gradients in the mixed phase. In the main part of the fireball volume, the central plasma core, the radial dependence of the flow velocity is very similar in both cases. The main difference is that in non-central collisions, the free-streaming dynamics does not create any elliptic flow until τ_{equ} and then jumps to a non-zero value as a result of the matching

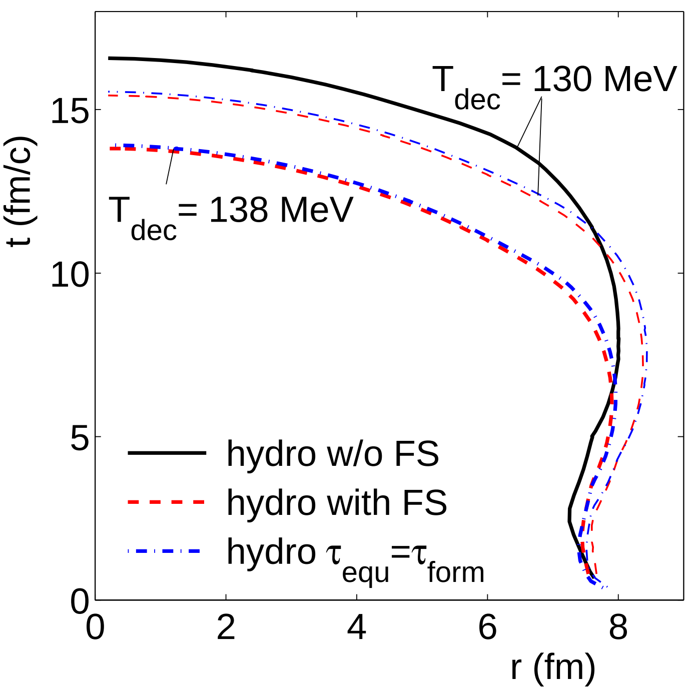

Figure 5.5: Freeze-out hypersurfaces displayed as $\tau_f(r)$ for central RHIC 1 collisions. The solid line shows the solution of the traditional calculation, the dashed and dashed-dotted line are for preequilibrium scenarios including free streaming from $\tau_{\rm form} = 0.2$ fm/c to $\tau_{\rm equ} = 0.6$ fm/c or an early equilibration time. The calculations with the larger decoupling temperatures lead to particle spectra, that fit again the experimental data.

of the kinetic energy momentum tensor to a hydrodynamic form. In contrast, the purely hydrodynamic evolution begins to build up momentum anisotropy at $\tau_{\rm form}$. The resulting momentum anisotropy at equilibration is very similar in both cases ($\epsilon_p(\tau_{\rm equ}) \approx 0.004$).

The resulting HBT radii calculated from the freeze-out hypersurface of the calculations including such a preequilibrium scenario are included in Figure 5.4 (again, as in Figure 5.5 the dashed line represents the results with the free-streaming period, the dashed-dotted the early hydrodynamic scenario, $T_{\rm dec} = 138$ MeV for both). The sidewards radius is not largely influenced by the new considerations – it goes slightly down, as the system still does not reach larger spatial extensions and the maximum radius of the system is even a little smaller, because of the required higher freeze-out temperature. The outwards and sidewards radii decrease and move towards the data. As discussed in the previous sections, this results from the shorter system lifetimes and emission durations, which are caused by the initial dynamics of the system. Altogether we are still a considerable distance away from the data, and it appears unlikely that transverse collective dynamics before $\tau_{\rm equ}$ can resolve the remaining discrepancies. For those we still have to look elsewhere.

5.4.2 Non-ideal effects

In our calculations we have implemented in the initial conditions a strong longitudinal dynamical expansion according to a Bjorken flow field $v_z = z/t$, which seems to be justified by experimental observables and numerical calculations (see Section 2.2.3).

Such a strongly inhomogeneous velocity field could lead to a decoupling of the longitudinal and transverse dynamics, as it is not obvious that a real system with non-ideal effects, which shows some 'stickiness' or viscosity, can follow up the strongly varying velocity fields and accelerations. It could therefore react different on pressure gradients in directions with strong flow than orthogonal to it. In dissipative hydrodynamics, this is described by adding a viscosity term $\tau^{\mu\nu}$ to the energy momentum tensor [82]:

$$T^{\mu\nu} = (e+P)u^\mu u^\nu - Pg^{\mu\nu} + \tau^{\mu\nu}. \tag{5.22}$$

Shear viscosity effects, which arise from an anisotropic flow fields are described in terms of the shear-tensor [82]

$$\tau^{\mu\nu} = -\eta\,(g^{\mu\gamma} - u^\mu u^\gamma)\left(\partial_\delta u_\gamma + \partial_\gamma u_\delta + \frac{2}{3}\,g_{\gamma\delta}\,\partial_\alpha u^\alpha\right)(g^{\delta\nu} - u^\delta u^\nu)\,, \tag{5.23}$$

where the shear viscosity η determines the strength of this correction. One easily finds that for a longitudinal Bjorken flow field $u^\mu = \gamma\,(1,0,0,z/t)$ at $z=0$ this expression becomes $\tau^{\mu\nu} = \frac{2\eta}{3t}\,\mathrm{diag}\,(0,\,1,\,1,\,-2)$. Such a term would therefore effectively reduce the longitudinal pressure (as was also found in microscopic calculations [45]), but increase the transverse components of the energy momentum tensor, leading to larger radial flow and a more rapid transverse expansion, while less longitudinal work is done by the fluid. The viscosity tensor scales with $1/t$, which is a result of the longitudinal velocity gradient at initialization. Early in the expansion process its effect is more serious than in later stages, when the system gets more and more isotropic.

The stronger transverse expansion can also lead to larger system sizes upon freeze-out. Freeze-out however could occur earlier, due to stronger transverse cooling of the radial flow. As we have seen before, this would change the results of HBT parameters in the desired way, lowering the longitudinal and outward radius, while increasing the sidewards radius. How large this effect is remains to be seen from quantitative calculations which are currently under development [99]. That particle spectra and elliptic flow remain in agreement with the experimental data then needs to be confirmed.

5.4.3 Particle freeze-out

Particle freeze-out from a certain hypersurface of fixed temperature or energy density in the space-time fabric according to a Cooper-Frye prescription has a long tradition of intense arguments, which were already addressed in Section 2.3. It is obvious that a smooth transition from the hydrodynamic to the free-streaming stage via a hadronic cascade afterburner [21, 125, 126] is a theoretically preferable option. It has also been noted that a more realistic late rescattering stage leads to a larger spatial width of particle emission [116] and therefore a larger sidewards radius [116] as the data in fact suggest. However, it does not help with the problems with R_{long} and R_{out}: the time duration of the stage where hadrons experience their last interaction and therefore the outwards radius turn out much larger than in the pure hydrodynamic calculations and the experimental data [116]. Even though it intuitively appears to be correct to model the late hadronic stage by a hadronic cascade, it also leaves the experimental data largely unexplained. It seems to be a nontrivial problem to increase R_{side} while at the same time decreasing R_{out} and R_{long}.

It was also proposed [116] that particle correlations may not be created at the late freeze-out stage, but rather at hadronization. From the hydrodynamic point of view this would lead to shorter time durations, but to still smaller transverse extensions of the source. Figure 5.4 includes the corresponding results from our calculation with $e_{\text{dec}} = e_{\text{crit}}$. Even though the results for R_{out} and R_{long} fall right into the experimental errorbars, this does not really point towards a solution of the problem as the results for R_{side} are even worse than before, and only a simultaneous description of all three parameters can be accepted as a satisfactory result.

5.4.4 Sensitivity to the equation of state

A detailed account of the sensitivity of HBT correlations to the equation of state was given in [139]. The authors find that an equation of state which features a crossover rather than a strong first order phase transition leads to smaller outwards radii, but with results still $\sim 20\%$ above the experimental data. As we have discussed before, smaller R_{out} is a result of of earlier freeze-out which is here achieved by stronger transverse cooling in the absence of a confining shell of mixed-phase. Still, freeze-out in these calculations does not happen early enough to cure the emission-duration problem which was also discussed earlier, and the large longitudinal radii persist. The sidewards radius does not exhibit a strong sensitivity on the employed equation of state and is almost a factor 2 too small in all studied cases. Even in scenarios with a crossover in the equation of state, the $R_{\text{out}}/R_{\text{side}}$ ratio turns out too large by a factor of more than 2.

That a weak phase transition or a crossover leads to an improvement of the outward and longitudinal radius is expected, as it is just the mixed phase from a first order phase transition which stalls the evolution, and therefore leads to long lifetimes and the large numerical values of R_{out} and R_{side}. In fact it was just this argument that led to the prediction of large outward radii [103], as one expected a delay signal if the system expanded under the influence of an equation of state with a strong first order phase-transition, as it is suggested by lattice gauge theory [46, 95].

The flow data that were analyzed in the previous chapters clearly suggest that there really is a strong phase transition in the equation of state, and we are seeing first signs of it from *hadronic* observables. These observables indicate a 'latent heat' (change in energy density during the phase transition which does not necessarily have to be first order) of the transition between 0.8 and 1.6 GeV/fm^3 [124, 125]. The solution of the HBT riddle therefore lies most likely in a combination of the causes discussed above, which might all by themselves contribute with small effects. This however is the worst case scenario, as it would be difficult to disentangle the different contributions to the HBT radii. But no matter which of those effects might turn out to be the most important to cope with the discrepancies, the observation that flow anisotropies agree *quantitatively* with experimental results still holds. As we have seen in Section 2.5, the anisotropies are generated *early* and are rather independent of the freeze-out dynamics and its modeling. While we cannot claim to have a complete understanding of the break-up of the system, we still have strong arguments that it has evolved through a period with local thermal equilibration and strong transverse pressure gradients which were established quite early in the collision.

5.5 Azimuthally sensitive HBT

Although the hydrodynamic predictions for HBT radii do not quantitatively agree with the experimental results, their theoretical analysis is still helpful for a full understanding of the expansion stage. In particular it is interesting to see qualitatively if HBT radii from non-central collisions can be used to reveal the dynamics of the fireball in *coordinate-space*, and possibly show the turnover from an oval which is initially elongated in y-direction to one that is finally longer in x-direction, as discussed in Section 2.5. For non-central collisions, the HBT radii of Eqs. (5.15) become dependent on the azimuthal angle between the impact parameter and the angle of observation, $\Phi = \angle(\vec{b}, \vec{K}_\perp)$.

At the AGS, oscillations of the HBT radii with Φ have been observed in non-central collisions [88]. At such relatively low energies, the system does not develop as large transverse dynamics as it does at RHIC energies, and thus the observed oscillations are thought to reflect the spatial geometry of the initial overlap almond [87, 88]. First preliminary data from RHIC also show clear signs of such oscillations [101], apparently *in phase* with the AGS data. Within a purely geometric interpretation, this would again indicate emission from a source which is still elongated along the y-direction, contrary to what is suggested by the density contours at late proper times shown in Figs 2.13 and 2.14. We will see later in this section that these snapshots at constant proper time τ can be misleading with respect to the shape of the actual emission function. Due to the much stronger flow, the validity of a purely geometric interpretation needs to be studied before drawing conclusions.

Let us begin by discussing the relevant formalism [87, 130]. As in the preceding chapters, the impact parameter defines the x-axis of the coordinate system, and the y-axis is orthogonal to beam- (z-) axis and the impact parameter. The transverse component of the particle pair momentum $\mathbf{K} = K^0\boldsymbol{\beta}$ and the impact parameter span the angle $\Phi = \angle(\vec{K}_\perp, \vec{b})$. The direction of $\vec{K}_\perp$ defines the 'out' direction, the 'side' direction is in the transverse plane and orthogonal to $\vec{K}_\perp$. Then, as before, R_{out} and R_{side} will be defined to give measures for the width of the 'homogeneity region' in the direction of the transverse momentum and perpendicular to it. The 'long' direction is again given by the beam axis.

Within these definitions of coordinate systems, the spatial correlation tensor $S_{\mu\nu} = \langle \tilde{x}_\mu \tilde{x}_\nu \rangle$, which summarizes the different correlation lengths, is not only a function of the magnitude of the particle pair momentum $K_\perp$, but also of its direction Φ when evaluated in the $(x,\, y)$ system fixed by the impact parameter:

$$S_{\mu\nu}(K_\perp, K_l, \Phi;\, b) = \langle \tilde{x}_\mu \tilde{x}_\nu \rangle (K_\perp, K_l, \Phi;\, b)\,. \tag{5.24}$$

The evaluation of the HBT radii via the correlation lengths as given in Eqs. (5.15-5.18) is then performed after rotating the coordinate system form this system into the out-side system given by the direction of $\vec{K}_\perp$: $(x,\, y) \to (x_{\mathrm{out}},\, x_{\mathrm{side}})$. After this rotation, the six non-vanishing HBT radii (for six pairwise combinations of the out, side and long direction) are given by [130]

$$\begin{aligned} R^2_{\mathrm{side}}(\Phi) &= S_{11}\sin^2\Phi + S_{22}\cos^2\Phi - S_{12}\sin 2\Phi\,, & (5.25)\\ R^2_{\mathrm{out}}(\Phi) &= S_{11}\cos^2\Phi + S_{22}\sin^2\Phi + S_{12}\sin 2\Phi \\ &\quad - 2\beta_\perp(S_{01}\cos\Phi + S_{02}\sin\Phi) + \beta_\perp^2 S_{00}\,, & (5.26) \end{aligned}$$

$$\begin{aligned}
R^2_{\rm os}(\Phi) &= S_{12}\cos 2\Phi + \frac{1}{2}(S_{22}-S_{11})\sin 2\Phi \\
&\quad + \beta_\perp (S_{01}\sin\Phi - S_{02}\cos\Phi)\,, & (5.27)\\
R^2_{\rm long}(\Phi) &= S_{33} - 2\beta_l S_{03} + \beta_l^2 S_{00}\,, & (5.28)\\
R^2_{\rm ol}(\Phi) &= (S_{13}-\beta_l S_{01})\cos\Phi - \beta_\perp S_{03} \\
&\quad + (S_{23}-\beta_l S_{02})\sin\Phi + \beta_l\beta_\perp S_{00}\,, & (5.29)\\
R^2_{\rm sl}(\Phi) &= (S_{23}-\beta_l S_{02})\cos\Phi - (S_{13}-\beta_l S_{01})\sin\Phi\,. & (5.30)
\end{aligned}$$

The explicit Φ-dependence arising from the geometrical rotation is displayed through the cos and sin terms. The geometrical features of the expansion dynamics come into play through the implicit angular dependence of the correlation tensor components $S_{\mu\nu}$.

Exploiting the symmetries at midrapidity leads to vanishing off-diagonal components of the spatial correlation tensor except for S_{13} [87]. Longitudinal boost invariance (which forbids a tilt of the source such as the one observed at the AGS [87]), however, leads to $S_{13}\equiv 0$ and studying pairs with vanishing longitudinal momentum, $\beta_l = 0$, we are left with the evaluation of only four non-trivial radii

$$\begin{aligned}
R^2_{\rm side}(\Phi) &= S_{11}\sin^2\Phi + S_{22}\cos^2\Phi \\
&= \frac{1}{2}(S_{11}+S_{22}) - \frac{1}{2}(S_{11}-S_{22})\cos 2\Phi\,, & (5.31)\\
R^2_{\rm out}(\Phi) &= S_{11}\cos^2\Phi + S_{22}\sin^2\Phi + \beta_\perp^2 S_{00} \\
&= \frac{1}{2}(S_{11}+S_{22}) + \frac{1}{2}(S_{11}-S_{22})\cos 2\Phi + \beta_\perp^2 S_{00}\,, & (5.32)\\
R^2_{\rm os}(\Phi) &= \frac{1}{2}(S_{22}-S_{11})\sin 2\Phi\,, & (5.33)\\
R^2_{\rm long}(\Phi) &= S_{33}\,. & (5.34)
\end{aligned}$$

The angular dependence of these radii with the transverse pair-momentum as a parameter is displayed in the four panels of Figure 5.6. The initial conditions correspond to RHIC 1 collisions with an impact parameter of 7 fm. The sideward radius is seen to be largest if the source is observed in direction of the impact parameter ($\Phi = 0$) and smaller when observed orthogonally to it ($\Phi = 90°$). The opposite oscillatory behavior is observed for the outward radius. The homogeneity regions thus appear wider when observed from the direction of impact parameter and smaller when observed orthogonal to it. Furthermore they are thinner when observed in direction of $\vec{b}$ than orthogonal to it (see also Figs. 5.10 to 5.12, where we will explain how this comes about). $R_{\rm os}$ oscillates sinus-like, describing how the region of homogeneity in the transverse plane tilts relative to the direction of observation.

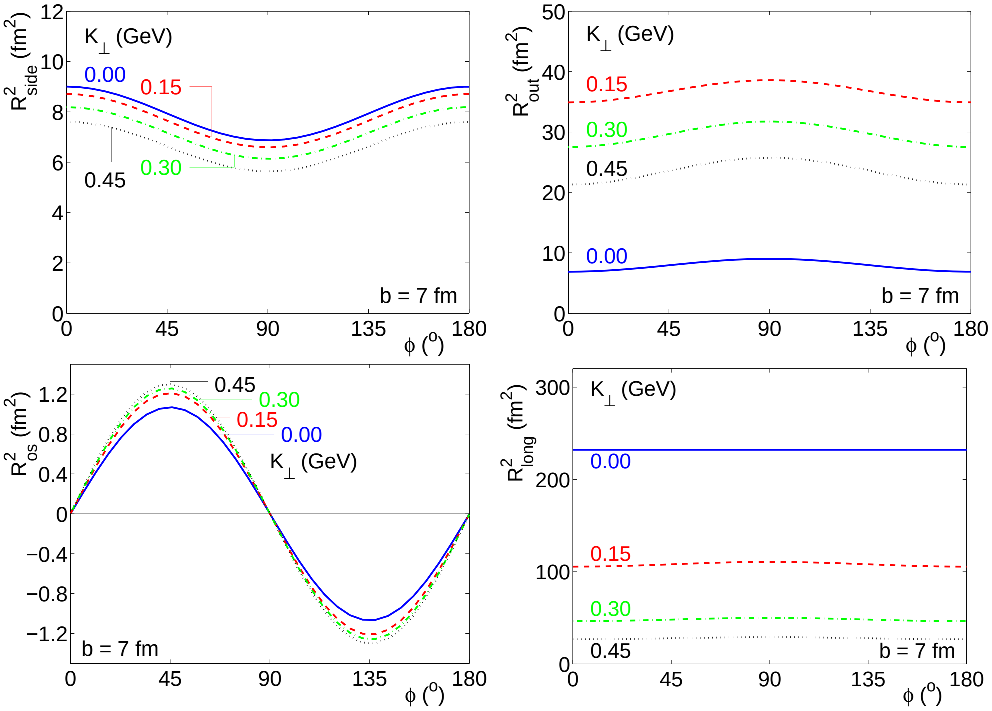

Figure 5.6: Azimuthal dependence of HBT radii for RHIC 1 collisions with impact parameter $b = 7$ fm for different transverse pair momenta $K_\perp$.

As before it is of interest to evaluate the HBT-radii and their azimuthal sensitivity not at the thermal decoupling energy density $e_{\mathrm{dec}} = 0.08$ GeV/fm^3 but also at the critical energy density ($e_{\mathrm{dec}} = e_{\mathrm{crit}}$) where hadrons leave the mixed phase, to understand the influence of the hadronic stage on the observation. This was also carried out in Section 5.4.3 and results from the hadronization surface of central collisions where shown in Fig. 5.4. There we saw that the outward and longitudinal radii from this earlier freeze-out agree better with the data, whereas the sideward radius gets even worse. Fig. 5.7 shows the angular dependencies at hadronization in strict analogy to Fig. 5.6. Obviously the HBT radii increase during the time from hadronization to freeze-out. The phase of the oscillation stays unchanged. However, the relative oscillation of the squared outward radius $\frac{\max(R^2_{\mathrm{out}}) - \min(R^2_{\mathrm{out}})}{\max(R^2_{\mathrm{out}}) + \min(R^2_{\mathrm{out}})}$ decreases from 8.9% to 5.0% between hadronization and decoupling. STAR has observed angular oscillations in R^2_{out} [101] with a relative oscillation of $\sim 8.7\%$. This is again better reproduced in our model if we assume that the HBT radii are fixed already at hadronization. For the crossterm R^2_{os} we

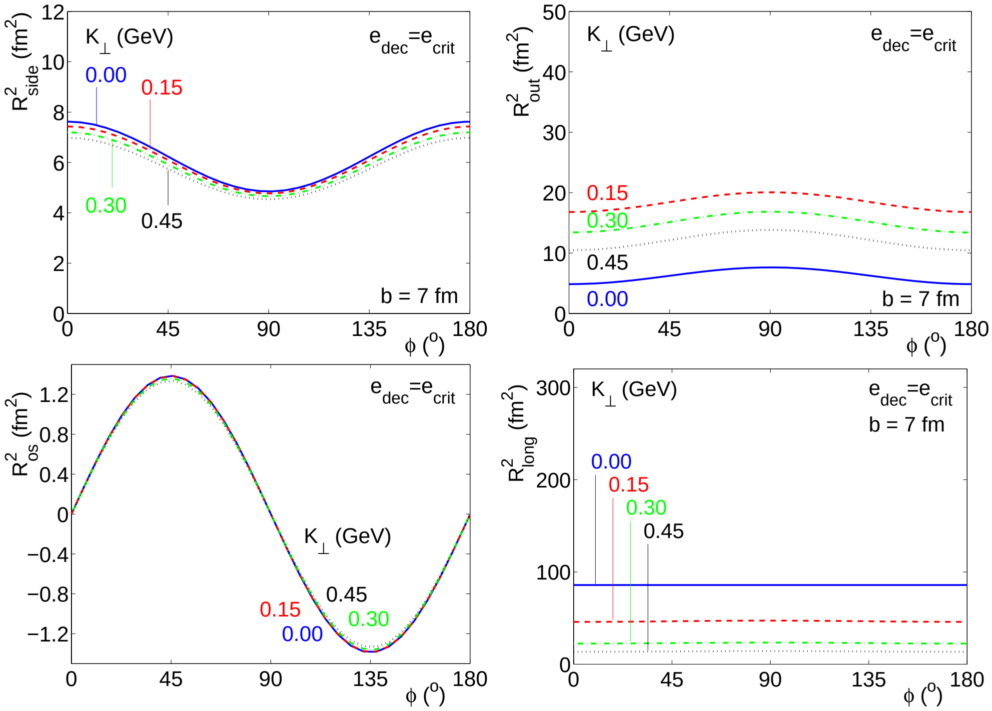

Figure 5.7: Azimuthal dependence of HBT radii for RHIC 1 collisions with impact parameter $b = 7$ fm for different transverse pair momenta $K_\perp$, evaluated at the transition from mixed phase to hadronic phase, $e_{\mathrm{dec}} = e_{\mathrm{crit}}$.

observe an amplitude of $\max(R^2_{\mathrm{os}}) \approx 1.3\ \mathrm{fm}^2$ at hadronization, decreasing somewhat (especially for smaller $K_\perp$) towards freeze-out. The values at hadronization are again in good agreement with preliminary STAR data [101]. The sign of the oscillations for R_{out}, R_{side} and R_{ol} in the data is correctly reproduced by our model. While at hadronization the hydrodynamic calculation can account for the average R^2_{out} and gives the proper magnitude of oscillation for R^2_{out} and R^2_{ol}, it gives much to small values for the sideward radius. At freeze-out all oscillations are too weak when compared to the data, and R_{long} and R_{out} are too large while R_{side} is still too small.

This oscillatory pattern is the same as observed at AGS energies [88], where flow effects are small. In the limit of vanishing flow, such a pattern is expected from purely geometrical reasons as the regions of homogeneity are centered around the origin for any momentum $\vec{K}_\perp$ and have the same geometry as the initial overlap region, i.e. they are elongated along the y-axis. At RHIC energies, transverse flow is large, and as we have found in the preceding chapters, particles with small transverse momenta are emitted later in the collision (Fig. 5.1) than particles with large $K_\perp$. At very late times, the relatively small part of the system that has not yet frozen out can reach negative spatial anisotropies, i.e. be oriented *in plane* (Fig. 2.12). On the other hand, particles with large transverse momenta are frozen out preferentially when the system has reached its largest expansion before matter transport from the fireball core cannot balance the strong transverse and longitudinal cooling any more and the radial extension of the fireball decreases (see again Fig. 5.1, lower right panel). In non-central collisions this happens already about 7.5 fm/c after equilibration, at a time where the source is still substantially deformed out of the reaction plane ($\epsilon_x > 0$).

As the source changes its shape through its time evolution and it is convoluted with the transverse momentum under investigation we study the shape of the total effective source in the transverse plane at midrapidity which we obtain by integrating the source function not only over time and the longitudinal coordinate but also over the transverse momentum. This gives the contribution $\frac{dN}{dxdydY}$ of a point (x, y) to the total multiplicity $\frac{dN}{dY}$ (in this section we denote the particle rapidity by Y and again investigate only emission of particles with $Y = 0$):

$$\frac{dN}{dxdydY} = \int K_\perp dK_\perp d\Phi \int_\Sigma dzdt\; S(x, y, z, t;\, \vec{K}_\perp)\,. \tag{5.35}$$

where Φ is the angle of $\vec{K}_\perp$ with respect to the reaction plane. Contours of this distribution are shown in Fig. 5.8. It is striking to observe that the majority of all emitted particles (not differentiating between different particle momenta), is emitted from the rim of the system at the system's largest expansion. The contributions from the interior, where low momentum particles are produced out of a region with potentially positive ϵ_x (see Fig. 5.10), is small and strongly suppressed in this representation due to the appearance of the factor of $K_\perp dK_\perp$ in Eq. (5.35).

In Figure 5.9 we show the analogous contour plots for the $\vec{K}_\perp$-integrated emission function at hadronization. We observe that there the spatial anisotropy is still larger than at thermal freeze-out. We further see that the contributions from the interior of the fireball are larger relative to the contributions from the rim. However here we always deal with a source with positive spatial anisotropy, irrespective of the particle momentum, as the time until hadronization does not allow the reduction of the spatial anisotropy of the freeze-out hypersurface to a value close to zero (Fig. 2.12).

After these general considerations on the shape of the *total* source, by which we mean the time and momentum integrated source-function, we now look again

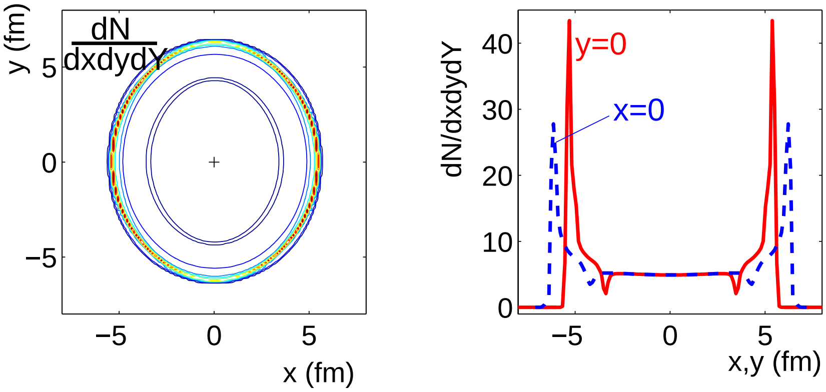

Figure 5.8: Contributions of the transverse coordinates to the total particle yield. The left panel shows contours in the transverse plane, the right plot gives cuts through the distribution at constant $y = 0$ as function of x (solid) and vice versa (dashed line).

at the emission of particles with certain fixed momenta and the shapes of the corresponding homogeneity regions.

The top left panel of Fig. 5.10 shows the contours of the source function in the transverse plane for $K_\perp = 0$, similar to the top row of Fig. 5.1, but now for a collision with non-zero impact parameter, $b = 7$ fm. One observes a complicated interplay of contours aligned in x and in y-direction, as a result of the unusual structures in the freeze-out hypersurface [123] which we discussed in Section 2.6. The other panels show the source functions for $K_\perp = 0.5$ GeV with three different orientations with respect to the impact parameter, namely $\Phi = 0$, $\pi/4$ and $\pi/2$. The gray line indicates the shape of the source at its largest expansion, about 7.5 fm/c after equilibration; this is essentially the same as the outermost contour of the total source (Fig. 5.8). One can clearly see that going from 0 to $\pi/2$ the thickness of the emission region (measured parallel to the vector $\vec{K}_\perp$) increases, whereas the width (measured orthogonal to $\vec{K}_\perp$) decreases (just as seen in the upper left panels of Figs. 5.6 and 5.7). Here it appears that the reason for the latter is the deformed geometry of the total source ($\epsilon_x > 0$), but later we will discuss how this can also arise from purely dynamical mechanisms.[2]

In Fig. 5.11 we repeat the investigations at hadronization. We now include

---

[2] The figure in the lower right panel shows a small 'island' along the y-axis where one of the contours is separated from the rest. It is a consequence of the phase transition and its vanishing pressure gradients which produce a flow field that does not necessarily increase monotonically with radius. Therefore also the source function is not necessarily a monotonic function of radius, but can show a more complicated behavior. This becomes even more apparent in Fig. 5.11.

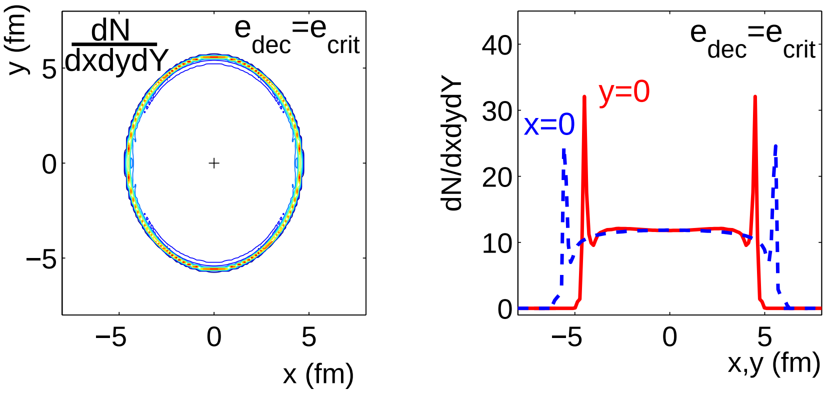

Figure 5.9: As Fig. 5.8, evaluated at hadronization, $e_{\mathrm{dec}} = e_{\mathrm{crit}}$.

as a gray line the maximum extension of the surface with $e_{\mathrm{dec}} = e_{\mathrm{crit}}$ (which happens at $\tau \approx 4.5$ fm$/c$), where most particles with large momenta are created. Because at hadronization the transverse flow is less strong than at freeze-out particle generation is not as strongly biased towards the edge as in Fig. 5.10. At first sight this might lead to a larger outward radius, but the outward radius also contains contributions from the emission time duration, which is much larger at freeze-out. The sidward extension reaches almost halfway around our confining hull. As this hull is now smaller than the hull given by the lower freeze-out energy density (Fig. 5.11), the sideward radius is slightly smaller. Again we see that the oscillations observed in our HBT radii Figs. 5.6 and 5.7 are apparently of geometrical origin. Because the geometric deformation at hadronization is larger at hadronization than at thermal freeze-out, the relative oscillation is larger in the former case.

We want to stress that this oscillatory pattern is not uniquely characterized by the effective shape of the source, but is strongly influenced by the flow pattern if the latter exhibits large anisotropies. If the flow gradients and anisotropies are large, one can even reach a stage where the oscillation pattern becomes completely decoupled from the geometric shape of the (momentum integrated) source and is determined entirely by the anisotropic flow.

Fig. 5.12 shows a cartoon of a source which is largely deformed in plane. (Such a total source could be generated at much higher beam energies (see the curve of extreme initial energy density in Fig. 2.12).) What we expect to happen at asymptotically high initial energy densities is the following: The anisotropic flow fields show a larger radial velocity gradient in x- than in y-direction. Therefore, the regions where particles of similar momentum (small q) are emitted are

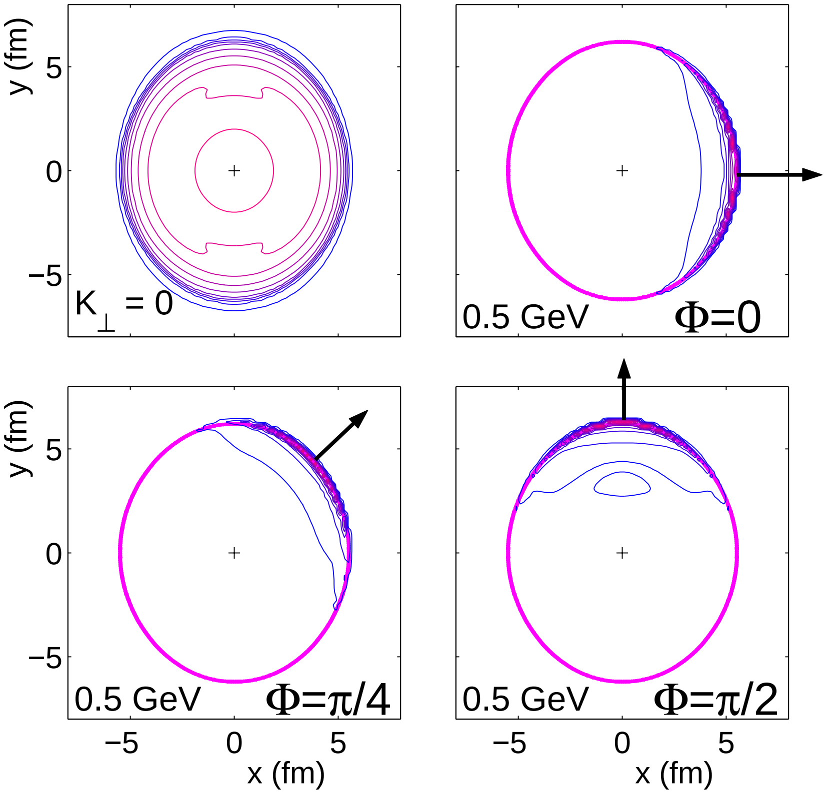

Figure 5.10: Source function of a non-central collision ($b = 7$ fm) for different transverse momenta. In the top left panel $K_\perp = 0$, for the others $K_\perp = 0.5$ GeV with different angles relative to the impact parameter. Top right: $\Phi = 0$, lower left: $\Phi = \pi/4$, lower right: $\Phi = \pi/2$

flatter if the particle pair momentum is in x-direction, and the *thickness* of this emission region Δx_{out} parallel to $\vec{K}_\perp$ is therefore smaller when observed from x-direction($\vec{K}_\perp \,||\, \vec{e}_x$), than from y-direction ($\vec{K}_\perp \,||\, \vec{e}_y$). On the other hand, the *width* of the emission region Δx_{side} (orthogonal to $\vec{K}_\perp$) where particles experience correlation effects is wider when seen from the x-direction, because the flow gradient in y-direction (at $y = 0$) is not as large as is the gradient in x-direction (at $x = 0$). This allows particles from larger spatial separations Δx_{side} to obtain similar momenta when emitted in x-direction. Both effects result from the different strength of the flow gradients in x- and y-direction, but at sufficiently large transverse flow become *independent of the spatial geometry of the source*, i.e. whether it is extended in or out of plane. Even in the limit $K_\perp = 0$ this homogeneity region, which is then centered at the origin can be oriented with its long axis orthogonal to the impact parameter, as the flow gradient is stronger in

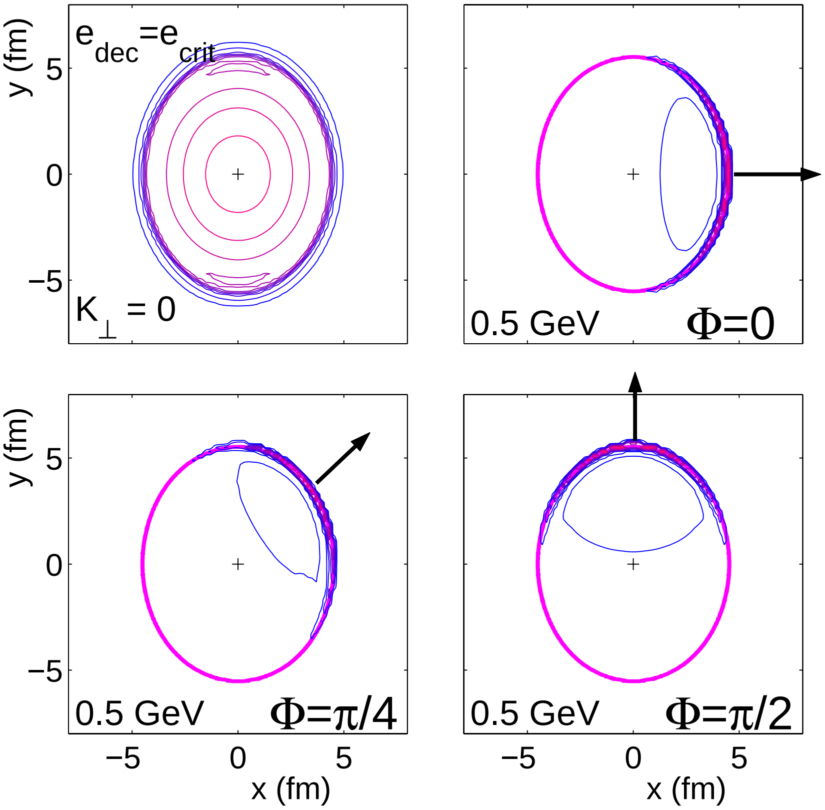

Figure 5.11: As Fig. 5.10 evaluated at hadronization, $e_{\rm dec} = e_{\rm crit}$.

this direction than in the y-direction – independently of the system's elongation in coordinate space! The geometry measured by investigating the azimuthal sensitivity of the HBT radii is the geometry of those homogeneity regions. Their shape is given through an interplay of anisotropies of the flow gradients as we have seen with the help of Fig. 5.12, and the geometry of the source, Figs. 5.10 and 5.11.

We conclude that although quantitatively the HBT radii are not under theoretical control, their dynamical origin is understood qualitatively, and the oscillatory pattern observed in the preliminary STAR data [101] is in agreement with the dynamical evolution suggested by the hydrodynamic picture. Due to strong transverse flow, the oscillation pattern does not give conclusive information on the freeze-out geometry of the system. We do see that *most* aspects of the measured HBT radii, including the sign and amplitude of their azimuthal oscillations can be reproduced by hydrodynamic model calculations, if we postulate (against our intuition) that the HBT radii are already fixed at hadronization. Then only

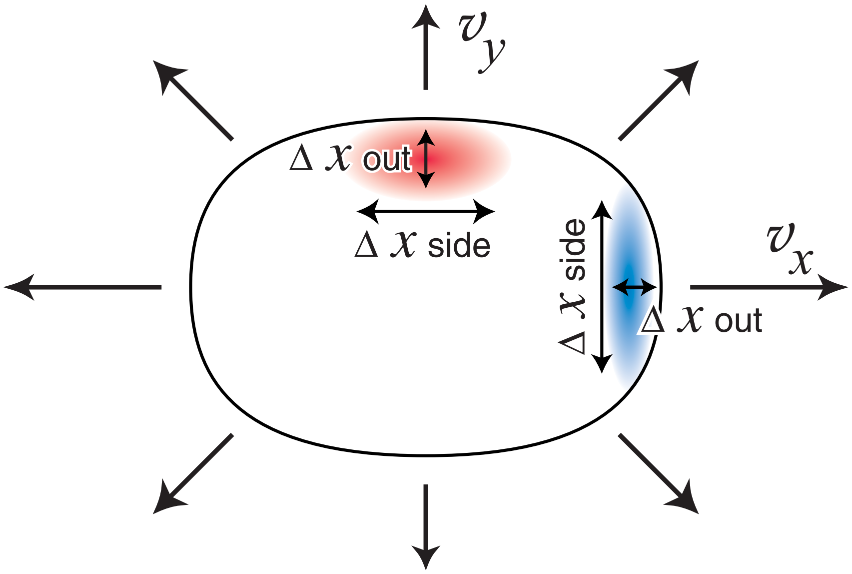

Figure 5.12: Schematic picture of a strongly deformed fireball in the transverse plane and two different regions of homogeneity corresponing to observation of particle pair momenta in plane and out of plane.

the magnitude of R_{side}, and its strong $K_\perp$ dependence, is severely underpredicted by the model. Unfortunately, while we clearly hear this message, we still don't understand what it wants to tell us about the freeze-out process.

6

Summary and conclusions

Within this work, the traditional hydrodynamic approach for the description of ultrarelativistic heavy-ion collisions was applied to study flow observables in the transverse plane with a special focus on the possibilities offered by non-central collisions. Encouraged by the large signal of anisotropic flow as first observed by the STAR collaboration [2], which was found to be in stunning agreement with predictions from hydrodynamic calculations [74, 75], I decided in this thesis to carry the model and its underlying philosophy to the limits, in order to study its range of applicability and establish where and how it begins to break down.

Therefore we assumed the validity of ideal hydrodynamics from equilibration to freeze-out at temperatures below the transition temperature predicted by lattice QCD calculations. To keep the number of unknown parameters as low as possible, we excluded all non-ideal, dissipative effects. The influence of the initial configuration on the dynamical evolution was investigated and it was found that a significant fraction (25 %) of the initial entropy density deposition has to originate from processes which scale with the number of binary collisions, in order to account for an increasing particle production per wounded nucleon pair with centrality, as it was observed in heavy ion experiments at collider energies [3, 24]. The four input parameters of the hydrodynamical calculation, the equilibration time τ_{equ}, the maximum entropy and net baryon density at equilibration s_{equ} and n_{equ}, and the decoupling temperature T_{dec}, were determined by fitting to particle spectra of identified pions and protons from central collisions *only.* For Au+Au collisions at $\sqrt{s_{\text{NN}}} = 130$ GeV we find the maximum entropy and baryon density at $s_{\text{equ}} = 95$ fm^{-3} and $n_{\text{equ}} = 0.3$ fm^{-3}, at an equilibration time $\tau_{\text{equ}} = 0.6$ fm$/c$. Thermal freeze-out occurs at $T_{\text{dec}} = 130$ MeV. The generalization of the initialization for the hydrodynamic calculations from central collisions to collisions with finite impact parameters then does not introduce any further parameters and the observables (apart from the centrality dependence of the multiplicity) are pure predictions derived from the hydrodynamic equations of motion and the underlying equation of state.

We first investigated global transverse observables from non-central collisions, i.e. observables with a possible azimuthal dependence integrated (or averaged) out. In particular we found good agreement with the transverse momentum spectra of pions, kaons and protons in a variety of centrality classes up to impact parameters of ~ 10 fm. The centrality dependencies of multiplicity, transverse momentum, and average transverse flow velocity were shown to be in qualitative and quantitative agreement with the experimental data. These observables indicate strong transverse expansion with average expansion velocities 10-20 % larger than those observed at the SPS. (This corresponds to an increase of $\gamma - 1$, which measures relativistic flow effects, by $\sim 30\%$.) However, already at lower beam energies, where local thermal equilibrium might not be fully achieved, transverse observables are known to be fitted well by thermodynamic models by choosing appropriate fit-parameters [44]. In that case, the thermodynamic model is a convenient parametrization of the particle spectra, but does not accurately describe the underlying dynamical expansion of the system. At RHIC, the latter seems to be realized for the first time.

Direct and unequivocal indication for the local equilibration and strong rescattering already in the earliest stages of the collision was found in observables which depend on the azimuthal angle of emission relative to the reaction plane. In particular we motivated elliptic flow, the anisotropic emission of particles in the transverse plane, and argued for its formation in the earliest stages and its saturation in later stages of the collision. A time delay in the equilibration would lead to a reduction of the initial eccentricity, which is to a fair degree proportional to the observed elliptic flow. The observed large signal thus tells us that local equilibration happens rapidly and pressure gradients drive the system apart collectively starting at very early times. We have shown excellent quantitative agreement of elliptic flow as a function of transverse momentum up to momenta of $p_{\mathrm{T}} \sim 2$ GeV, which accounts for more than 99% of the overall produced particles. For larger p_{T} the experimental data indicate insufficient thermalization and elliptic flow does not reach up to the hydrodynamic expectation value. Analyzing the centrality dependence of elliptic flow we found a gradual breakdown of the hydrodynamic model for collisions with impact parameters larger than $b \sim 7$ fm. Hydrodynamics predicts a characteristic mass dependence of elliptic flow as a function of the transverse momentum: Collective flow leads to stronger flattening of the transverse momentum spectra of heavier particles. Therefore elliptic flow as a function of transverse momentum develops only at larger p_{T} for heavier particles than for lighter ones. This mass dependence was found to be in good quantitative agreement with experimental observation. In addition, the mass systematics of elliptic flow gives a handle on the equation of state. Whereas the pion elliptic flow (and, due to the pion dominance, the elliptic flow of all charged hadrons) is rather insensitive on the equation of state, proton elliptic flow is strongly suppressed at low p_{T} in the presence of a strong phase transition. This is in fact observed in the experimental data of elliptic flow for identified particles. The phase transition also leads to a distinctive maximum in the excitation function of elliptic flow, as the growth of anisotropies stalls in the mixed phase where pressure gradients vanish. However a clear identification of this signal requires to have a locally equilibrated, initially spatially deformed system already at low SPS collision energies – a prerequisite that does not seem to be met in non-central Pb+Pb collisions, but may be reachable in central U+U collisions aligned in such a way that all nucleons in both nuclei interact.

Motivated by the full hydrodynamic studies, we have presented a generalization of the Siemens-Rasmussen blast-wave model [113] to allow for a simple and rapid parametrization of the anisotropic particle emission at low transverse momenta in terms of 3 parameters, the decoupling temperature, the maximum radial rapidity and an amplitude to describe an azimuthal angular modulation of the radial flow rapidity. This parametrization has been used in the analysis of experimental data [9], and we found that it gives a good description of the data with parameters for decoupling temperature, radial rapidity and rapidity modulation given as $T_{\mathrm{dec}} = 140$ MeV, $\rho_0 = 0.58$ and $\rho_a = 0.09$, quite consistent with the full hydrodynamic simulations.

From the consistency of the description of a large body of single-particle observables which are highly sensitive to the thermodynamic history of the system, we conclude that the initially created system undergoes an expansion according to the laws of ideal hydrodynamics. The time needed to reach local thermal equilibrium is less than one fm/c after the first partons collided, and temperatures and energy densities at this stage are far above the predicted transition values to the QCD plasma stage.

However, as was discussed in the last chapter, the observed HBT radii, and thus the freeze-out geometry of the collisions differ strongly from the hydrodynamic freeze-out hypersurface. From our current understanding and interpretation, the measured HBT radii indicate shorter particle emission durations and earlier freeze-out, together with a larger spatial extension of the particle emitting source. We have investigated the possibility of stronger dynamics due to preequilibrium effects, which went in the right direction but did not yield large enough modifications to give a satisfactory explanation of the HBT data. Nevertheless, we noted the importance of azimuthally sensitive HBT radii for a clarification of the freeze-out geometry in non-central collisions. The discrepancy in the freeze-out geometry does not invalidate our conclusion in favor of the hydrodynamic expansion stage, as the observables that lead to that conclusion are not sensitive to the late collision stages, in particular not to the details of the hydrodynamically employed freeze-out. This is especially true for elliptic flow, which is generated early in the collisions. Improvements of the freeze-out dynamics are currently being investigated by several groups, in particular by using models which switch to a hadronic rescattering stage after hadronization. Even though this seems to be a more consistent approach for the late rescattering stage of the dilute hadron gas, the HBT-radii from such freeze-out scenarios so far lead to similar discrepancies with the experimental data [116].

In addition to the freeze-out and HBT problem, the microscopic equilibration mechanisms which make the hydrodynamic model work are not accessible within our macroscopic model. Only truly microscopic models can offer explanations of the very short equilibration times. At the moment partonic transport models can explain the large flow observables only under assumptions of density or cross section parameters which are orders of magnitude larger than estimated from perturbative QCD. This presents an additional puzzle for the earliest stage of the collision – its resolution is likely to completely change our understanding of early QCD dynamics in relativistic heavy ion collisions.

We have presented evidence that a system of deconfined quarks and gluons in local thermodynamic equilibrium is produced in heavy-ion collisions at RHIC energies. Its expansion into the surrounding vacuum is well under theoretical control from the macroscopic point of view. Now we must set out to understand the microscopic mechanisms that lead to rapid thermalization, and the freeze-out of the particles from the fireball needs to be better investigated in order to reach a full understanding of the *complete* reaction dynamics of ultrarelativistic heavy ion collisions. Clearly, exciting physics lies ahead to be resolved with the aid of experiments at RHIC and LHC and the resolutions of the equilibration problem will not only be of interest to the nuclear science community, but on an even more fundamental level.

APPENDIX A

COORDINATES AND TRANSFORMATIONS

This appendix summarizes the different coordinates and coordinate systems that one encounters permanently when dealing with collisions at relativistic energies. Furthermore the details for the transformation of the equations of motion are presented, as well as the evaluation of the transverse momentum spectra in the coordinates of choice.

A.1 COORDINATE SPACE

A.1.1 CARTESIAN COORDINATES

Consider the collision of two reaction partners (elementary particles, hadrons or nuclei) in their center of momentum frame (see Figure 2.1). The direction of the momentum vectors of the collision partners define the z-axis of the coordinate system (also called the *beam axis*). The *transverse plane* is the plane orthogonal to the z-axis through $z = 0$ which is set by the center of momentum. This transverse plane is spanned by the x- and y-axis. In case the center of masses of the individual reaction partners do not fall onto the z-axis, the collision has a finite impact parameter b, which is given by the projection of the connection vector of the two center of masses onto the transverse plane. The x-axis is then chosen to coincide with this projection vector, and thus $\vec{b} = b\,\vec{e}_x$. This orthogonal coordinate system together with the time t spans a Minkowski-space with the invariant line element squared $ds^2 = g_{\mu\nu} dx^\mu dx^\nu = dt^2 - dx^2 - dy^2 - dz^2$ and the trivial metric

$$g_{\mu\nu} = \mathrm{diag}(1,\, -1,\, -1,\, -1)\,. \tag{A.1}$$

A.1.2 Rapidity coordinates

Due to the strongly forward peaked cross-sections in elementary particle collision and nuclear transparency in nuclear collisions, the final state dynamics is largely oriented along the beam axis, just as in the initial stage of the reaction. The secondary particles will then have large velocity components in the direction of the beam. Therefore, within the light-cone $z < t$ a transformation to longitudinal eigentime $\tau = \sqrt{t^2 - z^2}$ proves useful. The coordinate orthogonal to the longitudinal eigentime is the space-time rapidity $\eta = \frac{1}{2} \ln \frac{t+z}{t-z} = \mathrm{Artanh}\,(z/t)$. The $(x,\, y)$ coordinates are not affected by this transformation. The full set of equations and differentials for the transformation back and fro from Cartesian coordinates is given by

$$x^\mu = (t, x, y, z) \longrightarrow \bar{x}^m = (\tau, x, y, \eta)$$

$$\begin{aligned}
t &= \tau \cosh\eta & \tau &= \sqrt{t^2 - z^2} \\
z &= \tau \sinh\eta & \eta &= \mathrm{Artanh}\,(z/t) \\
dt &= d\tau \cosh\eta + d\eta\, \tau \sinh\eta & d\tau &= dt\, \cosh\eta - dz\, \sinh\eta \\
dz &= d\tau \sinh\eta + d\eta\, \tau \cosh\eta & d\eta &= \frac{dz}{\tau} \cosh\eta - \frac{d\tau}{\tau} \sinh\eta\,.
\end{aligned} \tag{A.2}$$

The metric in the rapidity coordinate system follows from the invariant line element in this coordinate system $ds^2 = g_{mn} dx^m dx^n = d\tau^2 - dx^2 - dy^2 - \tau^2 d\eta^2$ to be

$$g_{mn} = \mathrm{diag}(1,\, -1,\, -1,\, -\tau^2)\,. \tag{A.3}$$

Most practical use of the pseudorapidity coordinates is made by using the coordinates $(\tau,\, \eta)$ in the actual orthogonal Minkowski space, i.e. by writing $x^\mu = (\tau \cosh\eta,\, x,\, y,\, \tau \sinh\eta)$, but vectors in the rapidity coordinate system will be used extensively in the next subsection for the derivation of the equations of motion. There we will also need the Christoffel symbols of the rapidity space which are evaluated from the metric by

$$\Gamma^s_{ij} = \frac{1}{2} g^{ks} (g_{ik,j} + g_{jk,i} - g_{ij,k})\,, \tag{A.4}$$

where the lowercase comma and index denotes the derivative with respect to this coordinate. The only non-vanishing Christoffel symbols in this metric are

$$\Gamma^\eta_{\eta\tau} = \frac{1}{\tau}\,, \qquad \Gamma^\eta_{\tau\eta} = \frac{1}{\tau}\,, \qquad \Gamma^\tau_{\eta\eta} = \tau\,. \tag{A.5}$$

A.1.3 TRANSFORMATION OF THE EQUATIONS OF MOTION

As is argued in section 2.2.3, from the strong longitudinal dynamics in the earliest stages of the collision, one can expect to have a Hubble like longitudinal flow-field, i.e. $v_z = z/t = \tanh\eta$. Numerical calculations which take the longitudinal direction into account explicitly show, that this flow field persists throughout the evolution in a substantial region around midrapidity [119]. Analytically implementing such a longitudinal Bjorken flow field [27] into the four velocity renders it particularly simple in rapidity space (with $\gamma = dt/d\tau_{\text{proper}}$ the time dilation factor),

$$\begin{aligned}
\bar{u}^\tau &= \frac{d\tau}{d\tau_{\text{proper}}} = u^0\cosh\eta - u^3\sinh\eta = \gamma\,\frac{1}{\cosh\eta}\,,\\
\bar{u}^x &= u^1\,,\\
\bar{u}^y &= u^2\,,\\
\bar{u}^\eta &= \frac{d\eta}{d\tau_{\text{proper}}} = \frac{1}{\tau_{\text{proper}}}\left(u^3\cosh\eta - u^0\sinh\eta\right) = 0\,,
\end{aligned}$$

that is, there is no flow in the space time rapidity coordinate. Furthermore making extensive use of the theorem for the summation of hyperbolic functions, $\cosh^2\eta - \sinh^2\eta = 1$, this can be brought to the simple expression

$$\bar{u}^m = \bar{\gamma}\,(1, \bar{v}_x, \bar{v}_y, 0)\,. \tag{A.6}$$

where we introduced the abbreviations $\bar{v}_i := v_i\cosh\eta$, $(i = x, y)$, and $\bar{\gamma} := 1/\sqrt{1-\bar{v}_x^2-\bar{v}_y^2}$.

We now go ahead to write down the equations of motion Eq. (2.9) and (2.10) in this chosen coordinate system. In an arbitrary coordinate system, the equations of motion are still as simple as $T^{mn}{}_{;m} = 0$ and $j^m{}_{;m} = 0$, but now the derivatives are covariant derivatives (indicated by the semi-colon) which have to be taken according to special rules respecting the geometry of the chosen description of space.[1] For tensors of rank 2 it is given by $T^{ik}{}_{;p} = T^{ik}{}_{,p} + \Gamma^i_{pm}T^{mk} + \Gamma^k_{pm}T^{im}$ and for vectors $j^i{}_{;p} = j^i{}_{,p} + \Gamma^i_{pk}\,j^k$. Because of the simplicity of the energy momentum tensor $T^{mn} = (e+P)u^m u^n - g^{mn}P$ in the rapidity coordinate system where one of the components of the four-velocity vanishes, one of the equations decouples trivially from the others, and one quickly arrives at the equations

$$T^{\tau\tau}{}_{,\tau} + \left(\bar{v}_x T^{\tau\tau}\right)_{,x} + \left(\bar{v}_y T^{\tau\tau}\right)_{,y} = -\frac{1}{\tau}\left(T^{\tau\tau}+P\right) - (P\bar{v}_x)_{,x} - (P\bar{v}_y)_{,y}\,, \tag{A.7}$$

---

[1] see any book on general relativity or covariant tensor calculus

$$T^{\tau x}{}_{,\tau} + \left(\bar{v}_x T^{\tau x}\right)_{,x} + \left(\bar{v}_y T^{\tau x}\right)_{,y} = -P_{,x} - \frac{1}{\tau} T^{\tau x}\,, \tag{A.8}$$

$$T^{\tau y}{}_{,\tau} + \left(\bar{v}_x T^{\tau y}\right)_{,x} + \left(\bar{v}_y T^{\tau y}\right)_{,y} = -P_{,y} - \frac{1}{\tau} T^{\tau y}\,, \tag{A.9}$$

$$\frac{1}{\tau^2}\, P_{,\eta} = 0\,, \tag{A.10}$$

$$j^{\tau}{}_{,\tau} + (\bar{v}_x j^{\tau})_{,x} + (\bar{v}_y j^{\tau})_{,y} = -\frac{1}{\tau} j^{\tau}\,, \tag{A.11}$$

of which Eq. (A.10) indicates that there are also no pressure gradients along the rapidity coordinate.

Technically these equations are easier to solve (or to *evolve* in time) after multiplying them with τ and rewriting them as

$$\tilde{T}^{\tau\tau}{}_{,\tau} + \left(\bar{v}_{xs}\tilde{T}^{\tau\tau}\right)_{,x} + \left(\bar{v}_{ys}\tilde{T}^{\tau\tau}\right)_{,y} = -P\,, \tag{A.12}$$

$$\tilde{T}^{\tau x}{}_{,\tau} + \left(\bar{v}_x\tilde{T}^{\tau x}\right)_{,x} + \left(\bar{v}_y\tilde{T}^{\tau x}\right)_{,y} = -\tilde{P}_{,x}\,, \tag{A.13}$$

$$\tilde{T}^{\tau y}{}_{,\tau} + \left(\bar{v}_x\tilde{T}^{\tau y}\right)_{,x} + \left(\bar{v}_y\tilde{T}^{\tau y}\right)_{,y} = -\tilde{P}_{,y}\,, \tag{A.14}$$

$$\tilde{j}^{\tau}{}_{,\tau} + (\bar{v}_x\tilde{j}^{\tau})_{,x} + (\bar{v}_y\tilde{j}^{\tau})_{,y} = 0\,. \tag{A.15}$$

With $\tilde{j}^{\tau} := \tau j^{\tau}$, $\tilde{T}^{\tau i} := \tau T^{\tau i}$, $(i = \tau,\, x,\, y)$, and $\tilde{P} := \tau P$. Furthermore it is necessary to introduce velocities of energy flow, i.e.

$$\bar{v}_{is} = \frac{(e+P)\bar{\gamma}^2\bar{v}_i}{(e+P)\bar{\gamma}^2 - P} = \frac{T^{\tau i}}{T^{\tau\tau}}\,, \qquad i \in (x,\, y) \tag{A.16}$$

We solve these equations of motion using the SHASTA algorithm [30] together with an improved flux-correction [136] for multi-dimensional problems. The resulting algorithm is especially well suited to keep discontinuities under numerical control which might arise during the evolution. In the fireball simulations the mixed phase with vanishing pressure gradients necessitates this delicate treatment of shock-waves and discontinuities.

A.1.4 PARAMETRIZATION OF A BOOST INVARIANT SURFACE

Generally, a hypersurface in n dimensions is parameterized by $n-1$ parameters. Here we want to parameterize the four-dimensional freeze-out hypersurface in terms of the the transverse coordinates $(x,\, y)$ and the longitudinal rapidity η. Furthermore we make the Bjorken assumption that all processes happening at non-zero η are locally the same than as at $\eta = 0$ (Eq. (A.6) and Eq. (A.10)). In the rest frame at $\eta = 0$ this generates a longitudinal gamma factor $\gamma = \cosh\eta$. Thus if we know the freeze-out hypersurface in the transverse plane at $z = 0$, parameterized for example by $\tau_f(x,\, y)$, we can write down the freeze-out hypersurface in four dimensions as

$$\begin{aligned}\Sigma(x,\, y,\, \eta) &= \left(\Sigma^0(x,\, y,\, \eta),\, \Sigma^1(x,\, y,\, \eta),\, \Sigma^2(x,\, y,\, \eta),\, \Sigma^3(x,\, y,\, \eta)\right) = \\ &= \left(\tau_f(x,\, y)\cosh\eta,\, x,\, y,\, \tau_f(x,\, y)\sinh\eta\right). \end{aligned} \tag{A.17}$$

The normal vector on such a surface is given by (see e.g. [108])

$$d^3\sigma_\mu(x,\, y,\, \eta) = -\epsilon_{\mu\nu\lambda\rho}\, \Sigma^\nu{}_{,x}\, \Sigma^\lambda{}_{,y}\, \Sigma^\rho{}_{,\eta}\, dx dy d\eta\,, \tag{A.18}$$

with the totally antisymmetric tensor of fourth order

$$\epsilon^{\mu\nu\lambda\rho} = -\epsilon_{\mu\nu\lambda\rho} = \begin{cases} 1 & \text{for } (\mu,\, \nu,\, \lambda,\, \rho) \text{ even permutation of } (0,\, 1,\, 2,\, 3) \\ -1 & \text{for } (\mu,\, \nu,\, \lambda,\, \rho) \text{ odd permutation of } (0,\, 1,\, 2,\, 3) \\ 0 & \text{otherwise.} \end{cases} \tag{A.19}$$

Therefore the normal vector on the boost invariant surface (Eq. A.17) is given by

$$d^3\sigma_\mu = \left(\cosh\eta,\, -\frac{\partial\tau_f(x,\, y)}{\partial x},\, -\frac{\partial\tau_f(x,\, y)}{\partial y},\, -\sinh\eta\right)\, \tau_f(x,\, y)\, dx dy d\eta\,. \tag{A.20}$$

A.2 MOMENTUM SPACE

A.2.1 RAPIDITY AND TRANSVERSE MASS

Analogously to the definition of the space time rapidity $\eta = \frac{1}{2}\ln(t+z)/(t-z)$ one uses the same combination of the (0) and (3) component of the four momentum $p^\mu = (p^0,\, p^1,\, p^2,\, p^3) = (E,\, \vec{p})$ to define the rapidity of a particle (with $E = \sqrt{m^2 + \vec{p}^2}$ the energy of the particle with mass m),

$$y = \frac{1}{2}\ln\frac{E + p_z}{E - p_z} = \operatorname{Artanh}\frac{p_z}{E}\,. \tag{A.21}$$

Defining further

$$m_{\mathrm{T}} = \sqrt{E^2 - p_z^2} = \sqrt{m^2 + p_x^2 + p_y^2} = \sqrt{m^2 + p_{\mathrm{T}}^2}\,, \tag{A.22}$$

one has achieved a transformation $(E,\, p_z) \leftrightarrow (m_{\rm T},\, y)$ similar to the space-time transformation, yielding

$$p^\mu = (m_{\rm T}\cosh y,\, p_x,\, p_y,\, m_{\rm T}\sinh y)\,. \tag{A.23}$$

In this coordinate system, the invariant particle distribution becomes

$$E\,\frac{dN}{d^3p} = \frac{dN}{dydp_xdp_y} = \frac{dN}{dyp_{\rm T}dp_{\rm T}d\varphi_p}\,. \tag{A.24}$$

Note also, that $p_{\rm T}dp_{\rm T} = m_{\rm T}dm_{\rm T}$.

A.2.2 Evaluation of the momentum spectra

With the help of the longitudinal Bjorken flow field $v_z = z/t = \tanh\eta$, the four flow field can be written as $u^\mu = \gamma\,(\cosh\eta,\, v_x(x,\, y),\, v_y(x,\, y),\, \sinh\eta)$ (in Minkowski space) with $\gamma = 1/\sqrt{1 - v_x^2(x,\, y) - v_y^2(x,\, y)}$. Together with Eq. (A.23), one obtains from this

$$\begin{aligned} u^\mu p_\mu &= \gamma\,(m_{\rm T}\cosh(\eta - y) - v_xp_x - v_yp_y) & \text{(A.25)}\\ &= \gamma\,(m_{\rm T}\cosh(\eta - y) - \vec{v}_{\rm T}\cdot\vec{p}_{\rm T}) & \text{(A.26)}\\ . & & \text{(A.27)}\end{aligned}$$

Similarly, multiplying Eq. (A.23) with Eq. (A.20) yields

$$p^\mu d^3\sigma_\mu = \Big(m_{\rm T}\cosh(\eta - y) - \vec{p}_{\rm T}\cdot\vec{\nabla}_{\rm T}\,\tau_f(x,\, y)\Big)\,\tau_f(x,\, y)\,dxdyd\eta\,, \tag{A.28}$$

where we have introduced the transverse gradient operator $\vec{\nabla}_{\rm T} = (\partial/\partial x,\, \partial/\partial y)\,.$

This culminates in the evaluation of the particle spectra, Equation 2.24, which we present here in detail. As in [104], we use the geometrical series $\frac{1}{1-a} = \sum_{n=0}^{\infty} a^n$ (for $|a| < 1$) to expand the statistical distribution factor. Furthermore, we make use of the integral definition of the modified Bessel Functions (see for example [1]):

$$\mathrm{K}_\nu(z) = \int_0^\infty dt\cosh(\nu t)\,e^{-z\cosh t} \tag{A.29}$$

Then we obtain

$$\frac{dN}{dydp_xdp_y} = \frac{g}{(2\pi)^3}\int_\Sigma f(p^\mu u_\mu, x)p_\mu\,d^3\sigma^\mu =$$

$$\begin{aligned}
&= \frac{g}{(2\pi)^3}\int dx dy\, \tau_f(x,y)\int_{-\infty}^{\infty} d\eta\, \frac{m_{\mathrm{T}}\cosh(y-\eta)-\vec{p}_{\mathrm{T}}\cdot\vec{\nabla}_{\mathrm{T}}\,\tau_f(x,\,y)}{e^{\beta[\gamma(m_{\mathrm{T}}\cosh(\eta-y)-\vec{v}_{\mathrm{T}}\cdot\vec{p}_{\mathrm{T}})-\mu]}\pm 1} = \\
&= \frac{g}{(2\pi)^3}\int dx dy\, \tau_f(x,y)\sum_{n=1}^{\infty}(\mp 1)^{n+1}\int_{-\infty}^{\infty} d\eta\, e^{-n\,\beta[\gamma(m_{\mathrm{T}}\cosh(\eta-y)-\vec{v}_{\mathrm{T}}\cdot\vec{p}_{\mathrm{T}})-\mu]}\times \\
&\qquad\qquad\times\Big(m_{\mathrm{T}}\cosh(y-\eta)-\vec{p}_{\mathrm{T}}\cdot\vec{\nabla}_{\mathrm{T}}\,\tau_f(x,\,y)\Big) = \\
&= \frac{2g}{(2\pi)^3}\int dx dy\, \tau_f(x,y)\sum_{n=1}^{\infty}(\mp 1)^{n+1}e^{n\,\beta[\gamma(\vec{v}_{\mathrm{T}}\cdot\vec{p}_{\mathrm{T}})+\mu]}\times \\
&\qquad\qquad\times\Big[m_{\mathrm{T}}\mathrm{K}_1\left(n\,\beta_\perp\right)-\vec{p}_{\mathrm{T}}\cdot\vec{\nabla}_{\mathrm{T}}\,\tau_f(x,\,y)\,\mathrm{K}_0\left(n\,\beta_\perp\right)\Big]\,,
\end{aligned}\tag{A.30}$$

where we have introduced $\beta_\perp = \gamma\, m_{\mathrm{T}}\,\beta = \gamma\, m_{\mathrm{T}}/T$ in the last step.

APPENDIX B

INTEGRALS FOR CORRELATION LENGTHS

Here we discuss the integrals appearing in the evaluation of the correlation lengths as given in Eq. (5.6)

$$\langle g(x,y,z,t)\rangle(K) := \frac{\int d^4x\, g(x,y,z,t)\, S(x,K)}{\int d^4x\, S(x,K)}\,. \tag{B.1}$$

Due to the assumption of boost-invariance, the related coordinate transformation and the remaining δ-function in the definition of the source function $S(x,K)$, Eqs. (5.1, 5.4), two of the four spatial integrations can be done analytically for all desired functions $g(x,y,z,t)$. The remaining numerical work is the integration over the transverse plane (x,y), using the information obtained from the hydrodynamic evolution or some model parametrization.

The τ-integration has the same triviality in all cases as it simply eliminates the remaining δ-function to constrain particle emission to the actual freeze-out hypersurface. However we have to distinguish different classes for the η integration, depending on whether there are additional factors of η coming in through

$$g(x,y,z,t) \to g(x,y,\tau\sinh\eta,\tau\cosh\eta)\,. \tag{B.2}$$

For all applicable cases the η integration is done by the usual trick of expanding the distribution function in a geometrical series which leaves us to evaluate (neglecting chemical potentials)

$$\begin{aligned}
&\int dx dy d\eta \tau d\tau\, g(x,y,\tau\sinh\eta,\tau\cosh\eta) S(x,y,\eta,\tau) = \qquad\qquad \text{(B.3)}\\
&\frac{g_i}{(2\pi)^3}\int dx dy\, \tau_f(x,y) \int d\eta\, g(x,y,\tau_f(x,y)\sinh\eta, \tau_f(x,y)\cosh\eta) \times\\
&\times \sum_{n=1}^{\infty} (\mp)^{n+1} e^{\frac{n}{T}\gamma(m_{\mathrm{T}}\cosh\eta - \vec{v}_\perp\cdot\vec{K}_\perp)} \Big(m_{\mathrm{T}}\cosh\eta - \vec{K}_\perp\cdot\vec{\nabla}_\perp\tau_f(x',\, y')\Big)\,.
\end{aligned}$$

In the following we perform the η-integral analytically, distinguishing four different cases of the function $g(x, y, z, t)$. A list of standard integrals is required for the calculation and is summarized at the end of this Appendix.

CASE 1: $g = g(x, y)$

This is the standard case for averages over functions involving only transverse coordinates x and y. It is also relevant for the case $g \equiv 1$ which gives the thermal particle spectra and appears as normalization in the denominator of the source function, Eq. (B.1). Doing the η integral by using Eq. (B.11) and (B.10) results in

$$\begin{aligned}\langle g(x,\, y)\rangle \;&=\; \frac{2\,g_i}{(2\pi)^3}\int dxdy\,\tau_f(x,y)g(x,y)\sum_{n=1}^{\infty}(\mp)^{n+1}e^{\frac{n}{T}\gamma\vec{v}_\perp\cdot\vec{K}_\perp}\times\\ &\quad\times\Big[m_{\mathrm{T}}\mathrm{K}_1(n\beta_\perp)-\vec{K}_\perp\cdot\vec{\nabla}_\perp\tau_f(x,\,y)\mathrm{K}_0(n\beta_\perp)\Big]\,, \qquad \text{(B.4)}\end{aligned}$$

with $\beta_\perp = \gamma\, m_{\mathrm{T}}/T$. The remaining integration over the transverse coordinates remains to be done numerically.

CASE 2: $g = g(x, y)\tau_f(x, y)\cosh\eta$

These kind of functions arise when evaluating expectation values that are linear in time, in particular $\langle t\rangle$, $\langle xt\rangle$ and $\langle yt\rangle$. The η integral becomes with the help of Eq. (B.13) and (B.11)

$$\begin{aligned}&\langle g(x,y)\tau_f(x,y)\cosh\eta\rangle =\\ &= \frac{2\,g_i}{(2\pi)^3}\int dxdy\,\tau_f^2(x,y)g(x,y)\sum_{n=1}^{\infty}(\mp)^{n+1}e^{\frac{n}{T}\gamma\vec{v}_\perp\cdot\vec{K}_\perp}\times \qquad \text{(B.5)}\\ &\times\left[m_{\mathrm{T}}\left(\mathrm{K}_0(n\beta_\perp)+\frac{1}{n\beta_\perp}\mathrm{K}_1(n\beta_\perp)\right)-\vec{K}_\perp\cdot\vec{\nabla}_\perp\tau_f(x,\,y)\mathrm{K}_1(n\beta_\perp)\right].\end{aligned}$$

Expectation values linear in z vanish due to symmetry.

CASE 3: $g = g(x, y)\tau_f^2(x, y)\sinh^2\eta$

This is needed to evaluate the expectation value $\langle z^2\rangle$, which in our analysis (at $K_l = 0$) is identical to R^2_{long} (see Section 5.3). Here, $g(x, y) \equiv 1$, but we keep it for general reasons. The integral from equ. (B.3) then becomes

$$\begin{aligned}\langle g(x,y)\tau_f^2(x,y)\sinh^2\eta\rangle &= \frac{2\,g_i}{(2\pi)^3}\int dxdy\,\tau_f^3(x,y)g(x,y)\sum_{n=1}^{\infty}(\mp)^{n+1}e^{\frac{n}{T}\gamma\vec{v}_\perp\cdot\vec{K}_\perp} \\ &\times\left[\frac{m_\mathrm{T}}{n\beta_\perp}\mathrm{K}_2(n\beta_\perp)-\frac{1}{n\beta_\perp}\vec{K}_\perp\cdot\vec{\nabla}_\perp\tau_f(x,\,y)\mathrm{K}_1(n\beta_\perp)\right]\,, \qquad \text{(B.6)}\end{aligned}$$

where we have used integrals (B.17) and (B.14).

CASE 4: $g = g(x,y)\tau_f^2(x,y)\cosh^2\eta$

Finally, to evaluate $\langle t^2\rangle$ we use integrals (B.16) and (B.13) and find

$$\begin{aligned}&\langle g(x,y)\tau_f^2(x,y)\cosh^2\eta\rangle = \\ &\frac{2g_i}{(2\pi)^3}\int dxdy\,\tau_f^3(x,y)g(x,y)\sum_{n=1}^{\infty}(\mp)^{n+1}e^{\frac{n}{T}\gamma v_i\mathrm{K}_i}\times \\ &\times\left[m_\mathrm{T}\left(\mathrm{K}_1(n\beta_\perp)+\frac{1}{n\beta_\perp}\mathrm{K}_2(n\beta_\perp)\right)-\right. \qquad \text{(B.7)} \\ &\qquad\left.-\vec{K}_\perp\cdot\vec{\nabla}_\perp\tau_f(x,\,y)\left(\mathrm{K}_0(n\beta_\perp)+\frac{1}{n\beta_\perp}\mathrm{K}_1(n\beta_\perp)\right)\right]\,.\end{aligned}$$

APPLIED STANDARD INTEGRALS

In this Appendix we made extensive use over integrals involving products of exponentials and hypergeometric functions. Useful are the integral definitions of the Bessel function of the first kind, as for example given in [1]:

$$\mathrm{K}_\nu(z) = \frac{\pi^{1/2}\,(\frac{1}{2}z)^\nu}{\Gamma(\nu+\frac{1}{2})}\int_0^\infty dt\,e^{-z\cosh t}\sinh^{2\nu}t\,, \qquad \text{(B.8)}$$

$$\mathrm{K}_\nu(z) = \int_0^\infty dt\,e^{-z\cosh t}\cosh(\nu t)\,, \qquad \text{(B.9)}$$

With these definitions, the following integrals are easily derived:

$$\int_{-\infty}^{\infty}d\eta\,e^{-\beta\cosh\eta} = 2\,\mathrm{K}_0(\beta)\,, \qquad \text{(B.10)}$$

$$\int_{-\infty}^{\infty}d\eta\,e^{-\beta\cosh\eta}\cosh\eta = 2\,\mathrm{K}_1(\beta)\,, \qquad \text{(B.11)}$$

$$\int_{-\infty}^{\infty} d\eta\, e^{-\beta\cosh\eta}\, \sinh\eta = 0\,, \tag{B.12}$$

$$\int_{-\infty}^{\infty} d\eta\, e^{-\beta\cosh\eta}\, \cosh^2\eta = 2\left(\mathrm{K}_0(\beta) + \beta^{-1}\mathrm{K}_1(\beta)\right), \tag{B.13}$$

$$\int_{-\infty}^{\infty} d\eta\, e^{-\beta\cosh\eta}\, \sinh^2\eta = 2\,\beta^{-1}\mathrm{K}_1(\beta)\,, \tag{B.14}$$

$$\int_{-\infty}^{\infty} d\eta\, e^{-\beta\cosh\eta}\, \cosh\eta\sinh\eta = 0\,, \tag{B.15}$$

$$\int_{-\infty}^{\infty} d\eta\, e^{-\beta\cosh\eta}\, \cosh^3\eta = 2\left(\mathrm{K}_1(\beta) + \beta^{-1}\mathrm{K}_2(\beta)\right), \tag{B.16}$$

$$\int_{-\infty}^{\infty} d\eta\, e^{-\beta\cosh\eta}\, \cosh\eta\sinh^2\eta = 2\,\beta^{-1}\mathrm{K}_2(\beta)\,. \tag{B.17}$$

APPENDIX C

FREE STREAMING

In Section 5.4.1 we have discussed the possibility of stronger transverse expansion due to preequilibrium effects and explored two extreme preequilibrium scenarios. In one, we assumed that after formation of the particles at timescale τ_{form} with a locally azimuthally symmetric momentum distribution, non-interacting motion would lead to a separation of faster and slower moving particles and to a separation and an orientation of the random velocities. In such a way, average flow velocities can build up and lead to the existence of flow profiles already at thermalization at $\tau_{\text{equ}} = \tau_{\text{form}} + \Delta\tau$, from when on the system evolves hydrodynamically. In the other extreme we assumed pressure gradients, local thermal equilibrium and an ideal hydrodynamic expansion already at formation time and have $\tau_{\text{equ}} = \tau_{\text{form}}$.

In the first part of this Appendix we present the formalism of the initial free streaming period, the extraction of the resulting flow velocities and the changes of the initial energy density profiles. We use those calculations to put an intuitive example for the free streaming scenario on solid quantitative grounds in the second part of this Appendix.

C.1 FORMALISM

We start with a microscopical description of some initial stage configuration in phase space, expressed by a phase space density $f(\mathbf{r}, \mathbf{p}, t)$. In kinetic theory, the energy momentum tensor of a configuration described by such a phase-space density is given by

$$T^{\mu\nu}_{\text{kin}}(\mathbf{r}, t) = \int \frac{d^3\mathbf{p}}{E}\, p^\mu p^\nu f(\mathbf{r}, \mathbf{p}, t)\,, \qquad \text{(C.1)}$$

where $E = \sqrt{m^2 + \mathbf{p}^2}$ is the energy of a particle with momentum $\mathbf{p}$.

If the particles of our configuration are not interacting, their velocities are fixed and therefore the phase space density at a later time $t + \Delta t$ is simply given as

$$f(\mathbf{r}, \mathbf{p}, t + \Delta t) = f(\mathbf{r} - \frac{\mathbf{p}}{E}\Delta t, \mathbf{p}, t)\,. \tag{C.2}$$

Now we want to work with rapidity and longitudinal proper time again to make it easier to introduce boost invariance. Furthermore we assume that in the initial stage space and momentum configuration have no correlations, i.e. that the spatial and momentum parts of the distribution function factorize. Then we have for the distribution function

$$f(\vec{r}_\perp, \eta, \tau_{\text{form}}; \vec{p}_{\text{T}}, y) = n_0 h(\vec{p}_{\text{T}}) n(\vec{r}_\perp) \delta(y - \eta)\,, \tag{C.3}$$

where $h(\vec{p}_{\text{T}}) = h(p_{\text{T}})$ is the (isotropic) momentum distribution of the generated particles and $n(\vec{r}_\perp)$ is the distribution in coordinate space, i.e. a combination of wounded nucleon and binary collision densities as discussed in Section 2.1. This coordinate space distribution also carries spatial anisotropies in non-central collisions. The δ-function here reflects the longitudinal flow field $v_z = z/t$: a slice of space-time rapidity $\eta = \text{Artanh}\,(z/t)$ is only populated by particles with longitudinal rapidity $y = \text{Artanh}\,(v_z)$.

If we assume free streaming, the collision term of the transport equation vanishes

$$p^\mu \partial_\mu f(x, p) = 0\,. \tag{C.4}$$

While the constituents of the system are freely streaming and spread out in space (according to Eq. (C.2)), their momentum-space distribution is preserved. Therefore the phase-space density at a later time τ has the same structure as Eq. (C.3), with $n(\vec{r}_\perp)$ shifted to $n\left(\vec{r}_\perp - \frac{\vec{p}_{\text{T}}}{m_{\text{T}} \cosh y}(\tau - \tau_{\text{form}})\right)$. Only the normalization factor carries another time-dependence, which is found with the help of the transport equation, Eq. (C.4). Its solution for any time τ later then τ_{form} is given by

$$f(\vec{r}_\perp, \eta, \tau; \vec{p}_{\text{T}}, y) = n_0 \frac{\tau_{\text{form}}}{\tau} \delta(y - \eta) h(\vec{p}_{\text{T}}) n\left(\vec{r}_\perp - \frac{\vec{p}_{\text{T}}}{m_{\text{T}} \cosh y}(\tau - \tau_{\text{form}})\right)\,, \tag{C.5}$$

as is confirmed directly by insertion into the left hand side of Eq. (C.4).

We want to use this transported distribution to extract flow velocities for the hydrodynamic evolution starting at τ_{equ}. Of course it is a drastic step to assume free streaming at one point of time and a fully hydrodynamic expansion at the very next moment. In the freely streaming system there is no pressure, whereas the hydrodynamic evolution is driven by pressure gradients, and we switch from one description to the other at an arbitrary 'equilibration time'. Equilibration can only be achieved by rescattering, and it can therefore not be generated from a free-streaming phase. Being aware of these conceptual problems we continue with a qualitative assessment that should still be able to give an extreme estimate on the influence of an initial free-streaming phase.

By switching from the free-streaming description to the hydrodynamic prescription we want to ensure that energy and momentum is conserved in the transition. We therefore identify the time components of the kinetic energy momentum tensor (C.1) with the transported distribution function (C.5) at $\tau_{\rm equ}$ and the time components of the hydrodynamic energy momentum tensor $T^{\mu\nu}_{\rm hydro}(\mathbf{r},\tau) = (e+P)u^\mu\, u^\nu - g^{\mu\nu}\, P$ to evaluate the average flow fields at the beginning of the hydrodynamic description:

$$T^{0\nu}_{\rm kin}(\vec{r}_\perp, \tau_{\rm equ}) = T^{0\nu}_{\rm hydro}(\vec{r}_\perp, \tau_{\rm equ})\,. \tag{C.6}$$

The other components cannot be matched within this description, as a result of the different concepts of pressure on the hydrodynamic and on the free-streaming side of the transition which was discussed above.

For the transport and connection to a hydrodynamic system, we assume an ideal gas made up of massless particles. The coordinate change in the distribution function of Eq. (C.5) due to transport then becomes $n(\vec{r}_\perp - \Delta\tau\vec{e}_p) = n(x'(\varphi_p),\, y'(\varphi_p))$ with $x'(\varphi_p) = r\cos\varphi_r - \Delta\tau\cos\varphi_p$ and $y'(\varphi_p) = r\sin\varphi_r - \Delta\tau\sin\varphi_p$.

The momentum integral $\int p_{\rm T}\, dp_{\rm T}$ for the kinetic tensor leads to the same constant for all equations in (C.6), and we absorb it in a constant factor N. However the angular integral $\int d\varphi_p$ over the relative angle between $\vec{p}_{\rm T}$ and $\vec{r}_\perp$, leads to the integrals (ν only takes the values 0, 1, 2, as the third spatial component vanishes identically at $z=0$ due to boost invariance)

$$\begin{aligned} T^{0\nu}(r,\varphi_r,\tau_{\rm equ}) \;&=\; \frac{N(\tau_{\rm form})}{\tau_{\rm equ}} \times \\ &\times \int_{-\pi}^{\pi} d\varphi_p \begin{pmatrix} 1 \\ \cos\varphi_p \\ \sin\varphi_p \end{pmatrix} n(r\cos\varphi_r - \Delta\tau\cos\varphi_p, r\sin\varphi_r - \Delta\tau\sin\varphi_p)\,. \end{aligned} \tag{C.7}$$

For an arbitrary distribution function n, which is for example given by the distributions of wounded nucleons and binary collisions as in Section 2.1, these integrals have to be performed numerically. Connecting the results to the ideal hydrodynamic tensor and solving for the energy density leads to

$$e(\vec{r}_\perp, \tau_{\rm equ}) = \sqrt{4\, T^{00\,2} - 3\left(T^{01\,2} + T^{02\,2}\right)} - T^{00}\,, \tag{C.8}$$

and for the velocity flow field ($i = (x,\, y)$ resp. $(1,\, 2)$) one finds

$$v_i(\vec{r}_\perp, \tau_{\rm equ}) = \frac{T^{0i}}{T^{00} + e(\vec{r}_\perp, \tau_{\rm equ})/3}\,. \tag{C.9}$$

Figure C.1 shows such a typical radial velocity field at $\tau = 0.6$ fm/c obtained from this procedure for a formation time of $\tau_{\rm form} = 0.2$ fm/c and $\tau_{\rm equ} = 0.6$ fm/c (red line). In addition the radial velocity field for a system with hydrodynamic evolution starting without flow fields at $\tau_{\rm form} = \tau_{\rm equ} = 0.2$ fm/c is given (blue). The initial energy/entropy densities were chosen as to result in the correct final state multiplicities as described in Sec. 5.4.1. One notices that there are large flow fields already at equilibration time, reaching up to more than 0.4 c. Usually such initial flow velocities are neglected in hydrodynamic and hybrid model calculations, and all flow is built up during the hydrodynamic stage only. Furthermore one notices that in the hottest part of the collision with small $r_\perp$ the fields from free streaming and a hydrodynamic calculation are very much the same. For hydrodynamic simulation starting at $\tau_{\rm form}$ one notices a pronounced dip in the velocity profile at larger radii with $r_\perp \approx 6 - 7$ fm. This dip marks the mixed phase of the system, where pressure gradients vanish and therefore flow fields cannot develop hydrodynamically. For smaller radial distances, the hard plasma phase produces the flow fields, for larger radii, the soft hadronic phase produces radial flow. Before particle production happens in the latest stages of the collision the differences in the hydrodynamic and free streaming initialization will smooth out, and therefore there will not be very drastic differences depending on which preequilibrium scenarios comes closer to reality 5.4.1.

The change in the energy density due to the short free streaming period is rather small and on a few percent level. The slight effect is that matter is shifted to larger radii due to the initial transport.

C.2 ILLUSTRATION WITH A BOX PROFILE

Intuitively, the effect of free streaming is best illustrated along a simple box profile for the distribution of matter in coordinate space i.e. $n(\vec{r}_\perp) = 1$ if $r_\perp \leq R_0$ and 0 otherwise. It is clear that free streaming for a time interval $\Delta\tau$ will give changes in the shape of the energy-density distribution, as the random motion of the particles will gradually lead to a smearing of the sharp step of the distribution. Thereby only particles within a distance smaller than $\Delta\tau \cdot c$ from the rim can be affected as the information that the system is finite cannot propagate faster

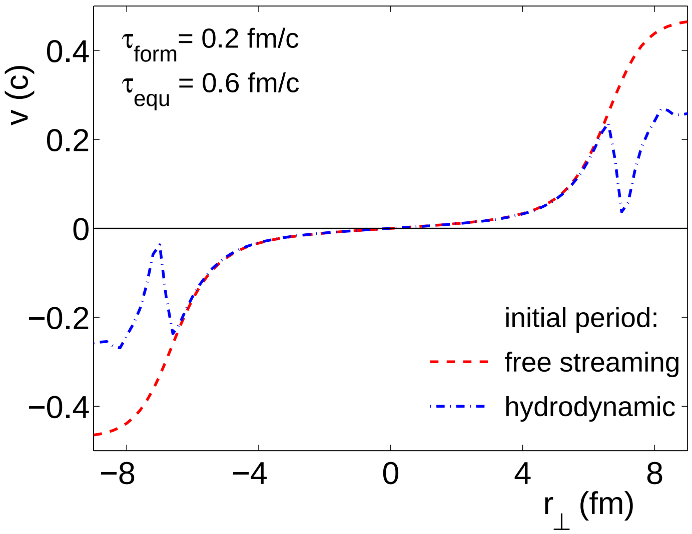

Figure C.1: Radial flow fields at $\tau = 0.6$ fm/c, as a result from free streaming in the equilibration process (dashed), or from a full hydrodynamical treatment starting at equilibration time (dash-dotted). There, the pronounced minimum at $r_\perp \sim 7$ fm results from the inert mixed phase of the system.

than with speed of light. This will follow naturally from the formalism presented above.

Also the sift of the random velocities, resulting in a finite average radial velocity at radial distances $r_\perp$ between $R_0 - \Delta\tau$ and $R_0 + \Delta\tau$ gets obvious by looking at a box profile. Particles which have reached the distance $R_0 + \Delta\tau$ can have only gotten there if they started out from the distance R_0 and traveled radially outwards with the speed of light. At smaller radial distances the average velocity is a little smaller. For radii smaller than $R_0 - \Delta\tau$, no flow profile has built up and the density distribution is still flat as the random motion from either side cancel any effects out. In between the two extremes of $R_0 \pm \Delta\tau$ there now exists a continuous, monotonically increasing flow profile.

Expressing the particle distribution in cylindrical coordinates after a free streaming interval $\Delta\tau$ becomes

$$n\left(\vec{r}_\perp - \Delta\tau\vec{e}_\perp\right) = n\left(\sqrt{\vec{r}_\perp^{\,2} + \Delta\tau^2 - 2r_\perp\Delta\tau\cos\varphi_p}\right) . \tag{C.10}$$

For the box profile the integrals in Eq. (C.7) and the subsequent steps for the extraction of the energy density and velocity profiles can be easily performed. For $r_\perp \in [R_0 - \Delta\tau,\, R_0 + \Delta\tau]$ one arrives at

$$v_\perp = \frac{2\,\psi_r}{\sin\psi_r} - \sqrt{\left(\frac{2\,\psi_r}{\sin\psi_r}\right)^2 - 3}\,, \tag{C.11}$$

and

$$e = \frac{3}{2}N\frac{1-v_\perp^2}{v_\perp}\sin\psi_r\,. \tag{C.12}$$

Here we have introduced the abbreviation $\psi_r = \arccos \frac{(r/R_0)^2+(\Delta\tau/R_0)^2-1}{2\,r/R_0\,\Delta\tau/R_0}$. The normalization $N = \tau_{\rm equ}/\tau_{\rm form}$ results from longitudinal expansion during the free-streaming interval $\Delta\tau$.

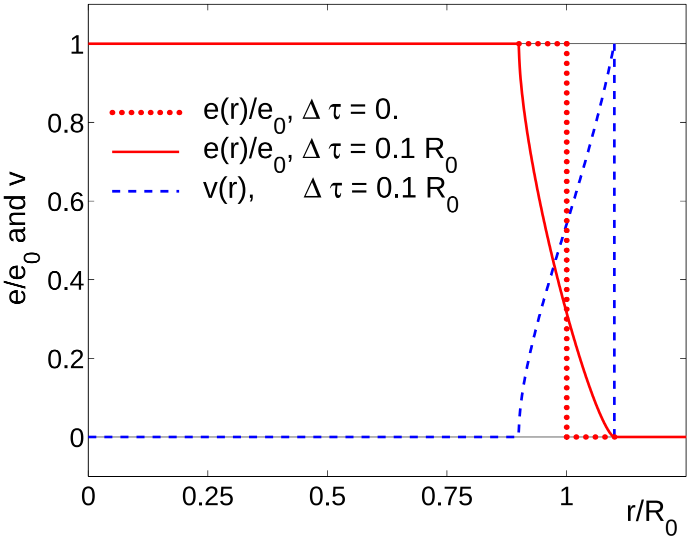

Figure C.2: Energy density (solid) and velocity profile (dashed) resulting from an initial box profile (dotted) after a free streaming interval $\Delta\tau = 0.1 R_0$. For clarity the density distributions are normalized to their maximum value.

This resulting flow and energy density profile is depicted in Figure C.2 for a ratio $\Delta\tau/R_0 = 0.1$. Again, this figure suggests that even a moderate free-streaming duration of 0.4 fm/c can lead to significant effects. This strong velocity profile results of course from the steep rim in the initial condition. Starting with an initial Gaussian distribution in the transverse plane one finds that the velocity profile increases approximately linearly from the origin as

$$v_\perp = \frac{3}{4}\frac{r_\perp \Delta\tau}{R_0^2}\,. \tag{C.13}$$

with changes in the energy density distribution which are only of the order of a few per cent. This is a more gradual flow profile, however it extends over the full fireball region.

Appendix D

Glossary

Colliders, Facilities and Experiments

AGS	Alternating Gradient Syncrotron at BNL, fixed target experiments with $\sqrt{s_{\mathrm{NN}}} \sim 5$ GeV
BNL	Brookhaven National Laboratory, Long Island, New York `http://www.bnl.gov`
BRAHMS	'Small scale' experiment at RHIC measuring multiplicities and spectra of hadrons
CERN	Conseil Européen pour la Recherche Nucléaire – European Organization for Nuclear Research, Geneva, Switzerland `http://www.cern.ch`
LHC	Large Hadron Collider at CERN collider experiments with $\sqrt{s_{\mathrm{NN}}} \sim 5.5$ TeV for nuclear collisions first experiments with heavy ions expected in 2007
PHENIX	Experiment at RHIC, large spectrometer for the measurement of photons, electrons, muons and hadrons
PHOBOS	'Small scale' experiment at RHIC aiming for rapid identification of characteristic observables
RHIC	Relativistic Heavy Ion Collider at BNL, collider experiments with $\sqrt{s_{\mathrm{NN}}} \sim 50 - 200$ GeV first run in year 2000 with $\sqrt{s_{\mathrm{NN}}} \sim 130$ GeV
SPS	Super Proton Syncrotron at CERN, fixed target experiments with $\sqrt{s_{\mathrm{NN}}} \sim 20$ GeV
STAR	Solenoidal Tracker At RHIC large time projection chamber with full azimuthal coverage

MOST IMPORTANT VARIABLES

β	inverse temperature $\beta = 1/T$
ϵ_p, ϵ_x	momentum anisotropy, spatial anisotropy
$\epsilon^{\mu\nu\alpha\beta}$	totally antisymmetric tensor of fourth order
η	space time rapidity, $\eta = \text{Artanh}\,(z/t) = \frac{1}{2}\ln\frac{t+z}{t-z}$
η	pseudorapidity, $\eta = \text{Artanh}\,(p_z/p) = \frac{1}{2}\ln\frac{p+p_z}{p-p_z} = \ln\frac{p+p_z}{p_\text{T}}$
γ	(Lorentz) contraction factor, $\gamma = 1/\sqrt{1-v^2}$
μ	chemical potential
Σ	freeze-out hypersurface, $\Sigma^\mu = (\Sigma^0(x), \Sigma^1(x), \Sigma^2(x), \Sigma^3(x))$
τ	longitudinal proper time
τ_f	freeze-out time
ρ	transverse flow rapidity
φ_p	angle in momentum space, $\varphi_p = \arctan(p_y/p_x)$
φ_s	angle in coordinate space, $\varphi_s = \arctan(y/x)$
Ω	thermodynamic potential
B	bag constant
b	impact parameter
c_s	speed of sound
$d^3\sigma_\mu$	normal vector on the freeze-out hypersurface
e, E, E_T	energy density, energy, transverse energy
$f(x, p)$	phase-space distribution function
$g^{\mu\nu}$, g^{mn}	metric tensor
$h(p)$	momentum distribution function
I_i	modified Bessel function
K_i	modified Bessel function
$K_\perp$	transverse particle (pair) momentum
m	mass
m_T	transverse mass, $m_\text{T} = \sqrt{m^2 + p_\text{T}^2} = \sqrt{E^2 - p_z^2}$
n	baryon number density
N_ch	produced charged hadrons
P	pressure
p_T	transverse momentum, $p_\text{T} = \sqrt{p_x^2 + p_y^2}$
R	nuclear radius
s, S	entropy density, entropy
$\sqrt{s_\text{NN}}$	center of mass energy per nucleon pair
T	temperature
$T^{\mu\nu}$	energy-momentum tensor
u^μ	flow four-velocity
v, $v_\perp$	velocity, transverse velocity
v_1, v_2	directed flow, elliptic flow coefficients
V	volume
y	rapidity, $y = \text{Artanh}\,(p_z/E) = \frac{1}{2}\ln\frac{E+p_z}{E-p_z} = \ln\frac{E+p_z}{m_\text{T}}$

BIBLIOGRAPHY

[1] M. Abramowitz and I.A. Stegun (editors), "Handbook of mathematical functions", (Dover Publications Inc., New York, 1970).

[2] K.H. Ackermann et al. (STAR Collaboration), "Elliptic flow in Au+Au collisions at $\sqrt{s_{NN}} = 130$ GeV", Phys. Rev. Lett. 86 (2001) 402.

[3] K. Adcox et al. (PHENIX Collaboration), "Centrality dependence of charged particle multiplicity in Au-Au collisions at $\sqrt{s_{NN}} = 130$ GeV", Phys. Rev. Lett. 86 (2001) 3500.

[4] K. Adcox et al. (PHENIX Collaboration), "Measurement of the midrapidity transverse energy distribution from $\sqrt{s_{NN}}$=130 GeV Au+Au collisions at RHIC", Phys. Rev. Lett. 87 (2001) 052301.

[5] K. Adcox et al. (PHENIX Collaboration), "Transverse mass dependence of two-pion correlations in Au+Au collisions at $\sqrt{s_{NN}}$=130 GeV", nucl-ex/0201008.

[6] C. Adler et al. (STAR Collaboration), "Pion interferometry of $\sqrt{s_{NN}} =$ 130 GeV Au+Au collisions at RHIC", Phys. Rev. Lett. 87 (2001) 082301.

[7] C. Adler et al. (STAR Collaboration), "Midrapidity antiproton-to-proton ratio from Au+Au collisions at $\sqrt{s_{NN}} = 130$ GeV", Phys. Rev. Lett. 86 (2001) 4778.

[8] C. Adler et al. (STAR Collaboration), "Multiplicity distribution and spectra of negatively charged hadrons in Au+Au collisions at $\sqrt{s_{NN}} = 130$ GeV", Phys. Rev. Lett. 87 (2001) 112303.

[9] C. Adler et al. (STAR Collaboration), "Identified particle elliptic flow in Au+Au collisions at $\sqrt{s_{NN}} = 130$ GeV", Phys. Rev. Lett. 87 (2001) 182301.

[10] C. Adler et al. (STAR Collaboration), "Measurement of inclusive antiprotons from Au+Au collisions at $\sqrt{s_{NN}}$ = 130 GeV", Phys. Rev. Lett. 87 (2001) 262302.

[11] M.M. Aggarwal et al. (WA98 Collaboration), "Scaling of particle and transverse energy production in ^{208}Pb+^{208}Pb collisions at 158 AGeV", Eur. Phys. J. C 18 (2001) 651.

[12] H. Appelshäuser et al. (NA49-Collaboration), "Directed and elliptic flow in 158 GeV/nucleon Pb+Pb collisions", Phys. Rev. Lett. 82 (1999) 2471.

[13] H. Appelshäuser et al. (NA49-Collaboration), "Baryon stopping and charged particle distributions in central Pb+Pb collisions at 158 GeV per nucleon", Phys. Rev. Lett. 82 (1999) 2471.

[14] B.B. Back et al. (PHOBOS Collaboration), "Charged-particle multiplicity near midrapidity in central Au+Au collisions at $\sqrt{s_{NN}} = 56$ and 130 GeV", Phys. Rev. Lett. 85 (2000) 3100.

[15] B.B. Back et al. (PHOBOS Collaboration), "Centrality dependence of charged particle multiplicity at mid-rapidity in Au+Au collisions at $\sqrt{s_{NN}} = 130$ GeV", nucl-ex/0105011, submitted to Phys. Rev. Lett.

[16] B.B. Back et al. (PHOBOS Collaboration), "Charged-particle pseudorapidity density distributions from Au+Au collisions at $\sqrt{s_{\mathrm{NN}}} = 130$ GeV", Phys. Rev. Lett. 87 (2001) 102303.

[17] B.B. Back et al. (PHOBOS Collaboration), "Energy dependence of particle multiplicities in central Au+Au collisions", Phys. Rev. Lett. 88 (2002) 022302.

[18] B.B. Back et al. (PHOBOS Collaboration), "Centrality dependence of the charged particle multiplicity near mid-rapidity in Au+Au collisions at $\sqrt{s_{\mathrm{NN}}}$ = 130 and 200 GeV", nucl-ex/0201005, submitted to Phys. Rev. C.

[19] S.A. Bass et al., "Last call for RHIC predictions", Nucl. Phys. A 661 (1999) 205 in [142].

[20] S.A. Bass et al., "Hadronic freezeout following a first order hadronization phase transition in ultrarelativistic heavy ion collisions" Phys. Rev. C 60 (1999) 021902.

[21] S.A. Bass and A. Dumitru, "Dynamics of hot bulk QCD matter: from the quark gluon plasma to hadronic freezeout", Phys. Rev. C 61 (2000) 064909.

[22] S.A. Bass, "Microscopic reaction dynamics at SPS and RHIC", Nucl. Phys. A 698 (2002) 164 in [143].

[23] I.G. Bearden et al. (NA44 Collaboration), "Collective expansion in high energy heavy ion collisions", Phys. Rev. Lett. 78 (1997) 2080.

[24] I.G. Bearden et al. (BRAHMS Collaboration), "Pseudorapidity distributions of charged particles from Au+Au collisions at the maximum beam energy", nucl-ex/0112001.

[25] A. Bialas, M. Bleszynski, and W. Czyz, "Multiplicity distributions in nucleus-nucleus collisions at high energies", Nucl. Phys. B 111 (1976) 461.

[26] T.S. Biró, "Analytic solution for relativistic transverse flow at the softest point", Phys. Lett. B 474 (2000) 21; T.S. Biró, "Generating new solutions for relativistic transverse flow at the softest point", Phys. Lett. B 487 (2000) 133.

[27] J.D. Bjorken, "Highly relativistic nucleus-nucleus collisions: The central rapidity region", Phys. Rev. D 27 (1983) 140.

[28] J.P. Blaizot and J.Y. Ollitrault, "Hydrodynamics of a quark gluon plasma", in:"Quark Gluon Plasma II", (R.C. Hwa ed., World Scientific, Singapore, 1990, p. 393).

[29] A. Bohr and B.R. Mottelson, "Nuclear structure", (Benjamin, New York, 1969).

[30] J.P. Boris, D.L. Book, "Flux-corrected transport I: SHASTA, a fluid transport algorithm that works", J. Comp. Phys. 11 (1973) 38; J.P. Boris, D.L. Book, and K. Hain, "Flux-corrected transport II: Generalization of the method", J. Comp. Phys. 18 (1975) 248.

[31] P. Braun-Munzinger, I. Heppe, and J. Stachel, "Chemical equilibration in Pb+Pb collisions at the SPS", Phys. Lett. B 465 (1999) 15.

[32] P. Braun-Munzinger, D. Magestro, K. Redlich, and J. Stachel, "Hadron production in Au - Au collisions at RHIC", Phys. Lett. B 518 (2001) 41.

[33] W. Broniowski and W. Florkowski, "Description of the RHIC $p_\perp$-spectra in a thermal model with expansion", nucl-th/0106050.

[34] K.A. Bugaev and M.I. Gorenstein, "Particle freezeout in selfconsistent relativistic hydrodynamics", nucl-th/9903072.

[35] J. Burward-Hoy, “Transverse momentum distributions of hadrons produced in Au+Au collisions at 130 GeV measured by the PHENIX experiment at RHIC BNL.”, PhD-thesis, State University of New York, Stony Brook, December 2001.

[36] M. Calderon de la Barca Sanchez, “Charged hadron spectra in Au+Au collisions at a $\sqrt{s_{\rm NN}} = 130$ GeV”, PhD-thesis, Yale University, December 2001.

[37] S. Chapman and U. Heinz, “HBT correlators: current formalism versus Wigner function formulation”, Phys. Lett. B 340 (1994) 250.

[38] S. Chapman, P. Scotto, and U. Heinz, “New cross term in the two-particle Hanbury-Brown-Twiss correlation function in ultrarelativistic heavy ion collisions”, Phys. Rev. Lett. 74 (1995) 4400.

[39] F. Cooper and G. Frye, “Single particle distribution in the hydrodynamic and statistical thermodynamic models of multiparticle production”, Phys. Rev. D 10 (1974) 186.

[40] L.P. Csernai, “Introduction to relativistic heavy ion collisions”, (Wiley, New York, 1994).

[41] P. Danielewicz, “Effects of compression and collective expansion on particle emission from central heavy ion reactions”, Phys. Rev. C 51 (1995) 716.

[42] P. Danielewicz et al., “Disappearance of elliptic flow: a new probe for the nuclear equation of state”, Phys. Rev. Lett. 81 (1998) 2438.

[43] P. Danielewicz, “Flow and the equation of state of nuclear matter”, Nucl. Phys. A 685 (2001) 368.

[44] H. Dobler, J. Sollfrank, and U. Heinz, “Kinetic freezeout and radial flow in 11.6 GeV/A Au+Au collisions”, Phys. Lett. B 457 (1999) 353.

[45] A. Dumitru and M. Gyulassy, “The effective pressure of a saturated gluon plasma”, Phys. Lett. B 494 (2000) 215.

[46] J. Engels, F. Karsch, H. Satz, and I. Montvay, “Gauge field thermodynamics for the SU(2) Yang-Mills system”, Nucl. Phys. B 205 (1982) 545.

[47] K.J. Eskola, K. Kajantie, P.V. Ruuskanen, and K. Tuominen, “Scaling of transverse energies and multiplicities with atomic number and energy in ultrarelativistic nuclear collisions”, Nucl. Phys. B 570 (2000) 379.

[48] K.J. Eskola, K. Kajantie, and K. Tuominen, “Centrality dependence of multiplicities in ultrarelativistic nuclear collisions”, Phys. Lett. B 497 (2001) 39.

[49] K. Geiger and B. Müller, “Dynamics of parton cascades in highly relativistic nuclear collisions”, Nucl. Phys. B 369 (1992) 600.

[50] K. Geiger, “Space-time description of ultrarelativistic nuclear collisions in the QCD parton picture”, Phys. Rept. 258 (1995) 237.

[51] R.J. Glauber, in “Lectures on Theoretical Physics”, Vol. 1, (W.E. Brittin, L.G. Dunham eds., Interscience, NY, 1959).

[52] D.E. Groom et al. (Particle Data Group), “The review of particle physics”, Eur. Phys. J. C 15 (2000) 1.

[53] D.J. Gross and F. Wilczek, “Ultraviolet behavior of nonabelian gauge theories”, Phys. Rev. Lett. 30 (1973) 1343.

[54] M. Gyulassy and X.N. Wang, “Multiple collisions and induced gluon bremsstrahlung in QCD”, Nucl. Phys. B 420 (1994) 583.

[55] M. Gyulassy, I. Vitev, and X.N. Wang, “High p_{T} azimuthal asymmetry in noncentral A+A at RHIC”, Phys. Rev. Lett. 86 (2001) 2537.

[56] M. Gyulassy, I. Vitev, X.N. Wang, and P. Huovinen, “Transverse expansion and high p_{T} azimuthal asymmetry at RHIC”, nucl-th/0109063.

[57] R. Hanbury-Brown and R.Q. Twiss, “A test of a new type of stellar interferometer on sirius”, Nature 178 (1956) 1046.

[58] U. Heinz, K.S. Lee, and E. Schnedermann, “Hadronizatin of a quark gluon plasma” in “Quark Gluon Plasma” (R.C. Hwa ed., World Scientific, Singapore, 1990).

[59] U. Heinz and B.V. Jacak, “Two particle correlations in relativistic heavy ion collisions”, Ann. Rev. Nucl. Part. Sci. 49 (1999) 529.

[60] U. Heinz and M. Jacob, “Evidence for a new state of matter: An assessment of the results from the CERN lead beam programme”, nucl-th/0002042.

[61] U. Heinz and P.F. Kolb, “Early thermalization at RHIC”, hep-ph/0111075, to be published in Nucl. Phys. A.

[62] H. Heiselberg and A.M. Levy, “Elliptic flow and Hanbury-Brown–Twiss correlations in noncentral nuclear collisions”, Phys. Rev. C 59 (1999) 2716.

[63] N. Herrmann, J.P. Wessels, and T. Wienold, “Collective flow in heavy ion collisions”, Ann. Rev. Nucl. Part. Sci. 49 (1999) 581.

[64] T. Hirano, K. Morita, S. Muroya, and C. Nonaka, “Hydrodynamical analysis of hadronic spectra in the 130 GeV / nucleon Au+Au collisions”, nucl-th/0110009.

[65] T. Hirano, “Is early thermalization achieved only near midrapidity in Au+Au collisions at $\sqrt{s_{\mathrm{NN}}} = 130$ GeV?”, Phys. Rev. C 65 (2002) 011901(R).

[66] C.M. Hung and E.V. Shuryak, “Hydrodynamics near the QCD phase transition: Looking for the longest-lived fireball”, Phys. Rev. Lett. 75 (1995) 4003.

[67] C.M. Hung and E. V. Shuryak, “Equation of state, radial flow and freezeout in high-energy heavy ion collisions”, Phys. Rev. C 57 (1998) 1891.

[68] P. Huovinen, P.F. Kolb, U. Heinz, P.V. Ruuskanen, and S.A. Voloshin, “Radial and elliptic flow at RHIC: further predictions”, Phys. Lett. B 503 (2001) 58.

[69] P. Huovinen, P.F. Kolb, and U. Heinz, “Is there elliptic flow without transverse flow?”, Nucl. Phys. A 698 (2002) 475 in [143].

[70] S. Johnson et al. (PHENIX Collaboration), “First measurements of pion correlations by the PHENIX experiment”, Nucl. Phys. A 698 (2002) 603 in [143].

[71] J. Kapusta, L. McLerran, and D.K. Srivastava, “Rates for dilepton production at RHIC and LHC between J/Ψ and Υ are big”, Phys. Lett. B 283 (1992) 145.

[72] F. Karsch, “Lattice results on QCD thermodynamics”, Nucl. Phys. A 698 (2002) 199 in [143].

[73] D. Kharzeev and M. Nardi, “Hadron production in nuclear collisions at RHIC and high-density QCD”, Phys. Lett. B 507 (2001) 121.

[74] P.F. Kolb, J. Sollfrank, and U. Heinz, “Anisotropic flow from AGS to LHC energies”, Phys. Lett. B 459 (1999) 667.

[75] P.F. Kolb, J. Sollfrank, and U. Heinz, “Anisotropic transverse flow and the quark-hadron phase transition”, Phys. Rev. C 62 (2000) 054909.

[76] P.F. Kolb, J. Sollfrank, P.V. Ruuskanen, and U. Heinz, "Hydrodynamic simulation of elliptic flow", Nucl. Phys. A 661 (1999) 349 in [142].

[77] P.F. Kolb, P. Huovinen, U. Heinz, and H. Heiselberg, "Elliptic flow at SPS and RHIC: from kinetic transport to hydrodynamics", Phys. Lett. B 500 (2001) 232.

[78] P.F. Kolb, P. Huovinen, U. Heinz, K. Eskola, and K. Tuominen, "Centrality dependence of multiplicity, transverse energy, and elliptic flow from hydrodynamics", Nucl. Phys. A 696 (2001) 175.

[79] P.F. Kolb, "Hydrodynamic flow at RHIC", nucl-th/0104089, published in [144].

[80] R.A. Lacey et al. (PHENIX Collaboration), "Elliptic flow measurements with the PHENIX detector", Nucl. Phys. A 698 (2002) 559 in [143].

[81] L.D. Landau, "On the multiparticle production in high energy collisions", Izv. Akad. Nauk Ser. Fiz. 17 (1953) 51.

[82] L.D. Landau, E.M. Lifshitz, "Fluid mechanics", (Addison-Wesley, Reading, Mass., 1959).

[83] K.S. Lee, M.J. Rhoades-Brown, and U. Heinz, "Quark-gluon plasma versus hadron gas. What one can learn from hadron abundances", Phys. Rev. C 37 (1988) 1452.

[84] K.S. Lee, U. Heinz, and E. Schnedermann, "Search for collective transverse flow using particle transverse momentum spectra in relativistic heavy ion collisions", Z. Phys. C 48 (1990) 525.

[85] B.A. Li, "Uranium on uranium collisions at relativistic energies", Phys. Rev. C 61 (2000) 021903(R).

[86] Z.W. Lin and C.M. Ko, "Partonic effects on the elliptic flow at relativistic heavy ion collisions", nucl-th/0108039.

[87] M.A. Lisa, U. Heinz, and U.A. Wiedemann, "Tilted pion sources from azimuthally sensitive HBT interferometry", Phys. Lett. B 489 (2000) 287.

[88] M.A. Lisa et al. (E895 Collaboration), "Azimuthal dependence of pion interferometry at the AGS", Phys. Lett. B 496 (2000) 1.

[89] M.A. Lisa, and R. Wells, unpublished preprint and private communication.

[90] L. McLerran and J. Schaffner-Bielich, “Intrinsic broadening of the transverse momentum spectra in ultrarelativistic heavy ion collisions?” Phys. Lett. B 514 (2001) 29.

[91] D. Molnar and M. Gyulassy, “Saturation of elliptic flow at RHIC: Results from the covariant elastic parton cascade model MPC”, nucl-th/0104073.

[92] J.-Y. Ollitrault, “Anisotropy as a signature of transverse collective flow”, Phys. Rev. D 46 (1992) 229.

[93] I. Park et al. (PHOBOS Collaboration), “Charged particle flow measurement for $|\eta| < 5.3$ with the PHOBOS detector”, Nucl. Phys. A 698 (2002) 564 in [143].

[94] H.D. Politzer, “Reliable perturbative results for strong interactions?”, Phys. Rev. Lett. 30 (1973) 1346.

[95] J. Polonyi, H.W. Wyld, J.B. Kogut, J. Shigemitsu, and D.K. Sinclair, “Finite-temperature phase transitions in SU(3) lattice gauge theory with dynamical light fermions”, Phys. Rev. Lett. 53 (1984) 644.

[96] A.M. Poskanzer and S.V. Voloshin (NA49 Collaboration), “Centrality dependence of directed and elliptic flow at the SPS”, Nucl. Phys. A 661 (1999) 341 in [142].

[97] A.M. Poskanzer, “Anisotropic flow at the SPS and RHIC”, nucl-ex/0110013, to be published in [145].

[98] S. Pratt, “Validity of the smoothness assumption for calculating two-boson correlations in high-energy collisions”, Phys. Rev. C 56 (1997) 1095.

[99] S. Pratt, private communication, after a talk given at the ’Midwest theory get-together’, Argonne National Laboratory, October 5-6, 2001.

[100] K. Rajagopal and F. Wilczek, “The condensed matter physics of QCD”, in “At the frontier of particle physics / Handbook of QCD”, (M. Shifman ed., World Scientific, Singapore, 2001).

[101] F. Retière et al. (STAR Collaboration), “Two-particle correlations in Au+Au collisions at $\sqrt{s_{NN}} = 130$ GeV”, nucl-ex/0111013, to be published in [145].

[102] D.H. Rischke, M.I. Gorenstein, H. Stöcker, and W. Greiner, “Excluded volume effect for the nuclear matter equation of state”, Z. Phys. C 51 (1991) 485.

[103] D.H. Rischke and M. Gyulassy, "The time-delay signature of quark-gluon plasma formation in relativistic nuclear collisions", Nucl. Phys. A 608 (1996) 479.

[104] P.V. Ruuskanen, "Transverse hydrodynamics with a first order phase transition in very high energy nuclear collisions", Acta Phys. Pol. 18 (1987) 551.

[105] J. Schaffner-Bielich, D. Kharzeev, L. McLerran, and R. Venugopalan, "Generalized scaling of the transverse mass spectrum at the Relativistic Heavy Ion Collider", nucl-th/0108048.

[106] B.R. Schlei, U. Ornik, M. Plümer, and R.M. Weiner, "Transverse expansion and effective radii of sources in high-energy collisions", Phys. Lett. B 293 (1992) 275.

[107] E. Schnedermann and U. Heinz, "A hydrodynamical assessment of 200 AGeV collisions", Phys. Rev. C 50 (1994) 1675.

[108] E. Schnedermann, J. Sollfrank, and U. Heinz, "Fireball spectra", in: "Particle production in highly excited matter", (H.H. Gutbord and J. Rafelski, eds., Plenum Publ., New York, 1993).

[109] E. Schnedermann, J. Sollfrank, and U. Heinz, "Thermal Phenomenology of hadrons from 200A GeV S+S collisions", Phys. Rev. C 48 (1993) 2462.

[110] E.V. Shuryak, "The correlation of identical pions in multiboson production", Phys. Lett. B 44 (1973) 387.

[111] E.V. Shuryak, "QCD and the theory of superdense matter", Phys. Rept. 61 (1980) 71.

[112] E.V. Shuryak, "High energy collisions of strongly deformed nuclei: An old idea with a new twist", Phys. Rev. C 61 (2000) 034905.

[113] P.J. Siemens and J.O. Rasmussen, "Evidence for a blast wave from compressed nuclear matter", Phys. Rev. Lett. 42 (1979) 880.

[114] Y.M. Sinyukov, "Boson spectra and correlations in small thermalized systems", in "Hot hadronic matter: theory and experiment", (J. Letessier et al., eds., Plenum, New York, 1995).

[115] R. Snellings et al. (STAR Collaboration), "Elliptic flow in Au+Au collisions at $\sqrt{s_{NN}} = 130$ GeV", Nucl. Phys. A 698 (2002) 193 in [143].

[116] S. Soff, S.A. Bass, and A. Dumitru, "Pion interferometry at RHIC: Probing a thermalized quark gluon plasma", Phys. Rev. Lett. 86 (2001) 3981.

[117] J. Sollfrank, P. Koch, and U. Heinz, "The influence of resonance decays on the p_T spectra from heavy ion collisions", Phys. Lett. B 252 (1990) 256.

[118] J. Sollfrank, M. Gazdzicki, U. Heinz, and J. Rafelski, "Chemical freezeout conditions in central SS collisions at 200 AGeV", Z. Phys. C 61 (1994) 659.

[119] J. Sollfrank et al., "Hydrodynamical description of 200A GeV/c S+Au collisions: Hadron and electromagnetic spectra", Phys. Rev. C 55 (1997) 392.

[120] H. Sorge, "Elliptical flow: a signature for early pressure in ultrarelativistic nucleus-nucleus collisions", Phys. Rev. Lett. 78 (1997) 2309.

[121] H. Sorge, "Highly sensitive centrality dependence of elliptic flow: a novel signature of the phase transition in QCD", Phys. Rev. Lett. 82 (1999) 2048.

[122] H. Stöcker and W. Greiner, "High-energy heavy ion collisions: probing the equation of state of highly excited hadronic matter", Phys. Rept. 137 (1986) 277.

[123] D. Teaney and E. Shuryak, "Unusual space-time evolution for heavy ion collisions at high energies due to the QCD phase transition", Phys. Rev. Lett. 83 (1999) 4951.

[124] D. Teaney, "Collective flow in ultra-relativistic heavy ion collisions", PhD-thesis, State University of New York, Stony Brook, August 2001.

[125] D. Teaney, J. Lauret, and E.V. Shuryak, "Flow at the SPS and RHIC as a quark gluon plasma signature", Phys. Rev. Lett. 86 (2001) 4783.

[126] D. Teaney, J. Lauret, and E.V. Shuryak, "A hydrodynamic description of heavy ion collisions at the SPS and RHIC", nucl-th/0110037.

[127] J. Velkovska et al. (PHENIX Collaboration), "P_t Distributions of identified charged hadrons measured with the PHENIX experiment at RHIC", Nucl. Phys. A 698 (2002) 507 in [143].

[128] X.N. Wang and M. Gyulassy, "HIJING: a Monte Carlo model for multiple jet production in pp, pA and AA collisions", Phys. Rev. D 44 (1991) 3501.

[129] X.N. Wang, "Jet quenching and azimuthal anisotropy of large p_T spectra in noncentral high-energy heavy ion collisions", Phys. Rev. C 63 (2001) 054902.

[130] U.A. Wiedemann, "Two-particle interferometry for noncentral heavy ion collisions", Phys. Rev. C 57 (1998) 266.

[131] U.A. Wiedemann and U. Heinz, "Particle interferometry for relativistic heavy ion collisions", Phys. Rept. 319 (1999) 145.

[132] C.Y. Wong, "Introduction to high-energy heavy ion collisions", (World Scientific, Singapore, 1994).

[133] N. Xu and M. Kaneta, "Hadron freeze-out conditions in high energy nuclear collisions", Nucl. Phys. A 698 (2002) 306 in [143].

[134] C.N. Yang and R.L. Mills, "Conservation of isotopic spin and isotopic gauge invariance", Phys. Rev. 96 (1954) 191.

[135] E.E. Zabrodin, C. Fuchs, L.V. Bravina, and A. Faessler, "Elliptic flow at collider energies and cascade string models: the role of hard processes and multi-pomeron exchanges", Phys. Lett. B 508 (2001) 184.

[136] S.T. Zalesak, "Fully multidimensional flux-corrected transport algorithms for fluids", J. Comp. Phys. 31 (1979) 38.

[137] B. Zhang, M. Gyulassy, and C.M. Ko, "Elliptic flow from a parton cascade", Phys. Lett. B 455 (1999) 45.

[138] B. Zhang, C.M. Ko, B.A. Li, and Z.W. Lin, "A multiphase transport model for nuclear collisions at RHIC", Phys. Rev. C 61 (2000) 067901.

[139] D. Zschiesche, S. Schramm, H. Stöcker, and W. Greiner, "Space-time evolution and HBT analysis of relativistic heavy ion collisions in a chiral $SU(3) \times SU(3)$ model", nucl-th/0107037.

[140] "A new state of matter created at CERN", CERN press release, February 10, 2000, `http://cern.web.cern.ch/CERN/Announcements/2000/` `/NewStateMatter/`

[141] "Statistical mechanics of quarks and hadrons", International Symposium, Bielefeld, Germany, August 24-31, 1980, (H. Satz, ed.), Amsterdam, Netherlands, North-Holland (1981).

[142] Proceedings of the 14th International Conference on Ultrarelativistic Nucleus-Nucleus Collisions (QM 99), Torino, Italy, May 10-15, 1999, (L. Riccati, M. Masera, and E. Vercelli, eds.), Nucl. Phys. A 661 (1999) 1.

[143] Proceedings of the 15th International Conference on Ultrarelativistic Nucleus-Nucleus Collisions (QM 2001), Stony Brook, New York, January 15-20, 2001, Nucl. Phys. A 698 (2002) 1.

[144] Proceedings of the 17th Winter Workshop on Nuclear Dynamics, Park City, Utah, March 10-17, 2001, (G.D. Westfall and W. Bauer, eds.), EP Systema, Debrecen, Hungary (2001)

[145] Proceedings of the International Workshop on the Physics of the Quark-Gluon Plasma, Palaiseau, France, 4-7 September 2001.

HERZLICHEN DANK !

I am most grateful for all the circumstances which brought me into the lecture on Theoretical Mechanics by Professor Ulrich Heinz at the University of Regensburg in winter 1994. His enthusiasm increased my interests in theoretical physics even further and some years later I was happy to find out that his skills as a supervisor are of similar magnitude as his devotion to lecturing. Only through his guidance, continuous input and encouragement could I manage to set foot in up-to-date research and also participate actively in it. His critical remarks on the draft of this thesis also helped to bring it to its final shape. I am also indebted to Josef Sollfrank who caused the prime spark to light my curiosity on flow in heavy ion collisions. I further thank Professor Andreas Schaefer and the Department of Physics of the University of Regensburg for continuous support.

For the stimulating atmosphere in the Theoretical Nuclear Physics Group at the Ohio State University and the many delicious lunches on Fridays, I would like to thank Professors Bunny Clark, Richard Furnstahl (who also showed great patience in the resolution of various computer problems), Sabine Jeschonnek, and Robert Perry.

I greatly acknowledge the very fruitful collaborations with Kari Eskola, Henning Heiselberg, Pasi Huovinen, Vesa Ruuskanen, Matt Tilley, Kimmo Tuominen, and Sergei Voloshin. The different collaborations allowed the diverse treatment of a variety of subjects related to flow physics that was presented in this work.

The number of people from both the theoretical and experimental heavy ion physics community which I would like to acknowledge personally for the numerous and often very lively discussions is as exhaustive as a list of authors of a typical publication from RHIC. Therefore I refrain from writing down all the names, but give my greatest thanks to all of you for the motivating and critical feedback that I received throughout my work. I do wish to express special thanks to Jane Burward-Hoy and Barbara Jacak who provided crucial contributions for the analysis which are part of Chapter 3; Raimond Snellings and Art Poskanzer offered the necessary insights on anisotropic flow analysis from the experimentalists points of view which led to a large part of the analysis in Chapter 4, and continuous discussions with Mike Lisa helped to shape Chapter 5.

Meiner Familie, besonders meinen Eltern Anneliese und Siegfried, meinem Bruder Michael mit Irmgard sowie meinen Großeltern, bin ich für die jahrelange Untersützung dankbar, durch welche ich mir so viele meiner Jugendträume erfüllen konnte. Trotz der vielen Abwesenheit sorgen sie auch dafür, dass ich in der Heimat nie fremd werde. Auch meinen Studienkollegen Christian Walter und Harald Dobler möchte ich in diesem Sinne danken.

For keeping me cheerful even through the end of my thesis work I am grateful to Mara who showed endless patience even in the toughest times. The wonderful DeWees Family quickly gave me a feeling of having a second home so far away from my mountainous origins. In plus, Mara also deserves credit for help with some figures.

For financial support and/or hospitality, I would like to thank the University of Regensburg, the Ohio State University, the University of Jyväskylä, CERN, BNL and LBL, the DAAD, and the DFG.

Thank you all so much!